Strojniški vestnik
Journal of Mechanical Engineering

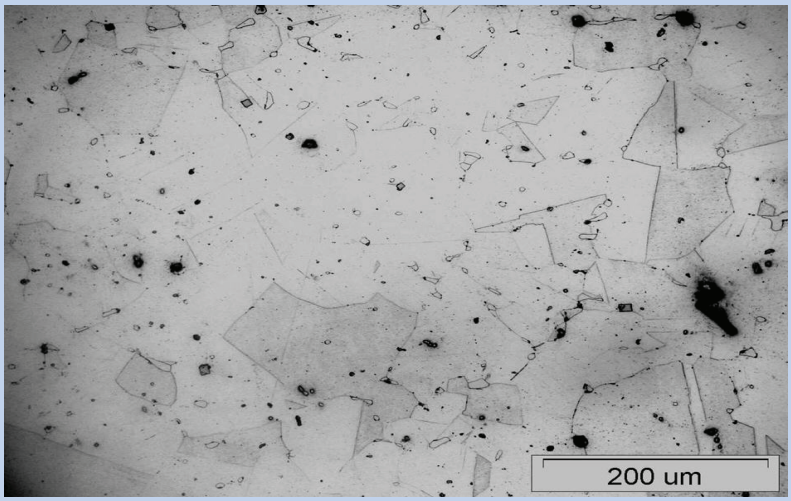

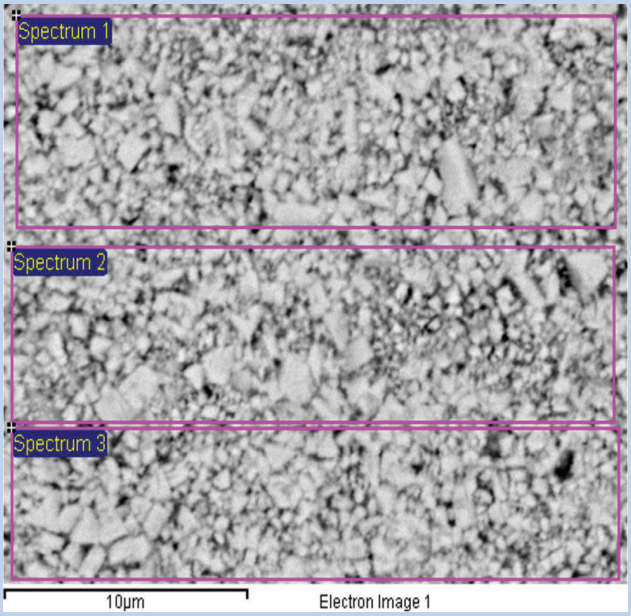

no. 11
year 2020
volume 66

Strojniški vestnik – Journal of Mechanical Engineering (SV-JME)

Aim and Scope

The international journal publishes original and (mini)review articles covering the concepts of materials science, mechanics, kinematics, thermodynamics, energy and environment, mechatronics and robotics, fluid mechanics, tribology, cybernetics, industrial engineering and structural analysis.

The journal follows new trends and progress proven practice in the mechanical engineering and also in the closely related sciences as are electrical, civil and process engineering, medicine, microbiology, ecology, agriculture, transport systems, aviation, and others, thus creating a unique forum for interdisciplinary or multidisciplinary dialogue.

The international conferences selected papers are welcome for publishing as a special issue of SV-JME with invited co-editor(s).

Editorial Office

University of Ljubljana, Faculty of Mechanical Engineering
SV-JME, Aškerčeva 6, SI-1000 Ljubljana, Slovenia
Phone: 386 (0)1 4771 137
Fax: 386 (0)1 2518 567
info@sv-jme.eu, http://www.sv-jme.eu

Print: Koštomaj printing office, printed in 275 copies

Founders and Publishers

University of Ljubljana, Faculty of Mechanical Engineering, Slovenia
University of Maribor, Faculty of Mechanical Engineering, Slovenia
Association of Mechanical Engineers of Slovenia
Chamber of Commerce and Industry of Slovenia, Metal Processing Industry Association

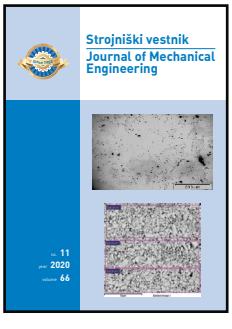

Cover:
The metallographic structure of AISI 321 steel at × 200 magnification (above) and the BEC image of the microstructure of H10F tungsten carbide microstructure at × 5000 magnification (below).

Image courtesy:
Faculty of Mechanical Engineering, Opole University of Technology, Opole, Poland

General information

Strojniški vestnik – Journal of Mechanical Engineering is published in 11 issues per year (July and August is a double issue).

Institutional prices include print & online access: institutional subscription price and foreign subscription €100,00 (the price of a single issue is €10,00); general public subscription and student subscription €50,00 (the price of a single issue is €5,00). Prices are exclusive of tax. Delivery is included in the price. The recipient is responsible for paying any import duties or taxes. Legal title passes to the customer on dispatch by our distributor. Single issues from current and recent volumes are available at the current single-issue price. To order the journal, please complete the form on our website. For submissions, subscriptions and all other information please visit: *http://www.sv-jme.eu.*

You can advertise on the inner and outer side of the back cover of the journal. The authors of the published papers are invited to send photos or pictures with short explanation for cover content.

We would like to thank the reviewers who have taken part in the peer-review process.

ISSN 0039-2480, ISSN 2536-2948 (online)

The journal is subsidized by Slovenian Research Agency.

Strojniški vestnik - Journal of Mechanical Engineering is available on *https://www.sv-jme.eu*.

Contents

Strojniški vestnik - Journal of Mechanical Engineering
volume 66, (2020), number 11
Ljubljana, November 2020
ISSN 0039-2480

Published monthly

Papers

Strojniški vestnik - Journal of Mechanical Engineering 66(2020)11, 629-641
DOI:10.5545/sv-jme.2020.6840
Original Scientific Paper
Received for review: 2020-07-01
Received revised form: 2020-09-08
Accepted for publication: 2020-10-13

Temperature and Heat Partition Testing in the Cutting Zone for Turning AISI 321 Steel

Marian Bartoszuk*
Opole University of Technology, Faculty of Mechanical Engineering, Poland

This article shows selected results of experimental tests and the results of analytical and numerical modelling of the thermal characteristics of the cutting process. The tests were conducted for the case of the dry turning of austenitic steel AISI 321 with cutting tools with a flat rake face. The research aimed to determine the actual division of thermal fluxes in the zone of contact between the chip and the rake face. As a result of such work, a formula for a new heat partition coefficient and a formula for calculating the average contact temperature were developed. The results showed that the formulas developed can be a useful tool to estimate heat distribution in the cutting zone quickly.
Keywords: cutting process, numerical modelling, contact temperature, heat partition

Highlights
- *This article examines the heat dissipation in the chip-to-rake face interface.*
- *The analyses were carried out using the results of experimental research, analytical modelling, and computer simulations.*
- *A formula was developed for a new heat partition coefficient at the chip-to-cutting tool interface.*
- *A new formula for determining the average contact temperature was proposed.*

0 INTRODUCTION

Heat is emitted while machining metal materials. This heat is generated by the plastic deformation of the workpiece material and by the friction of the cutting tool surface against the workpiece. It is believed that it is the high temperature and distribution of heat in the cutting zone that are the main factors determining tool wear. The negative influence of temperature on tool life is particularly important in dry cutting at high cutting speeds [1] and [2]. Economic and environmental pressures require the cutting to be carried under precisely these conditions. The amount of heat generated during the cutting process depends mainly on the machining parameters and the machinability of the workpiece material. In contrast, the distribution of heat between the tool, chip and workpiece depends mainly on the mutual ratio of the thermophysical properties of the cutting tool material and the workpiece material [3] and [1]. The most important are thermal conductivity, thermal diffusivity, and heat transfer coefficient. In industrial practice, tool manufacturers use advanced protective coatings to reduce the negative impact of cutting temperatures. The chemical compositions of coatings and their structure are constantly changing. The ever-increasing demands of tool users dictate these changes.

For exploratory purposes, the temperature values in the individual areas of the cutting zone can be determined using appropriate mathematical models, the methodology proposed by Shaw [3], Reznikov [4] or Silin [5] can be mentioned. These calculations are often based on heat partition coefficients, which determine how much of the heat flux enters the tool. Nowadays, the analyses of heat distribution in the cutting zone are often supported by the results of computer simulations or thermographic measurements. The finite element method (FEM) [6] and [7], as well as the boundary element method (BEM) [8] and [9], are usually used for computer simulations, less often the finite difference method (FDM) [1] and [10] is utilised. The wide popularity of these calculation methods is due to their universality. They allow for the simultaneous observation of the stress distribution of temperature fields deformation, etc. The smoothed-particle hydrodynamics (SPH) method has similar computational capabilities [11] and [12]. However, it is not very common in machining.

The least frequently used is the method of elementary balances (MEB) being a variation of the FDM method. In this method, usually only the heat distribution in the cutting zone is tested [13]. For example, using this method, Bartoszuk and Grzesik [10] researched the temperature distribution and direction of flow of heat fluxes along the length of the chip-tool interface. Any calculation using this method may be carried out considering the area of the moving chip or without the chip (only for the cutting tool itself) [1]. In the latter case, however, it is necessary to know the heat partition coefficient. This coefficient allows you to calculate how much heat is introduced into the cutting tool area through the length of the chip-tool interface. However, the calculation formulas of

*Corr. Author's Address: Opole University of Technology, Prószkowska 76 Street 45-758 Opole, Poland, m.bartoszuk@po.edu.pl

commonly used heat partition coefficients (according to Shaw [3], Reznikov [4] or Kato-Fujii heat partition coefficient [5]) were defined many years ago. At that time, high-speed steel tools and first-generation carbide cutting tools were commonly used. Therefore, the machining parameters were modest. Nowadays, mainly state-of-the-art carbide tool materials and much higher values of cutting parameters are used. Therefore, calculations made with the help of these coefficients may be subject to material error.

In recent years, several papers have appeared in the literature describing heat distribution in the contact zone. However, there is little research in this area, and it is usually related to the topic of estimating the factors influencing the change in heat conduction at the chip-cutting tool interface. For example, Jam and Fard [14] used the reverse procedure to estimate the thermal conductivity at the chip-tool interface. The study was conducted for carbide cutting tools and AISI 1045 steel. The paper shows that it is possible to increase the accuracy of numerical calculations by correcting the heat partition coefficient.

Jin et al. [15] examined how the heat distribution in the cutting zone occurs and what effect the basic protective coatings have on heat dissipation. The research was conducted for H13 steel. In contrast, Jinfu and Liu [16] studied the changes in the heat partition coefficient over time and showed that the value of the heat partition coefficient decreases with increasing cutting speed. Carbide cutting tools and Inconel 718 were tested. Similar issues were addressed by Zemzemi et al. [17]. They studied the cutting of Inconel 718 with carbide and CBN cutting inserts. Similarly to previous researchers, they demonstrated that the value of the heat partition coefficient decreases as the cutting speed increases. It should be noted that a major shortcoming of these works is the assumption of constant and temperature-independent thermo-physical properties of the tested materials.

To summarize, the calculation formulas used thus far for heat partition coefficients do not work very well for modern tool materials, especially at higher cutting speeds. An extensive analysis of the literature has shown that there is no alternative calculation methodology that reliably describes the heat distribution in the chip-tool interface for modern carbide tools and the machining parameters recommended by manufacturers. Recognizing the shortage of knowledge in this area, the author attempted to develop a new heat partition coefficient that better describes the heat distribution between the chip and cutting tool, specifically one that will perform well in modern tool materials at higher cutting speeds.

In order to determine the new coefficient of heat partition at the interface between the cutting tool and the workpiece material, comprehensive analyses of the cutting process were carried out. The activities included experimental tests of the turning process, analytical temperature modelling, and numerical modelling of heat dissipation in the cutting zone. It was only on the basis of such research that a formula for a new heat partition coefficient and a formula for calculating the average temperature of the chip-tool interface were developed. The results obtained were compared with the results of the experiment. In order to better understand the basic laws governing the division of heat at the interface between the cutting insert and the workpiece material, the consideration was limited to the case of dry turning with a carbide tool with a flat rake face.

1 TEST METHODOLOGY

The case of orthogonal cutting of AISI 321 steel with an uncoated H10F carbide cutting insert was selected for testing. The tests were carried out using the PTNGR 2020-16 tool holder and the TNMA 160408 cutting insert with a flat rake face (Table 1). No cooling lubricant was used during the machining.

Table 1. *Specification of the angles of the tool cutting insert*

Angle	Designation	Value [°]
Rake	γ_n	–5
Clearance	α_n	5
entering – main	κ_r	90
entering – auxiliary	κ_r'	-
cutting edge inclination	λ_s	–6

The following machining conditions are assumed:

- cutting speed, v_c: 66.67 m/min, 86.33 m/min, 100.00 m/min, 116.67 m/min, 133.33 m/min, 150.00 m/min,
- feed rate, *f:* 0.10 mm/rev, 0.20 mm/rev, 0.28 mm/rev, 0.40 mm/rev,
- depth of cut, a_p: 2 mm.

The experimental tests were conducted in two stages. In the first stage, measurements were made during the tests in which the values of the components of the total cutting force were measured, and the value of the thermoelectric force signal generated at the contact between the cutting tool and the chip and thermographic images of the cutting zone were collected. In the second stage, i.e., after the end of the turning tests, the chip compression, length, and contact area were determined. The experimental tests

were carried out on a stand based on the TUM-35D1 centre lathe (Fig. 1). Two dynamometers were used alternately: a tensometric dynamometer of our own design and a KISTLER 9257B dynamometer with suitable measuring equipment [12]. The mean contact temperature was measured using the natural single-point thermocouple method [18].

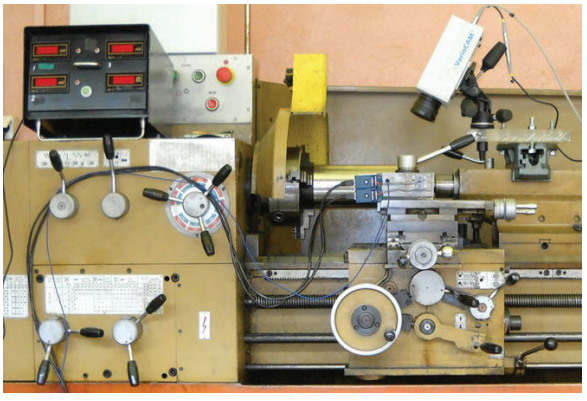

Fig. 1. *View of the test bench*

Thermographic images were collected using a JENOPTIK VarioCAM thermal imaging camera equipped with the IRBIS 3 software dedicated to archiving and processing thermographic images [12]. A sample image from an IR camera with a visible chip is shown in Fig. 2.

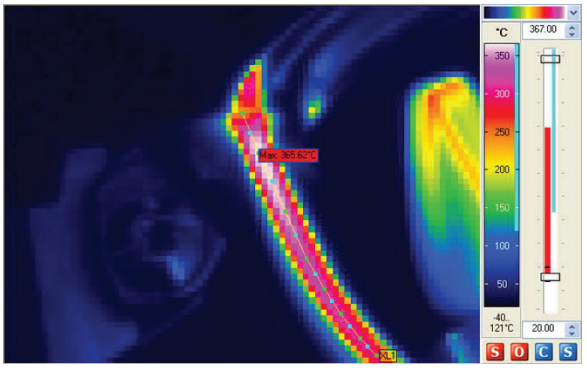

Fig. 2. *A thermographic image of the cutting zone obtained at a cutting speed v_c = 100 m/min and feed rate f = 0.20 mm/rev*

Experimental tests of the cutting process were carried out on specimens in the form of a cylinder with undercut forming a short pipe with a wall thickness of 2 mm. The requirement to isolate electrically the sample from the mechanisms of the machine tool was obtained using special insulating inserts made of dielectric materials. The LabVIEW software was used to record the tested signals.

1.1 Workpiece Material

The tests were carried out for one workpiece material, i.e., austenitic steel AISI 321 (DIN 1.4541). The quality of the material selected for testing was guaranteed by approval No MEST944800/2010/. Notwithstanding the above, the chemical composition of the material to be machined was tested experimentally. The results obtained are shown in Table 2.

The steel tested has a relatively low yield stress $R_{0.2}$ of 255 N/mm². In addition, this material has a high tendency to be reinforced by compression. After compression, the value of $R_{0.2}$ reaches from 1080 N/mm² to 1370 N/mm². The metallographic structure of AISI 321 steel is shown in Fig. 3.

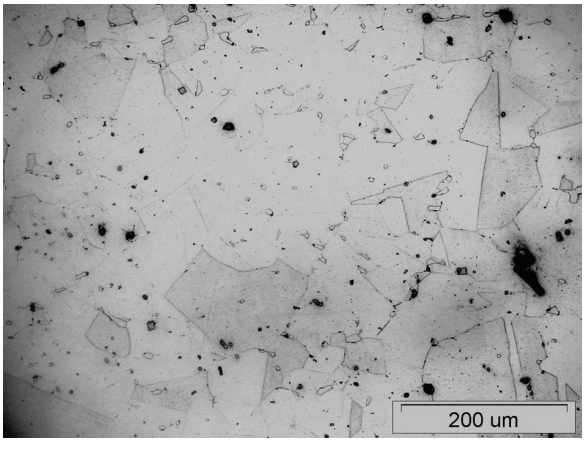

Fig. 3. *Microstructure of AISI 321 steel at ×200 magnification*

The hardness of the material was measured before the tests started. The measurements were made using the Brinell test method, on a Zwick/Roell ZHV 10 hardness tester, with an indenter load (balls of 1 mm diameter) of 10 kg. The average hardness value is 164 HB ± 5 HB.

Table 2. *Alloying composition of AISI 321 steel determined by tests*

Alloying element	Mn	Si	P	S	Cr	Ni	Mo	Cu	V	Al
Average content, [%]	1.63	0.66	0.007	0.014	17.31	9.29	0.36	0.43	0.062	0.025
Alloying element	Ti	W	Co	Pb	Sn	As	B	N	Ca	Fe
Average content, [%]	0.309	0.029	0.116	<0.001	0.010	0.003	0.0013	<0.001	0.0017	69.70

1.2 Cutting Tool

The H10F carbide cutting inserts from Sandvik Coromant used in the research have very good impact strength but relatively low abrasion resistance. These characteristics result from both the chemical composition and the grain size.

According to the manufacturer's data, H10F carbide consists of WC tungsten carbide (about 90 %) and cobalt (about 10 %) and the WC particle size of <0.8 μm classifies this material as fine carbide [2].

The chemical composition and microstructure of the cutting inserts tested were examined on the JEOL digital scanning electron microscope JSM-6460LV equipped with an EDS X-ray spectrometer. The image of the microstructure of the H10F tungsten carbide is shown in Fig. 4.

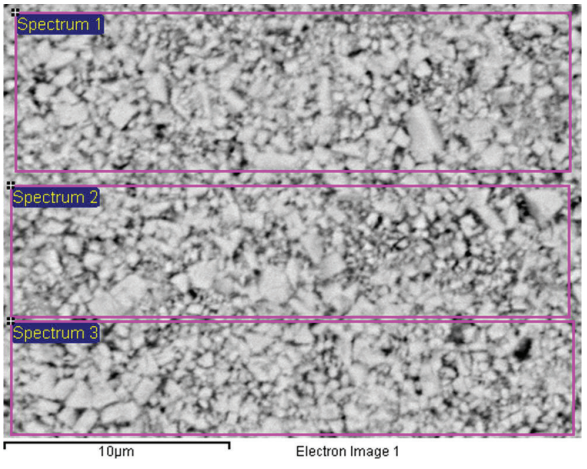

Fig. 4. *BEC image of the H10F tungsten carbide microstructure at ×5000 magnification*

The basic physical properties of the H10F carbide obtained from the literature are shown in Table 3. To complete the information, the hardness of the cutting insert was measured on its rake face. The tests were carried out using the Vickers method, on the Zwick/Roell ZHV 10 hardness meter. The average measured hardness value of the H10F carbide is 1604 HV ± 16 HV.

Table 3. *Selected physical properties of the H10F carbide according to* [2]

Hardness HV30	Density [g/cm³]	Fracture resistance, k_{Ic} [N/mm²]	Flexural strength, [N/mm²]	Compressive strength, [N/mm²]	Corrosion resistance 1 to 10	Wear resistance 1 to 10
1600	14.45	12.7	4300	6250	4	5

1.3 Measurement of the Temperature of Cutting by Natural Thermocouple

In order to measure the average contact temperature using the single-point method, it was necessary to determine the characteristic $t = f(tef)$ for the tested couple: carbide H10F – workpiece material AISI 321. This characteristic takes the following form:

$$t = 66.63299244 \cdot tef + 198.2808622 . \quad (1)$$

The correlation coefficient for the above equation was 0.845.

1.4 Measurement of Contact Length

In order to determine the length of contact and estimate the actual contact area after each turning test, a digital image of the abrasion area was taken on the LEICA MS 5 microscope. Measurements of the l_{nc} contact length and planimetry of the A_k contact area were performed using the LEICA IM 1000 Image Manager software.

1.5 Numerical calculation

These studies used a special variant of the FDM method called the method of elementary balances (MEB), in which differential equations are defined on the basis of energy balances for all discrete elements of the calculation model. This method uses only Fourier's law and a typical computational grid. In the presented studies, the calculations were made using Microsoft Excel. In the calculation, a grid with square elements of 5 μm mesh size was used. Each cell in the calculation sheet is assigned to one discrete element of the analytical model. As a result, the model was built as a set of cells containing the relevant formulas and values. In this way, both the geometric and physical features of the modelled process are represented. Formulas are entered in accordance with the open differential procedure method [13].

The calculations were made for the two-dimensional heat flow problem. Therefore, the partial differential equation for heat conduction in two perpendicular directions x and y, expressed by the Fourier heat conduction law, can be recorded as a finite difference:

$$\frac{T_{i-1,j} - 2T_{i,j} + T_{i+1,j}}{(\Delta x)^2} + \frac{T_{i-1,j} - 2T_{i,j} + T_{i+1,j}}{(\Delta y)^2} = 0. \quad (2)$$

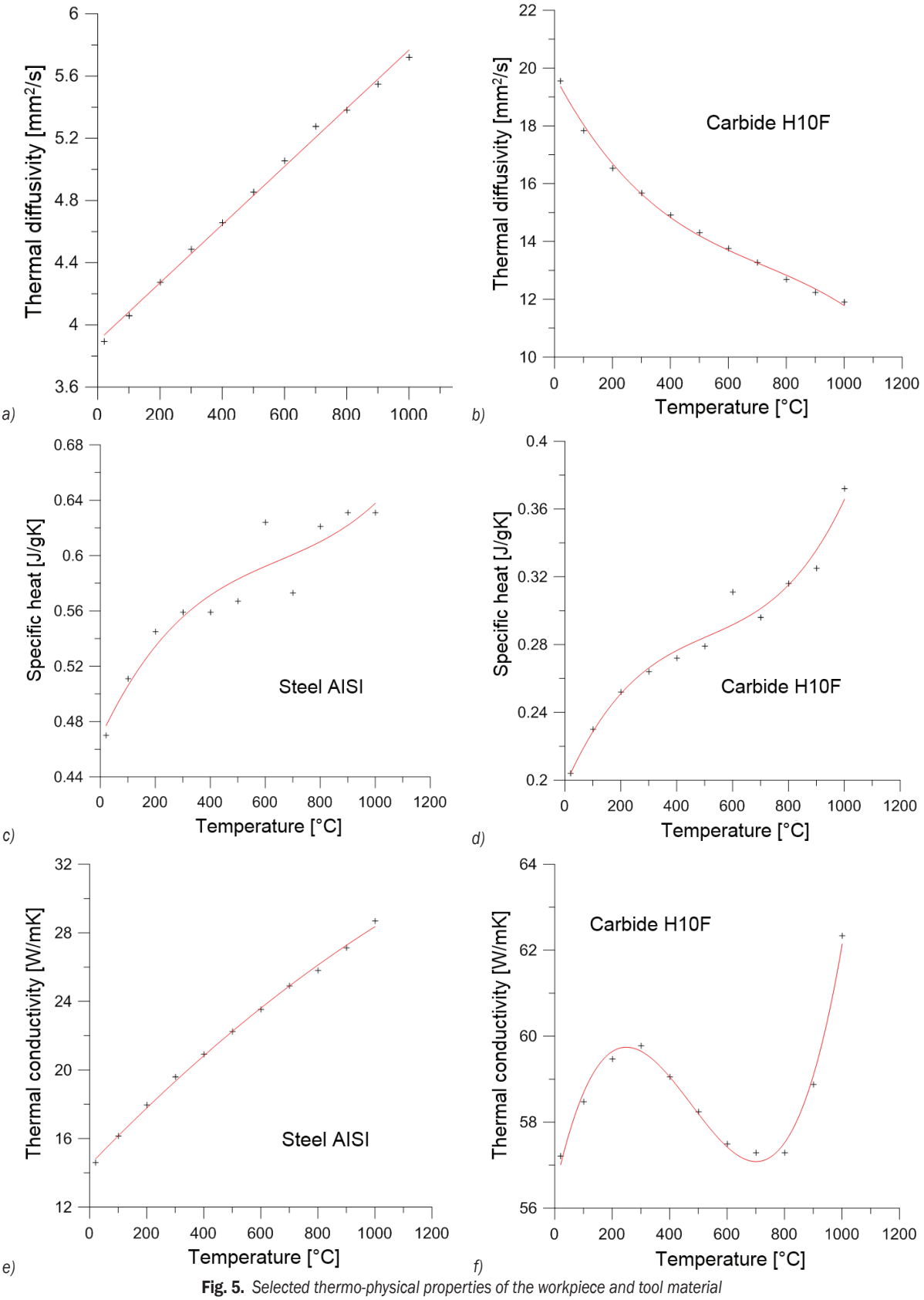

Fig. 5. *Selected thermo-physical properties of the workpiece and tool material*

The difference equation can be solved numerically using eight specific linear and corner boundary conditions [13]. It should be noted that these calculations were carried out for time-varying and temperature-dependent thermo-physical properties of the cutting insert and material machined. Their numerical values were determined using the laser-flash-technique using the LFA-457 MicroFlash from Netzsch. The graphic presentation of the thermo-physical properties of the materials tested is shown in Fig. 5.

The density of both materials was also determined. It is respectively: 7.86 g/cm³ ± 0.02 g/cm³ for the AISI 321 steel, and 14.33 g/cm³ ± 0.02 g/cm³ for the H10F carbide. Thermal conductivity $\lambda(T)$ shown in Figs. 5e and f was calculated from the formula:

$$\lambda(T) = \alpha(T) \cdot \rho \cdot c_p(T), \tag{3}$$

where $\alpha(T)$ is thermal diffusivity as a function of temperature, and $c_p(T)$ a specific heat as a function of temperature.

The mathematical description of the discussed characteristics as a function of temperature is shown in Table 4.

In the first phase of calculations, the actual heat dissipation in the contact zone was mapped in the simulations. For this purpose, the so-called full calculation model was used, consisting of the cutting tool area and the moving chip (Fig. 6).

Two heat sources were defined in the calculation. Both heat sources were defined in the chip area. A plastic deformation heat source with a trapezoidal shape was defined on the slip plane (Fig. 7a). A triangular source of friction heat of the chip against the rake face was determined at the contact length (Fig. 7b). In these calculations, the division of the thermal fluxes between the chip and the cutting tool was spontaneous.

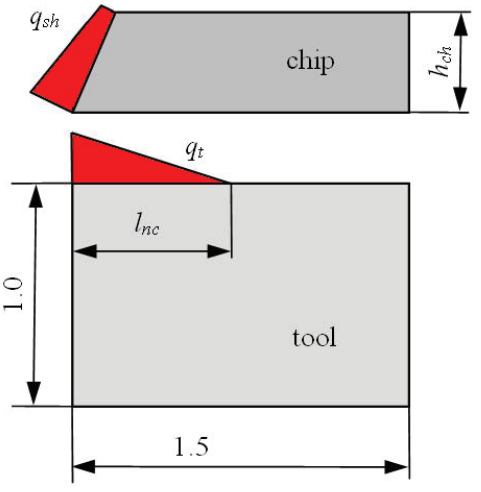

Fig. 6. *Full calculation model – with a chip*

In the second phase of simulation calculations, tests were conducted to estimate the actual amount of heat entering the tool through the length of contact. For this purpose, a simplified model was built, without the chip area (Fig. 8).

The density of the heat source q_n was determined by the method of successive approximations, aiming at the same average contact temperature value as for the full model. Comparison of the heat flux intensity value for the full model (with a chip) with the heat flux intensity for the cutting tool itself (for the simplified model) enables determining the actual heat partition coefficient R_B.

Table 4. *Equations of thermo-physical properties of the AISI 321 steel and H10F carbide in the temperature range 21 °C to 1000 °C*

Material		Equation	Correlation coefficient
AISI 321	Thermal diffusivity [mm²/s]	$Y = 0.001871271133 \cdot X + 3.896226402$	0.996
	Specific heat [J/(gK)]	$Y = 0.4684519516 + 0.000423468973 \cdot X - 5.238734575^{-7} \cdot X^2 + 2.697322783^{-10} \cdot X^3$	0.903
	Thermal conductivity [W/(mK)]	$Y = 14.45503166 + 0.01727554457 \cdot X - 3.37250283^{-6} \cdot X^2$	0.998
H10F	Thermal diffusivity [mm²/s]	$Y = 19.74440671 - 0.01895773412 \cdot X + 2.050360366^{-5} X^2 - 9.5090811^{-9} \cdot X^3$	0.997
	Specific heat, [J/(gK)]	$Y = 0.1965537097 + 0.0003752508169 \cdot X - 5.93466171^{-7} \cdot X^2 + 3.871187722^{-10} \cdot X^3$	0.972
	Thermal conductivity [W/(mK)]	$Y = 56.41965076 + 0.03025415521 \cdot X - 8.225706975^{-5} \cdot X^2 + 5.769878661^{-8} \cdot X^3$	0.985

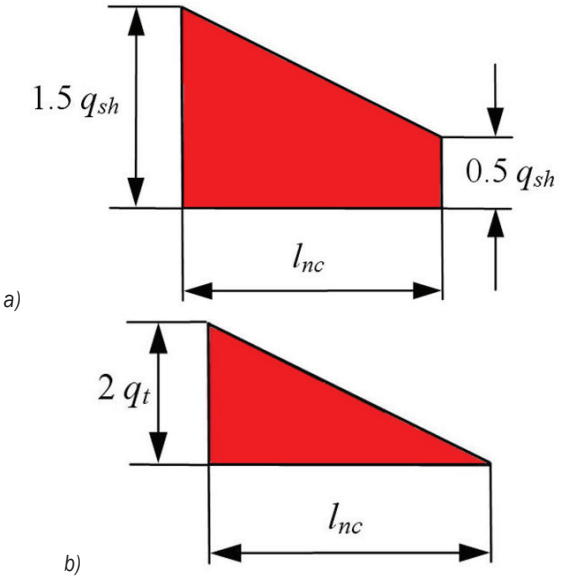

Fig. 7. *Heat sources used in the tests; a) source of heat in the slip plane, and b) source of heat in the contact length*

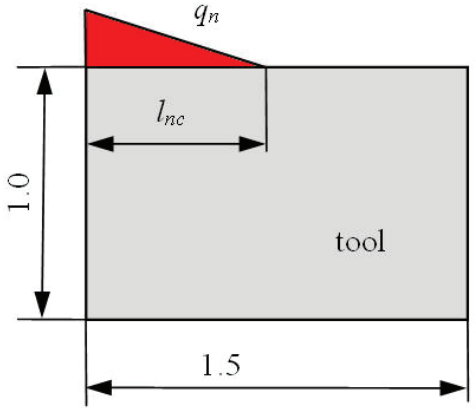

Fig. 8. *Simplified model – without a chip*

2 RESULTS AND DISCUSSION

2.1 Experimental Studies

The measured values of the components of the total cutting force, the average contact temperature and the maximum temperature of the chip upper side are shown in Table 5. The results were obtained for a variable cutting speed and feed rate of 0.2 mm/rev. After the end of the experiment, *inter alia*, the chip compression ratio k_h, the mechanical contact load k_F, the slip angle Φ and the slip coefficient μ, the contact stress values σ_k, τ_k were calculated. These values were calculated on the basis of the previously measured chip thickness values h_{ch}, the contact area A_k, the contact length l_{nc} and the main cutting force components (peripheral force F_c and feed force F_f). The study results collected in this way formed the basis for the construction of analytical and numerical models describing the heat dissipation in the cutting zone.

2.2 Analytical Modelling

Analytical modelling of thermal characteristics of the cutting process was carried out on the basis of commonly known relationships describing tribomechanical characteristics of the turning process [19]. The calculations focused on determining the average and maximum temperature values in the zone of primary plastic deformation (slip zone) and secondary plastic deformation (friction zone).

Generally speaking, due to the tool life, the maximum contact temperature seems to be the most important. Unfortunately, it cannot be measured. During the experimental studies, only information was collected about the value of the average contact temperature measured at the interface between the cutting tool and the workpiece material and about the temperature of the chip upper side. However, the maximum contact temperature that we are interested in can be determined with an analytical approach [4] and [5]. The detailed algorithm of conducted analytical calculations and interrelationships between the calculation formulas are shown in Fig. 9.

According to the algorithm presented, in order to calculate the maximum contact temperature, it is necessary to know the average and maximum temperature in the zone of primary and secondary plastic deformation. Temperatures generated in the zone of primary plastic deformation were determined according to the methodology proposed by Silin [5].

A comprehensive graphical representation of the algorithm for determining the thermal characteristics of the cutting process is shown in Fig. 9. In contrast, the numerical values of the average and maximum contact temperature calculated for cutting with a constant feed rate f = 0.20 mm/rev and a variable cutting speed are shown in Table 5. It should be noted that the calculations were made taking into account the influence of temperature on the thermo-physical properties of both materials tested. A graphical comparison of the sample calculation results with the experimentally obtained data is shown in Fig. 10. The dashed line on the graphs shows the average contact temperature determined experimentally, whereas the solid line shows the result of analytical modelling. Modelling of the temperature of the contact t_k and the

maximum temperature of the contact t_{kmax} was carried out according to the formulas shown in Fig. 9.

The analysis of the distribution of the presented temperature curves shows that for the H10F cutting

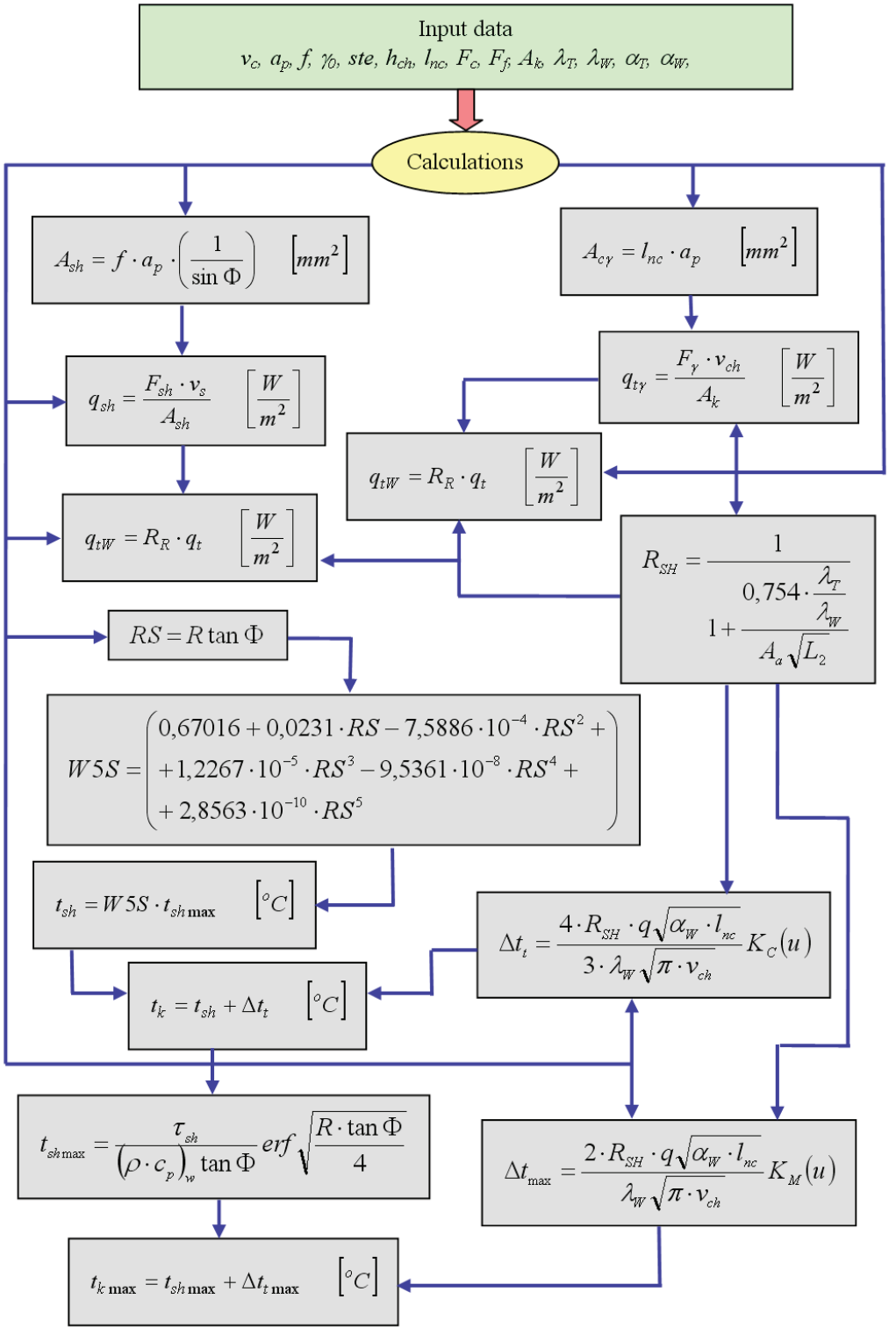

Fig. 9. *Algorithm for determining the thermal characteristics of the cutting process*

insert without protective coatings the value of the average contact temperature determined analytically is about 20 % to 25 % lower than the value obtained by way of experimentation. It can be assumed that the source of discrepancies between the measured and modelled average contact temperature value lies mainly in the adopted calculation methodology and, above all, in the imperfections of commonly known heat partition coefficients and in the analytical models themselves, as indicated by the research conducted by Niesłony **[19]**.

Table 5. *Summary of calculated average and maximum contact temperature values for a variable cutting speed and feed rate of 0.2 mm/rev*

f [mm/rev]	v_c [m/min]	F_c [N]	F_f [N]	t_k [°C]	$t_{W\max}$ [°C]	t_k [°C]	$t_{k\max}$ [°C]
		Experiment				Analytical model	
0.20	66.67	1369.4	1085.5	880.0	367.3	650.0	960.1
0.20	86.33	1274.7	959.4	912.4	376.5	696.9	1031.3
0.20	100.00	1212.7	887.7	931.0	381.8	732.1	1088.7
0.20	116.67	1141.2	812.5	949.4	387.3	757.6	1135.4
0.20	133.33	1074.0	747.3	963.1	392.1	774.6	1173.4
0.20	150.00	1010.7	689.9	972.0	396.3	784.4	1204.3

Based on literature data **[1]** and **[2]** and the results of the calculations carried out, it can be concluded that the heat generated in the zone of the primary plastic deformation and then accumulated in the chip is almost entirely carried away with the chip.

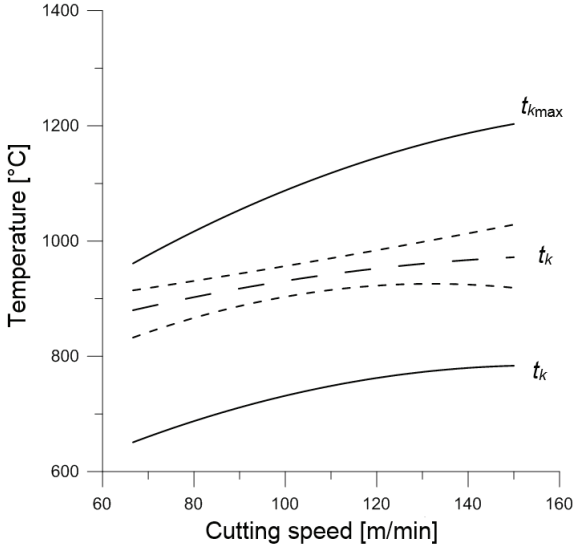

Fig. 10. *Average and maximum contact temperature for the H10F cutting tool (without coatings), solid lines – data from analytical models, dashed line – experimental data*

Some of it, however, penetrates the cutting tool through the contact area, combining with the heat of friction between the chip and the rake face of the cutting tool. The amount of heat entering the tool in this way can be calculated analytically using the heat partition coefficients (according to Shaw **[3]**, Reznikov **[4]**, or Kato-Fujii heat partition coefficient **[5]**. However, it must be remembered that these coefficients of heat give a clear underestimation of the total heat flux penetrating the cutting edge of the tool **[10]** and **[12]**. Moreover, they are highly sensitive to the correct selection of material data.

2.3 Simulation Modelling

The results of numerical modelling carried out according to the procedure described above are shown in Table 6. The comparison of the average contact temperature measurements and the numerical calculation results obtained for the full model (with a chip) shows that the largest discrepancies in the results were recorded for low cutting speeds, respectively –5.0 % for v_c = 83.33 m/min and –11.31 % for v_c = 66.67 m/min.

Table 6. *Summary of the results of simulations of heat dissipation in the contact zone for the uncoated H10F cutting insert for a variable cutting speed and feed rate of 0.2 mm/rev*

v_c [m/min]	t_k [°C]	t_k [°C]	Deviation [%]	t_k [°C]	Deviation [%]
	Experiment	Simulation – full model		Simulation – simplified model	
66.67	880.0	780.50	-11.31	780.80	-11.27
83.33	912.4	862.50	-5.00	861.64	-5.10
100.00	931.0	924.85	-0.66	925.02	-0.64
116.67	949.4	970.33	2.20	970.50	2.22
133.33	963.1	1010.39	4.91	1012.31	5.11
150.00	972.0	1032.13	6.19	1030.12	5.98

This phenomenon probably results from the shape of the heat source, adopted for the calculations, defined at the slip plane and at the contact length **[10]**. Another reason for these differences may be the longer stabilization time of the model at low cutting speeds. Assuming that the obtained differences in the results are acceptable, simulations of heat distribution were performed for the simplified model (without a chip). The calculations were carried out by selecting the intensity of the heat source in such a way as to get as close as possible to the results obtained in the first simulation round (for the full model). A comparison of the contact temperature values for the experiment and both simulation models is shown in Table 6.

It can be noted that for both numerical models very similar deviation values were obtained, whereas Table 7 presents the thermal flux figures for the full (q_t) and simplified (q_n) models. A graphical comparison of the variation in the intensity of both these heat fluxes as a function of cutting speed is shown in Fig. 11. The analysis of the course of change of both heat fluxes indicates that the actual value of the heat flux q_n penetrating the cutting tool surface through the contact length is lower than the friction heat flux q_t by about 25 % for low cutting speeds and about 55 % for high speeds. This phenomenon can be explained in part by the ratio of thermo-physical properties of the workpiece material and the cutting tool material and in part by the influence of the cutting speed on the division of the thermal fluxes in the zone of cutting.

Table 7. *Summary of the frictional heat flux values for the full and simplified model, for the H10F cutting tool without coatings; machining parameters: v_c = vario, f = 0.2 mm/rev*

v_c [m/min]	q_t [MW/m^2] Simulation – full model	q_n [MW/m^2] Simulation – simplified model	$q_n / q_t = R_B$
66.67	137.694	104.796	0.761076
83.33	178.315	130.477	0.731726
100.00	221.789	137.144	0.618352
116.67	269.060	151.603	0.563453
133.33	321.581	163.797	0.509350
150.00	381.783	176.664	0.462733

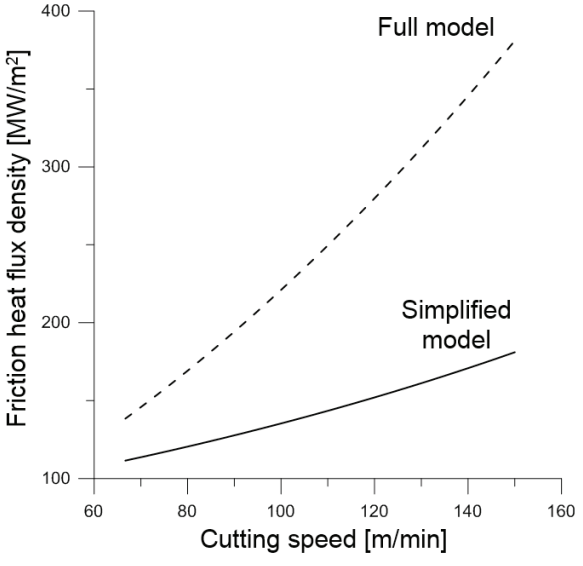

Fig. 11. *Influence of the cutting speed on changes in frictional heat flux density, machining parameters: v_c = vario, a_p = 2 mm, f = 0.2 mm/rev*

It is important to remember that as the cutting speed increases, the heat flux of friction and heat of plastic deformation does so also, while at the same time the contact length decreases and the chip evacuation speed increases. This phenomenon shortens the duration of the influence of the thermal fluxes on the cutting insert. As a result, the total amount of heat penetrating the cutting tool is significantly reduced. The analysis of the mutual ratio of the heat fluxes q_t to q_n (Fig. 11) shows that as the cutting speed increases, the actual amount of heat entering the tool through the contact length decreases, which means that the heat partition coefficient will also decrease as the cutting speed increases. These results are confirmed in the literature, because a decrease in the partition coefficient with an increase in the v_c speed was proved earlier by Jinfu and Liu [16] and Zemzemi et al. [17].

From the analysis of the simulation results (Table 7) and the course of changes calculated analytically and determined in the simulations of the actual friction heat flux density (Fig. 11) it can be seen that the ratio of the value of the actual heat flux penetrating the tool q_n to the value of the friction heat flux q_t may be a new value of the heat partition coefficient R_B. The new heat partition coefficient figures calculated in this way are shown in Table 7.

Analysis of the calculation formulas on the commonly known heat partition coefficients indicates that they are based almost exclusively on the mutual ratio of thermophysical properties of the workpiece and tool material. This approach seems to be correct because, as we know, it is the thermo-physical properties that mainly determine the heat distribution in the cutting zone. On the basis of the above-mentioned assumptions, a new formula of the heat partition coefficient R_B was developed, describing in a more rational way the heat distribution for carbide cutting tools without protection coatings. Its form can be recorded as follows:

$$R_B = -11.009 \cdot \ln \frac{b_T}{b_W} + 4.499, \tag{4}$$

where b_T is heat transfer coefficient for the tool, $b_T = \sqrt{\lambda_T \cdot \rho_T \cdot c_{pT}}$, and b_W heat transfer coefficient for the chip, $b_W = \sqrt{\lambda_W \cdot \rho_W \cdot c_{pW}}$.

The algorithm of the calculations carried out for this purpose is illustrated in Fig. 12.

The course of changes in the value of the new heat partition coefficient R_B calculated from Eq. (4) is shown as a function of the cutting speed in Fig. 13. For comparison, this graph shows the changes of commonly known literature-derived heat partition

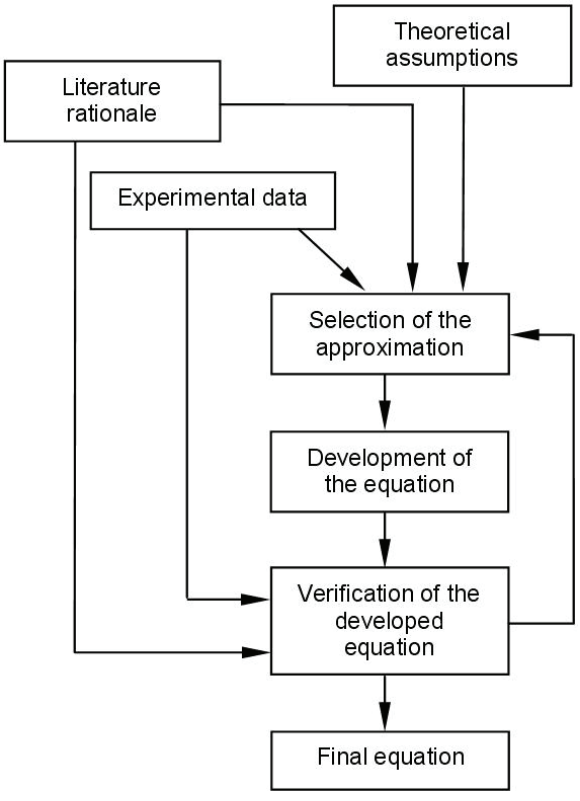

Fig. 12. *Algorithm for determining the heat partition coefficient equation*

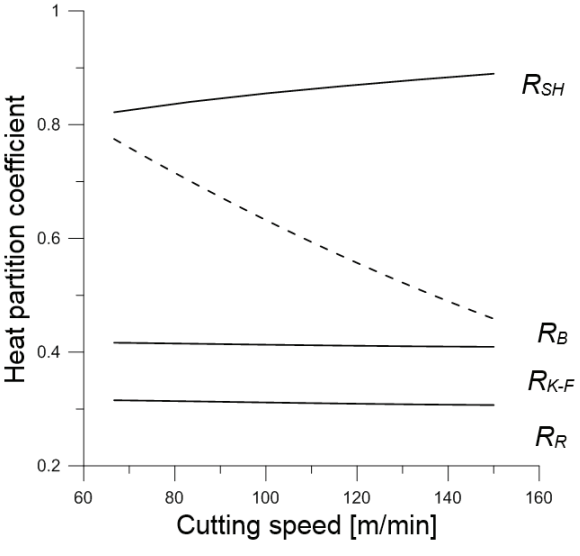

Fig. 13. *Course of change of different heat partition coefficients for the pair AISI321 steel-uncoated carbide, machining parameters: v_c = vario, a_p = 2 mm, f = 0.2 mm/rev*

coefficients according to Shaw **[3]**, Reznikov **[4]** and Kato-Fujii heat partition coefficient **[5]**. Note that the R_B value varies monotonously from 0.76 for v_c from 66 m/min to 0.46 m/min for a cutting speed of 150 m/min. The nature of these changes is completely different from the other heat partition coefficients.

The analysis of the distribution of the curves shows that the calculations demonstrated a relatively large discrepancy in the results, reaching -23 % for a cutting speed of 150 m/min. Therefore, the new heat partition coefficient does not match Shaw's empirical patterns. Thus, for the calculation of the average contact temperature, a new formula based on the law of heat conduction was proposed:

$$t_k = \frac{q_n}{\lambda_w} \cdot l_p, \tag{5}$$

where l_p is the length of the plastic interface.

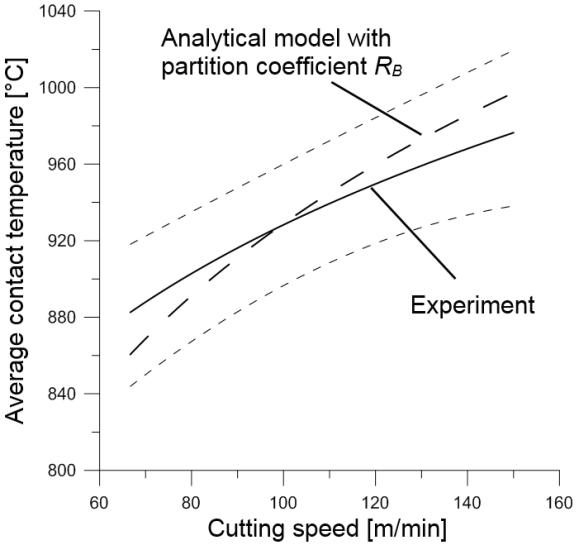

Fig. 14. *Comparison of the average contact temperature measured experimentally and determined from the law of heat conduction for the new partition coefficient, cutting tool: H10F without coatings, machining parameters: v_c = vario, a_p = 2 mm, f = 0.2 mm/rev*

Based on the literature data **[1]** and **[20]** and, in particular, the results of previous research **[10]** and **[12]**, the plastic interface length $l_p = 0.37 \cdot l_{nc}$, identical for all cases considered, was assumed for the calculations. The calculations performed according to Eq. (5) for the constant l_p value and using the new heat partition coefficient R_B are graphically shown in Fig. 14. This figure shows a comparison of the average contact temperature obtained from the calculations and from the experiment. Both graphs show a high level of alignment. The greatest temperature differences of about 3.5 % were recorded for extreme cutting speeds. It can be assumed that this error is due to the assumption of a constant value of the plastic interface

length l_p. In reality, l_p is not a constant quantity. It changes its value to a small extent as the cutting speed changes. In Eq. (5) the parameter l_p is a component of the product, therefore even a slight change in its value will translate into the final result.

4 CONCLUSIONS

The analysis of heat distribution in the cutting zone shown in this article allows for the following conclusions:

- The maximum temperature of the chip upper side, as well as the average cutting temperature determined in experimental studies, can be successfully used to validate numerical calculations. The research has proven that the temperature of the chip upper side represents about 50 % of the average contact temperature measured experimentally, whereas the difference between the average contact temperature determined experimentally and calculated in simulations ranges from -11.3 % to +6.2 %.
- The developed formula of the new heat partition coefficient R_B at the chip-to-cutting tool interface is based exclusively on the interrelationship of thermophysical properties of the cutting tool and workpiece material. The influence of the cutting speed is taken into account indirectly, by changing the temperature-dependent values of the thermophysical properties. Unlike other known heat partition coefficients, its value decreases monotonically as the cutting speed increases and changes between 0.76 (for v_c = 66 m/min) and 0.46 (for v_c = 150 m/min).
- The new formula for average contact temperature was derived from Fourier's law and is much simpler than the empirical formulas used so far. The calculations made with its help and using the new heat partition coefficient R_B are characterized by an error not exceeding 3.5 %.

5 REFERENCES

[1] Grzesik, W. (2017). *Advanced Machining Processes of Metallic Materials: Theory, Modelling, and Applications*, Elsevier, Amsterdam.

[2] Davim, J.P. (2010). *Metal Cutting*, Nova Science Publishers Inc., New York

[3] Shaw, M.C. (2004). *Metal cutting principles*, Oxford University Press, Oxford.

[4] Reznikov, A.N. (1981). *Thermophysics of Metal Machining Processes*, Mechanical Engineering, Moscow. (in Russian)

[5] Silin, S.S. (1979). *Similarity Method when Cutting Materials, Mechanical Engineering*, Moscow. (in Russian)

[6] Venkatesh, S.S., Ram Kumar, T.A., Blalakumhren, A.P., Saimurugan, M., Prakash Marimuthu K. (2019). Finite element simulation and experimental validation of the effect of tool wear on cutting forces in turning operation. *Mechanics and Mechanical Engineering*, vol. 23, no. 1, p. 297-302, **DOI:10.2478/mme-2019-0040**.

[7] Zhang, Q., Zhang, S., Li, J. (2017). Three dimensional finite element simulation of cutting forces and cutting temperature in hard milling of AISI H13 steel. *Procedia Manufacturing*, vol. 10, p. 37-47, **DOI:10.1016/j.promfg.2017.07.018**.

[8] Pattavanitch, J., Hinduja, S., Atkinson, J. (2010). Modelling of the electrochemical machining process by the boundary element method. *CIRP Annals*, vol. 59, no. 1, p. 243-246, **DOI:10.1016/j.cirp.2010.03.072**.

[9] Zhang, Y., Gu, Y., Chen, J.T. (2010). Boundary element analysis of the thermal behaviour in thin-coated cutting tools. *Engineering Analysis with Boundary Elements*, vol. 34, no. 9, p. 775-784, **DOI:10.1016/j.enganabound.2010.03.014**.

[10] Bartoszuk, M., Grzesik, W. (2011). Numerical prediction of the interface temperature using updated Finite Difference Approach, *CIRP Annals - Advanced Materials Research*, vol. 223, p. 231-239, **DOI:10.4028/www.scientific.net/AMR.223.231**.

[11] Niu, W., Mo, R., Liu, G.R., Sun, H., Dong, X., Wang, G. (2017). Modeling of orthogonal cutting process of A2024-T351 with an improved SPH method. *The International Journal of Advanced Manufacturing Technology*, vol. 95, p. 905-919, **DOI:10.1007/s00170-017-1253-6**.

[12] Bartoszuk, M. (2013). *Modeling of Heat Flow and Temperature Distribution in the Cutting Zone for Cemented Carbide Inserts*, Publishing House of the Opole University of Technology, Opole. (in Polish)

[13] Grzesik, W., Bartoszuk, M., Niesłony, P. (2004). Finite difference analysis of the Thermal bahaviour of coated tools in orthogonal cutting of steels. *International Journal of Machine Tools and Manufacture*, vol. 44, no. 14, p. 1451-1462, **DOI:10.1016/j.ijmachtools.2004.05.008**.

[14] Jam, J.E., Fard, V.N. (2011). A novel method to determine tool-chip thermal contact conductance in machining, *International Journal of Engineering Science and Technology*, vol. 3, no. 12, p. 8491-8501.

[15] Jin, D., Jingjie, Z., Liguo, W. (2018). Heat partition and rake face temperature in the machining of H13 steel with coated cutting tools. *The International Journal of Advanced Manufacturing Technology*, vol. 94, p. 3691-3702, **DOI:10.1007/s00170-017-1122-3**.

[16] Zhao, J., Liu, Z. (2019). Modelling for prediction of time-varying heat partition coefficient at coated tool-chip interface in continuous turning and interrupted milling. *International Journal of Machine Tools & Manufacture*, vol. 147, p. 1-10, **DOI:10.1016/j.ijmachtools.2019.103467**.

[17] Zemzemi, F., Rech, J., Ben Salem, W., Dogui, A., Kapsa, Ph. (2014). Identification of friction and heat partition model at the tool-chip-workpiece interfaces in dry cutting of an inconel 718 alloy with CBN and coated carbide tools. *Advances in Manufacturing Science and Technology*, vol. 38, no.1, p. 5-22, **DOI:10.2478/amst-2014-0001**.

[18] Abhang, L.B., Hameedullah, M. (2010). Chip-tool interface temperature prediction model for turning process. *International Journal of Engineering Science and Technology*, vol. 2, no. 4, p. 382-393.

[19] Niesłony, P. (2008). *Modeling of Heat Flow and Temperature Distribution in the Cutting Zone for Blades with Hard Protective Coatings*, Publishing House of Opole University of Technology, Opole. (in Polish)

[20] Markopoulos, A.P., Davim, J.P. (2018). *Advanced Machining Processes: Innovative Modeling Techniques*, CRC Press, Taylor & Francis Group, Boca Raton.

Strojniški vestnik - Journal of Mechanical Engineering 66(2020)11, 642-654,

DOI:10.5545/sv-jme.2020.6795 Original Scientific Paper
Received for review: 2020-06-01
Received revised form: 2020-07-14
Accepted for publication: 2020-07-14

Fundamentals of Odour Assessment in Slovenia

Martin Dobeic[1] – Vincenc Butala[2] – Matjaž Prek[2] – Jan Leskovšek[3] – Žiga Švegelj[3,*]
[1] University of Ljubljana, Veterinary Faculty, Slovenia
[2] University of Ljubljana, Faculty of Mechanical Engineering, Slovenia
[3] Studio okolje d.o.o., Slovenia

From a sociological and economic perspective, odour pollution is one of the most complex problems in the field of air quality. Therefore, various approaches and odour impact criteria are particularly relevant when assessing odour exposure in the areas of different land use. The number of odour assessment methods is limited, and the lack of analytical techniques to determine odour concentration makes odour assessment even more complex. It is essential to analyse the spatial and temporal distribution of odour concentrations in order to assess odour nuisance in the ambient air. Since sampling of odorous air in the field for subsequent determination of odour concentrations in a laboratory by dynamic olfactometry is time-consuming, two approaches are used to assess odour concentrations in ambient air: estimating odour concentration by field inspection and calculation of odour concentrations using atmospheric dispersion models. The latter is the most commonly used technique.

Our study aimed to provide fundamentals for an odour regulatory framework in Slovenia. While a multitude of approaches is presently applied to establish odour regulation framework, a broader approach remains lacking. Various odour emission sources were identified to evaluate available methods and techniques to assess odour impact. The impact area was selected to analyse and compare the impact of different odour sources in terms of odour concentration, odour frequency, odour offensiveness, land use, and receptor location. Finally, odour impact criteria were set according to odour offensiveness and concentration, percentile compliance level and land use.

Keywords: odour emission sources, odour concentration, odour nuisance, annoyance, impact assessment, offensiveness, 95th and 99th percentiles of odour perception, mathematical dispersion model

Highlights

- *The scope of the project was to provide fundamentals of odour assessment in Slovenia based on the evaluation of available methods and techniques and odour regulations in selected countries. The results presented in this paper are based on odour emission rates from various stationary industrial sources, in-field measurements of odour concentrations, and calculation of odour concentrations using the dispersion model.*
- *Evaluation and applicability of different odour assessment methods and related techniques were conducted in a selected assessment site with existing odour nuisance.*
- *Concentrations calculated using the dispersion model were compared against different odour impact criteria including odour concentration, odour offensiveness, percentile compliance level and land use.*
- *Odour impact criteria are recommended for odour regulatory purpose in Slovenia.*

0 INTRODUCTION

Odour nuisance is an ecological, economic, and social problem. Most countries, especially in the EU, regulate odour pollution according to country-specific odour impact criteria (OIC). These criteria consider the level of protection based on the land use, odour offensiveness, odour concentration threshold, and level of compliance expressed in terms of percentiles **[1]**. Due to meteorological and socio-economical differences in the individual countries, odour impact criteria can vary considerably. In contrast to the analytical approach in which the particular odorous compound is measured using physical and chemical methods, odour concentration is determined using sensorial methods for which the basis of the measurement are human assessors. In the EU countries, the primary method used to determine odour concentrations is dynamic olfactometry method specified in European standard EN 13725 **[2]**. According to this method, odour concentration is measured under laboratory conditions at room temperature and normal atmospheric pressure. The measurements are performed by qualified panel members who detect the odour threshold in samples presented by dynamic olfactometer.

Several different assessment criteria should be considered simultaneously to assess odour impact adequately. The concentration of the odour is determined quantitatively, and the hedonic tone is determined qualitatively; the duration of each odour episode is also an important factor. Uncertainties associated with the determination of the odour emission rates from existing sources depend mostly on the type of a source since the determination of volume flow rate from area and volume sources is more complex compared to point sources.

*Corr. Author's Address: Studio okolje d.o.o., Slovenia, ziga.svegelj@studiookolje.si

Determination of odour in ambient air by using the grid method [3] or portable olfactometer can be applied. However, both methods are time-consuming, and the former is also associated with high costs. Due to the lack of methods to determine the spatial distribution of odour concentration in the assessment area, dispersion modelling is the most widely used technique to assess odour impact from existing and new facilities [1]. A variety of input data, such as the type of emission source, odour emission rates, high-quality meteorological data, topographic data, and land use data, need to be provided to calculate odour concentration using models. Since the spatial distribution of odour concentration in ambient air, in addition to emission odour rate, depends mainly on the calculation of wind fields, coupling microscale diagnostic meteorological model and mesoscale prognostic meteorological model is recommended. Doing so allows for vertical temperature profile, related information on temperature inversion, and vertical wind profile to be used in the meteorological model on a local scale. Although the use of dispersion model has certain advantages over field inspection methods, the inaccuracy of calculated odour concentration can be significant. Therefore, it is highly relevant to compare and verify calculated odour concentrations against those obtained by field inspection.

In general, odour dispersion modelling is similar to dispersion modelling of various pollutants in ambient air. However, unlike the majority of pollutants, the odour can be perceived by the human nose. The response of an individual to odour exposure is subjective and depends on numerous factors related to the physiological state of the receptor. While breathing normally, an average healthy adult has a respiratory rate of 12 to 18 breaths per minute, meaning that the duration of a single breath is approximately 3 to 5 seconds [4]. This indicates that odour concentrations should be considered on the time scale of seconds instead of hours. To provide a short-term odour peak concentration, the so-called peak-to-mean method is used [5]. According to this method, odour peak concentration is calculated based on hourly mean concentration using the peak-to-mean ratio, in which the latter is defined as a relationship between peak and mean odour concentration. Several approaches are used to estimate the peak-to-mean ratio. For instance, in Germany, the ratio is defined as a constant value of 4 [6]. Many recent studies suggest that the ratio depends on atmospheric stability, the distance from the odour source, and on the length of the selected time interval to calculate short-term odour peak concentrations.

A relationship between peak and mean concentration is expressed as a power function [7]:

$$R_0 = \frac{C_p}{\bar{C}} = \left(\frac{t_m}{t_p} \right)^a , \quad (1)$$

where R_0 is a peak-to-mean factor, C_p short-term peak odour concentration, $\bar{C}$ long-term mean concentration, t_m long-term averaging time (usually 1 hour), t_p short-term averaging time, and exponent a is empirically determined atmospheric-stability dependent exponent factor [8]. During stable atmospheric conditions, the odour dispersion is limited and therefore, the ratio is small. In contrast, during the unstable atmospheric condition, the odour disperses in ambient air more sufficiently, and hence the ratio is significant. Since odour peak concentration is also dependent on the distance from the odour emission source, Eq. (1) can be formulated as [9] to [11]:

$$R(r) = 1 + (R_0 - 1) \cdot e^{-0.7317 \frac{T(r)}{t_l}} , \quad (2)$$

$T(r)$ represents the particle's travel time calculated using the distance from the odour source and the wind speed. Variable t_l is a measure of a Lagrangian time scale [12]. The latter represents the time over which the velocity of a particle is self-correlated or roughly the time over which a particle maintains its initial velocity before experiencing a turbulent collision [13]. The Lagrangian time scale is defined as a ratio between wind speed variance and the rate of dissipation of turbulent energy:

$$t_l = \frac{\sigma^2}{\varepsilon} = \frac{\frac{1}{3}\left(\sigma_u^2 + \sigma_v^2 + \sigma_w^2 \right)}{\frac{1}{kz}\left(\frac{\sigma_w}{1.3} \right)^3} , \quad (3)$$

where σ_u, σ_v, σ_w, are variances of wind speed by components, k is the von Karman constant, and variable z height of individual or more specifically the receptor's nose. According to [14], the distribution of odour concentration within an hour can be fitted using the modified two-parameter Weibull probability density function:

$$p(c) = \lambda k (\lambda k)^{k-1} e^{-(\lambda c)^k} , \quad (4)$$

$$k = \left(\frac{\bar{C}}{\sigma} \right)^{1.086} , \quad (5)$$

$$\lambda = \frac{\Gamma\left(1+ 1/k\right)}{\bar{C}}. \quad (6)$$

Eqs. (5) and (6) are used to calculate shape parameters k and λ, where a variable $\bar{C}$ is hourly mean concentration, σ standard deviation of odour concentration within an hour, and Γ Gamma function. Shape parameters k and λ are computed in post-processing using an analytical approach. Once these factors are computed, the 90th percentile of the cumulative frequency distribution of odour-concentration fluctuations or the peak-to-mean ratio is determined using:

$$R_{90} = \frac{\left(-\ln 0.1\right)^{\frac{1}{k}}}{\lambda \bar{C}}, \quad (7)$$

Such an approach is practical, as there is no need to modify the source code of the dispersion model, and it can be used in combination with various dispersion models. It should be noticed that odour-hour concept is applied in a German guideline VDI 3940 [15], where an odour-hour is defined as an hour that has recognizable odour for at least 10 % of the time [16], which implies that the 90th percentile of cumulative frequency distribution has to be calculated.

Providing methodology to assess odour impact and to ensure an adequate regulatory framework remains a relevant challenge on a global scale. While a multitude of different methodologies is presently applied to assess odour impact, a broader approach to this problem remains lacking. The so-called CICOP approach was established to evaluate the odour impact [17]. According to this approach, the concentration, intensity, character, offensiveness, and persistence of an odour should be determined to assess odour impact. A similar but complementary is the FIDOL approach, in which FIDOL refers to odour frequency, intensity, duration, offensiveness, and location of the receptor [18] and [19]. The FIDOL approach is the basis of numerous regulatory frameworks and the concept of odour impact criteria [20]. Once compared to the findings of dose-response studies, which analyse the population response to the odour exposure, the odour impact criteria can be applied to the regulatory framework to limit odour nuisance from existing facilities or to prevent odour nuisance in the planning stage of a new facility.

1 MATERIALS AND METHODS

1.1 Odour Emission Sources

In general, odour nuisance is caused by odour-emitting sources of anthropogenic origin. In contrast to odour emissions from natural sources, the odour emitted from industry can be regulated to prevent and minimize or at least mitigate odour impact. In this study, the odour impact of four different sectors classified according to similar functions was investigated (e.g., food, metal, rendering, waste services).

Due to the differences in odour characteristics and consequently odour impact, odour samples at 12 odour-emitting facilities from a total of 17 different odour sources were collected. These differ in terms of the type of a source (e.g., point, area, and volume), hedonic tone of the odour, and odour emission rate. The odour samples were classified into four categories from least to most offensive odour, based on the

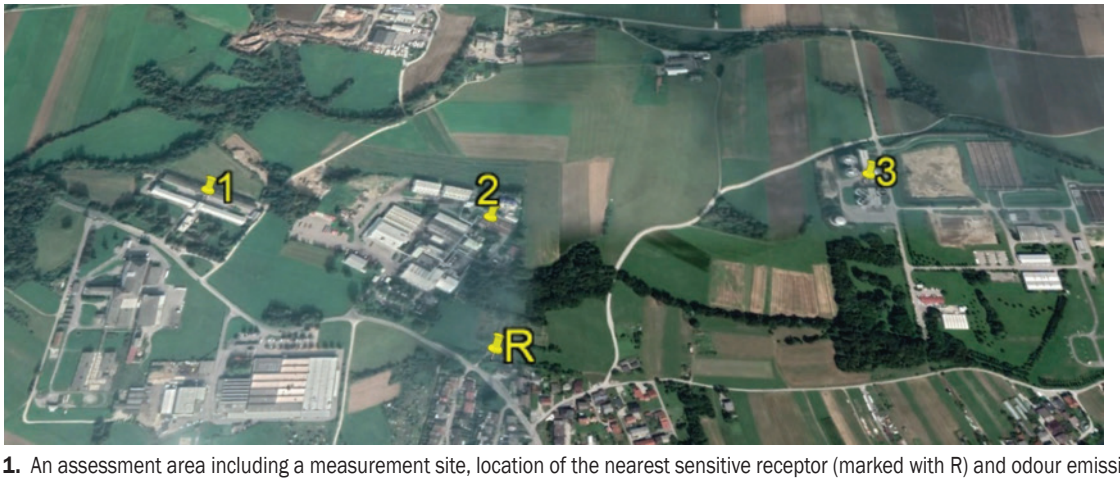

Fig. 1. An assessment area including a measurement site, location of the nearest sensitive receptor (marked with R) and odour emission sources, e.g., hen farm (marked with number 1), rendering plant (2), and municipal wastewater treatment plant (3)

hedonic tone (Table A1 in Appendix). Additionally, source data, such as location, dimension, height, as well as volume flow velocity, temperature and humidity of gas sample, were collected. Odour concentrations were determined under laboratory conditions using dynamic olfactometry, by which odorous samples were presented to qualified panel members. Odour emission rates were calculated using odour concentrations and characteristics of emission source.

In order to evaluate the impact of 17 different odour sources, an assessment area was selected. Measurements of meteorological parameters were carried out at a measurement site to obtain representative site-specific meteorological data. Applying such an approach enables the comparison of odour impact caused by different emission sources. The odour impact assessment was conducted in terms of odour concentration, odour offensiveness, different peak-to-mean ratios, and the residential area in which sensitive receptors are located. In the selected assessment area, three existing odour emitting facilities are located, while the nearest receptor is located at a distance of 200 metres from emission source, as shown in Fig. 1.

1.2 Meteorological Conditions

The dispersion of pollution in the atmosphere depends mainly on two physical processes: the advection of pollution downwind of the source and the dispersion of pollution transverse to the wind direction. While three-dimensional wind fields are required to describe advection, the dispersion depends on the atmospheric stability. Meteorological parameters, such as wind, air temperature, relative humidity, and air pressure, were recorded for 11 months at 10-minute intervals, to obtain representative site-specific meteorological data. Wind measurements in three dimensions were carried out using an ultrasonic anemometer. The measure of atmospheric stability in terms of Monin Obukhov length and standard deviation of vertical wind speed was derived from data collected by an ultrasonic anemometer. The analysis of meteorological data presented in Fig. 2 indicates a dominant north-east (N-E) winds and frequent low wind speeds. During the measurement period, the wind speed was below 1 m/s 49 % of the time. Due to a substantial percentage of time with low wind speeds and consequently a stable condition in the atmosphere, the dispersion of pollution is limited. Meandering, i.e., low-frequency horizontal wind oscillations, weak, layered, and intermittent turbulence occur in such meteorological conditions [21], which results in inhomogeneous and non-stationary wind fields, which are more complex to compute.

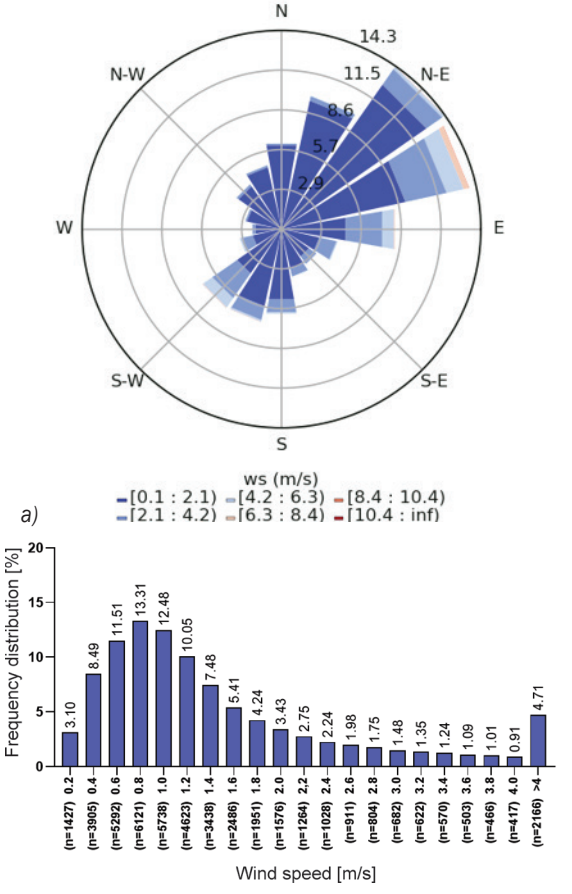

Fig. 2. *a) A wind rose, and b) wind speed (ws) frequency distribution at the measurement site in which parameter n represents the number of measurements in each class interval*

1.3 In-Field Determination of Odour

The method of in-field determination of odour concentration using portable olfactometer is based either on diluting the ambient odorous air by odourless air compressed in a gas cylinder or by filtering ambient odorous air using carbon adsorption bed [22]. Both approaches allow the determination of odour concentration in-situ, withdrawing the need of collecting odorous air in a sampling bag for subsequent olfactometry in a laboratory. The determination of odour concentration is conducted by an assessor, who is qualified according to requirements specified in the EU standard of dynamic olfactometry. The main disadvantage of portable olfactometers are their uncertainties associated with dilution technique as inaccuracy of dilution ratios

can be significant. Due to this issue, the performance of portable olfactometers has to evaluated using the gas analyser and certified test gas on a regular basis. Although in-field olfactometry is not standardized, it can be useful as complementary information for validation of dispersion models.

Prior to field inspection, the performance of portable olfactometer was evaluated using the calibrated gas analyser and a certified gas cylinder containing hydrogen sulphide. Six series of field inspection was conducted in a so-called Assessment area (Fig. 1), where 26 odour assessment locations within a grid of 2.65 km × 1.4 km with a resolution of 70 m were selected. In each of these locations, odour concentration over a period of 3 to 10 minutes was assessed, while the duration of each field inspection was 2 hours. In order to determine odour peak concentration, field inspections were performed considering local meteorological conditions and the official weather forecast of Slovenian environmental agency.

1.4 Dispersion Modelling

The modelling system CALPUFF/CALMET [23] and [24], which consists of a Lagrangian puff dispersion model and diagnostic mass-consistent meteorological model, was applied to assess the spatial and temporal distribution of odour concentrations. According to the EPA (US), the CALPUFF/CALMET modelling system is recommended for simulating the dispersion of pollutants over complex terrain, where topographic features might generate light or calm local winds and circulations. In order to compute three-dimensional wind fields, a microscale CALMET diagnostic model and mesoscale ALADIN/SI numerical weather prediction model were coupled. As the input for the CALMET model, the meteorological data series including site-specific meteorological data obtained by ground station and vertical temperature and wind profiles computed with the ALADIN/SI numerical weather prediction model was provided.

For the purpose of the odour impact evaluation in the assessment area, the modelling domain in the size of 4.8 km × 4.8 km and horizontal grid resolution of 40 m was introduced. The modelling domain and grid resolution as configurated in CALPUFF/CALMET modelling system are illustrated in Fig. 3b, while the grid resolution of the mesoscale numerical prediction model, which is 4.4 km, is illustrated in Fig. 3a. Fig. 3b also shows areas of different land use; residential areas are coloured in grey, cultivation areas in brown, and forest in green. The red placemark represents the emission source location. This location was chosen to assess and compare the odour impacts of 17 different emission sources.

1.5 Odour Impact Criteria

The odour impact of 17 emission sources specified in Section 2.1 was evaluated using so-called odour-hours, which implies that the 90th percentile of cumulative frequency distribution has to be calculated.

Therefore, to assess the odour impact adequately, it is essential to provide peak concentrations within an hour. These are calculated by utilizing hourly odour concentrations using the peak-to-mean method. The relationship between peak concentration and hourly average concentration is known as the peak-to-mean ratio (R). Due to a comparison of different approaches to assessing the peak-to-mean ratio, hourly odour concentrations were modified applying constant peak-to-mean R factor [6], empirically determined R factor, and analytically derived R factor. According to [7], R factor considers atmospheric stability, while R factor according to [9] and [14] considers atmospheric stability and distance from an emission source. Comparison of calculated R factors using

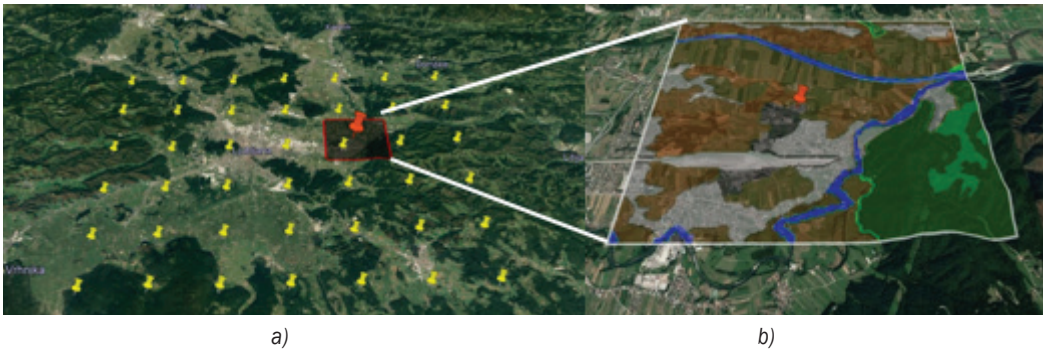

a) *b)*

Fig. 3. *Modelling domain; a) horizontal grid resolution, b) emission source location, and land use*

different methods is presented in Table 1, where t_p presents short-term averaging time. Note that the dispersion model simulations provided mean odour concentrations for an averaging time of an hour.

Table 1. *Comparison of calculated R factors using different methods*

	Short-term averaging time t_p							
	5 s		1 minute		3 minutes		6 minutes	
Method	min	max	min	max	min	max	min	max
[7]	3.3	87.7	2.1	16.2	1.7	7.4	1.5	4.8
[9]	1.0	84.8	1.0	15.7	1.0	7.4	1.0	4.4
[14]	1.5	169.0	1.5	17.9	1.5	7.0	1.5	4.0

Regarding Table 1, the differences between minimum and maximum R factors can be significant. Since it was concluded that modelled odour concentrations utilizing a short-term time interval of less than 6 minutes would be overestimated, we opted for the latter.

Two levels of protection against odour nuisance based on land use were introduced to evaluate the odour impact in the assessment area. The highest level of protection includes residential areas, holiday homes, health infrastructure, and social institutions, recreation and sports areas, parks, gardens, cemeteries, and tourist resorts. In contrast, the low level of protection includes various areas with industrial facilities, roads, agricultural land, and mining areas.

Furthermore, the odours were classified according to their hedonic tone (offensiveness), which is a measure of pleasantness or unpleasantness of an odour at a given concentration. The classification of odour emission sources, according to the odour offensiveness, is summarized in Table 2.

Table 2. *Classification of emission sources according to the odour offensiveness*

Odour offensiveness level	Emission source
Low	Fodder mixing plant, Foundry, Bakery, Coffee roasting facility
Medium	Poultry farm, Broiler farm, Municipal wastewater treatment plant
High	Pig farm, Red meat slaughterhouse, Brewery
Extreme	Biogas plant, Rendering plant

The criteria for the classification of odour sources in terms of odour offensiveness were based on VDI 3882, Part 2 [25] and our experiences since all of the emission sources are the reason for a large number of public complaints in Slovenia.

Finally, the odour impact assessment of 17 emission sources was conducted considering the odour concentration threshold, odour offensiveness and, percentile compliance level. The frequency of odour episodes was analysed through variation of the percentile level.

1.6 Appendix

The appendix to the article contains Table A1 as odour emission source classification with data on emission sources. Fig. A1 represents a comparison of odour emission rates. In the appendix evaluation between groups of odour emission rates and between groups of in-field odour concentrations using portable olfactometer are included.

2 RESULTS AND DISCUSSION

2.1 Determination of Odour Emission Rates

While uncertainties related to the determination of odour emission rates from point and area sources are fairly manageable, the same cannot be said for volume sources where fugitive emissions frequently occur. A total of 17 different emission sources observed in this study. They were collected at 11 point sources and 6 area sources (Table A1: Types and dimensions of emission sources and 3 volume sources described in the appendix). It should be noted that according to [26] emission sources can be classified as active or passive, depending on the velocity of the waste gas at the release. If the velocity is greater than 30 m/h, the source is considered active; otherwise, the source is passive. According to this definition, ventilation ducts at the hen, broiler, and pig farm, bakery, coffee roasting plant, brewery, foundry, and stack at biogas power plant were classified as point sources, the biofilter at a rendering facility, oxygenation and sludge tanks at the wastewater treatment plant, fodder mixing plant, and mixing tank at biogas plant as area sources, while storage facilities for sludge and hides at a rendering facility, and a slaughterhouse as volume sources. (Table A1 in the appendix: Types and dimensions of emission sources, and measurements of temperature and humidity of waste gas, Fig. A1 in the appendix: Comparison of odour emission rates). Emission rates from these sources are illustrated in Fig. 4.

The comparison shows that odour emissions from sources such as biogas power plant, brewery, coffee roasting plant and pig farm are extremely high and higher (P = 0.076) than the others. If a facility generating odour nuisance is exposed in public,

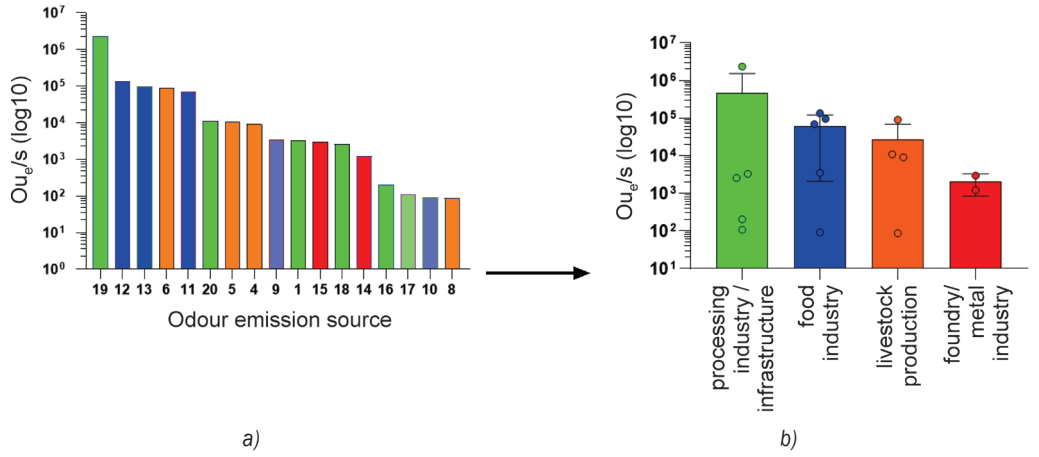

a) *b)*

Fig. 4. *a) Odour emission (Ou$_e$/s) by source classification: biofilter at animal by-products processing plant (1), hen farm (4), broiler farm (5), pig farm (6), fodder mixing plant (8), bakery: ventilation duct – baking (9), ventilation duct- mixing process (10), ventilation duct at coffee-roasting plant (11), brewery ventilation ducts (12, 13), foundry – ventilation ducts on the rooftop (14, 15), sludge thickener at the municipal wastewater treatment plant (16), sludge thickener at the municipal wastewater treatment plant (17), oxygenation tank at the municipal wastewater treatment plant (18), stack at the biogas power plant (19), mixing tank at the biogas power plant (20); b) the mean value of emissions grouped by industry type*

authorities take action and start the abatement process to tackle odour nuisance. Among all emission sources, estimating emission rates from volume sources was most challenging as fugitive emissions were identified. Therefore, reverse modelling was applied to evaluate emission rates from those sources. However, this is not the optimal solution to the problem as uncertainties associated with such an approach can be significant. An odour concentration as Ou$_e$/m^3 (Ou - European odour unit per cubic metre, e - EROM (European Reference Odour Mass)) and odour emission rate as Ou$_e$/s (European odour unit per second) can be determined more adequately by converting a volume source into a point source. This can be achieved by providing negative air pressure, i.e., to provide lower pressure than of the surroundings, and use single or multiple stacks to control the release of odorous gas.

2.2 In-Field Olfactometry

The results of field inspection using portable olfactometer in the assessment area indicate odour nuisance in the vicinity of all three odour sources, i.e., hen farm, rendering plant, and wastewater treatment plant, present in this area (see Fig. 1). The highest odour concentrations were estimated adjacent to the rendering plant, which were significantly higher ($P <$ 0.0001) than the other odour concentrations adjacent to the hen farm and wastewater treatment plant (Fig. 5). The odour peak concentration of 19 Ou$_e$/m^3 was assessed outside the rendering facility fence line 100 metres from the majority of odour sources. Further downwind from rendering facility, odour concentrations decreased rapidly. At a distance of 200 metres odour concentrations did not exceed 7 Ou$_e$/m^3, at the distance of 300 m, where the nearest sensitive receptor is located 3 Ou$_e$/m^3, and at a distance of 400 m 2 Ou$_e$/m^3. At the distance of 500 m, the odour concentrations did not exceed the odour threshold of 1 Ou$_e$/m^3 during field inspections.

2.3 Dispersion Modelling

The results of dispersion modelling were analysed and compared in terms of land use (level of protection against odour nuisance), odour offensiveness, and level of compliance. The latter was expressed in percentiles and varied in the range between 99th and 90th percentile. Odour concentrations were compared at the nearest sensitive receptor, which is located 300 m from the rendering plant. Fig. 6 illustrates odour concentrations at the 99th and 95th percentiles in the assessment area where 3 existing odour sources (i.e. hen farm, the rendering plant and municipal wastewater treatment plant) are located. The comparison shows that odour concentrations at 99th percentile exceed odour threshold of 1 Ou$_e$/m^3 2000 m downwind of rendering facility, while those at 95th percentile exceeded 1 Ou$_e$/m^3 1000 m downwind of the rendering facility.

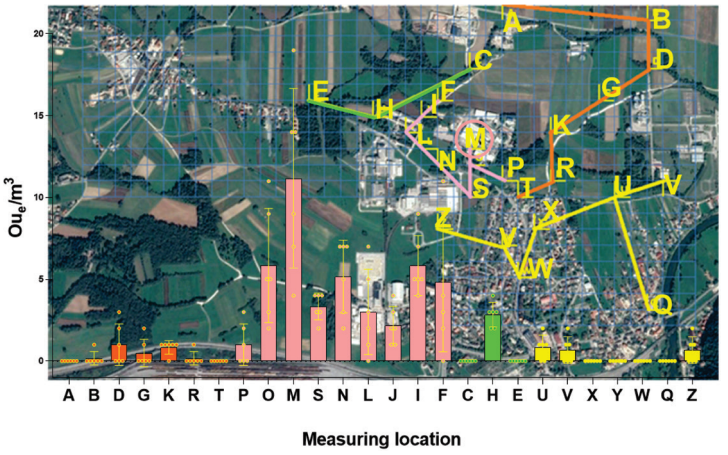

Fig. 5. *In-field odour concentration assessment using portable olfactometer. Odour concentration was assessed at 26 odour locations within a grid of 2.65 km × 1.4 km and a resolution of 70 m; green lines indicate the alleged impact of the chicken farm, pink lines indicate the impact of the rendering plant, orange lines indicate the alleged impact of the wastewater treatment plant, yellow lines indicate the impact to nearby settlements; M indicates the highest measured concentration near the biofilter of the rendering plant*

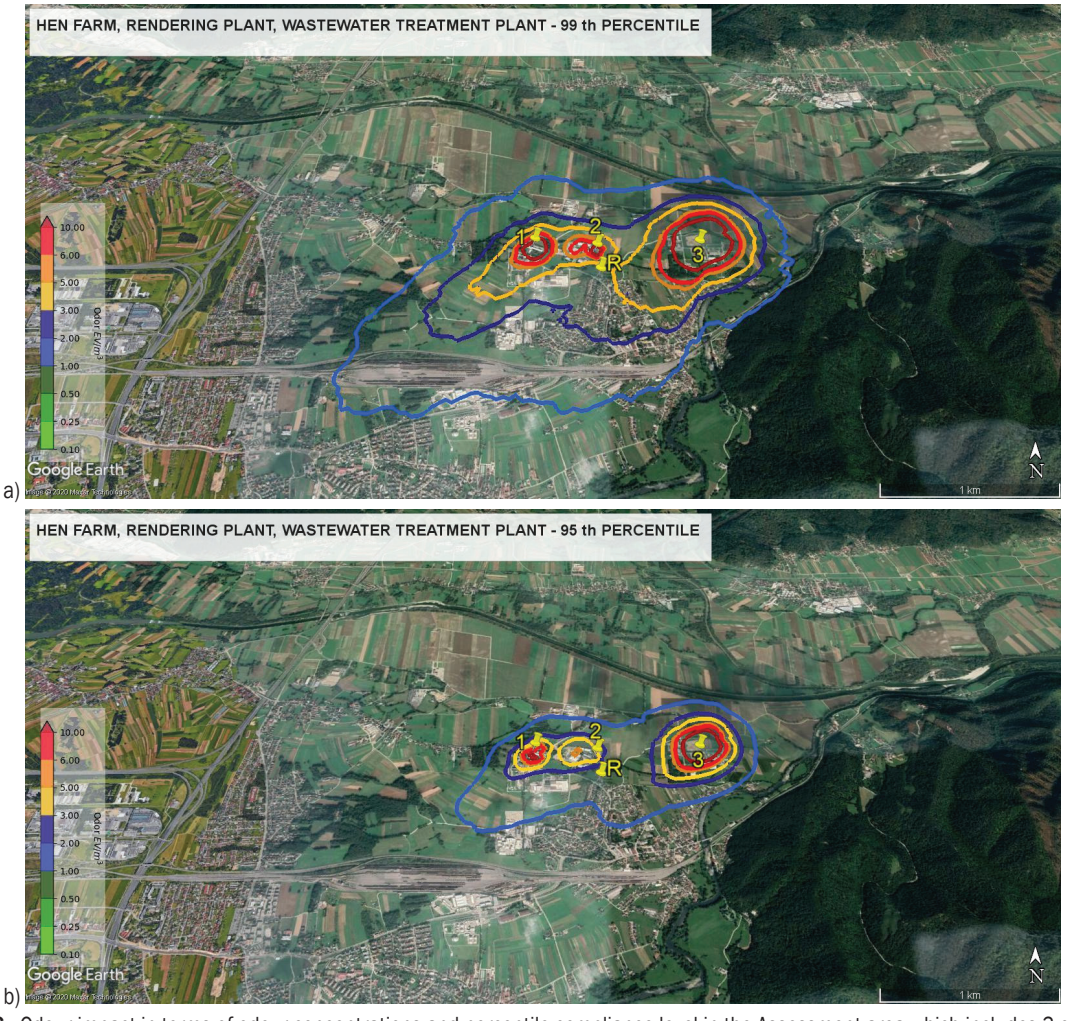

Fig. 6. Odour impact in terms of odour concentrations and percentile compliance level in the Assessment area which includes 3 odour sources, i.e., hen farm, the rendering plant, and municipal wastewater treatment plant (these are also shown in Fig. 1); a) illustrates odour concentrations at the 99th percentile, while b) at 95th the percentile

Furthermore, the odour impact of the other odour sources listed in Section 2.1. was evaluated. The impact of each odour source was evaluated in the Assessment area. Odour sources were positioned in the location of the rendering facility. Comparison of odour concentrations at the nearest sensitive receptor 300 m downwind of the source is shown in Fig. 7, where odour offensiveness thresholds are introduced. Fig. 7a shows that odour concentrations generated by the coffee roasting facility at the 99th and 95th percentiles would exceed 4 Ou_e/m^3, which was recommended threshold concentration for odour with low offensiveness. Odour concentrations generated by a wastewater treatment plant would exceed threshold concentration of 3 Ou_e/m^3at both 99th and 95th percentile, while odour impact of other odour sources in the group of moderately offensive odours would be within recommended threshold values. Highly (Fig. 7c) and extremely (Fig. 7d) offensive odours generated by the slaughterhouse, brewery, biogas power plant, and biofilter at rendering facility would exceed recommended odour threshold of 2 Ou_e/m^3 and 1 Ou_e/m^3 at 99th and 95th percentile. It can be concluded that these sources would exceed threshold limits even if the location of the nearest sensitive receptor would be within level II of protection against odour nuisance.

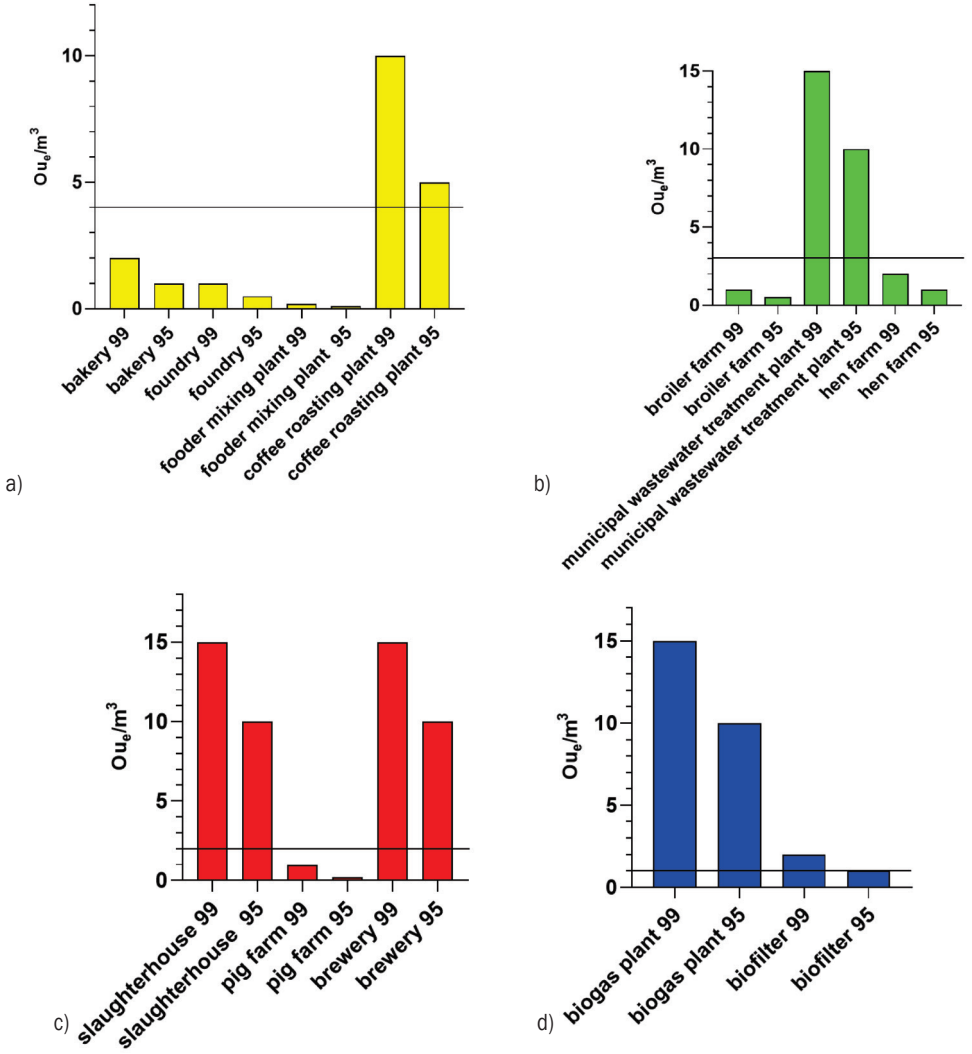

Fig. 7. *Odour concentrations in terms of odour compliance level in percentile and odour offensiveness; a) a threshold of 1 Ou_e/m^3 for extremely offensive odours, b) a threshold of 2 Ou_e/m^3 for highly offensive odours, c) a threshold of 3 Ou_e/m^3 for moderately offensive odours, and d) a threshold of 4 Ou_e/m^3 for low offensive odours; the nearest sensitive receptor located 300 m downwind of the odour source*

On the basis of presented analysis, odour impact criteria for existing and new facilities were recommended to establish a regulatory framework. The impact criteria are summarized in Tables 3 and 4.

Table 3. *Odour impact criteria for level I protection areas*

Odour offensiveness	Threshold concentration [Ou_e/m^3]	Percentile compliance level, existing facilities	Percentile compliance level, new facilities
low	4	98	99
medium	3	98	99
high	2	98	99
exceptional	1	98	99

Table 4. *Odour impact criteria for level II protection areas*

Odour offensiveness	Threshold concentration [Ou_e/m^3]	Percentile compliance level, existing facilities	Percentile compliance level, new facilities
low	4	90	95
medium	3	90	95
high	2	90	95
exceptional	1	90	95

3 CONCLUSION

Various emission sources were identified in terms of odour emission, odour offensiveness, and type of emission source in order to address odour management. Among several emission sites, a single assessment area was selected to evaluate the impact of the individual odour source. The odour impact of 17 emission sources was compared against commonly used criteria, which is provided by regulatory frameworks to assess the impact of existing facilities or to prevent potential odour nuisance in the planning stage of a new facility. As the representativeness of dispersion model simulations depends mainly on the input data, 11-month site-specific meteorological data, type of land use and topographical data were provided. A diagnostic meteorological model and a mesoscale prognostic meteorological model were coupled to compute wind fields. Hourly mean concentrations were calculated using the dispersion model, while short-term peak concentrations were provided using various peak-to-mean methods. Additionally, in-situ odour concentrations were estimated using portable olfactometer.

Odour impacts of emission sources were compared in terms of odour concentration generated by a particular source, odour offensiveness and level of compliance in percentile. Whereas the latter was varied in the range from 90^{th} to 99.9^{th} percentiles, odour concentration was analysed 300 metres downwind of emission source at the nearest receptor. On the basis of this analysis, odour impact criteria for a different type of land use and existing or new facility were specified.

While dispersion models are a very useful tool for odour impact assessment, the verification of their results requires more research in the future. In particular, the assessment of odour impact by various field inspection methods and dose-response studies should be conducted.

4 ACKNOWLEDGEMENTS

The research was funded by the Ministry of Environment and Spatial Planning of the Republic of Slovenia.

5 APPENDIX

Table A1. *Odour emission source classification with data of emission sources: biofilter at animal by-products processing plant (1), storage facility for hides at animal by-products processing plant (2), storage facility for waste sludge at animal byproduct-processing plant (3), hen farm (4), broiler farm (5), pig farm (6), slaughterhouse (7), fodder mixing plant (8), bakery: ventilation duct – baking (9), ventilation duct - mixing process (10), ventilation duct at coffee roasting plant (11), brewery ventilation ducts (12, 13), foundry – ventilation ducts on the rooftop (14, 15), sludge thickener at the municipal wastewater treatment plant (16), sludge thickener at the municipal wastewater treatment plant (17), oxygenation tank at the municipal wastewater treatment plant (18), stack at biogas power plant (19), mixing tank at biogas power plant (20)*

Emission source	Type of emission source	Source height [m]	Cross section / area / volume of the source	# of sources	Waste gas temperature [°C]	Relative humidity of waste gas [%]	Flow rate [m^3/h]	Odour concentration [Ou_e/m^3]	Odour emission rate [Ou_e/s]
1	area	2	1.000 m^2	1	23.7	78	95.000	126	3.325
2	volume	/	20.000 m^3	1	/	/	/	954	/
3	volume	/	12.000 m^3	1	/	/	/	2.048	/
4	point	1; 3; 6	0.16 m^2	36	30.5	49	5.040	181	9.122

Emission source	Type of emission source	Source height [m]	Cross section / area / volume of the source	# of sources	Waste gas temperature [°C]	Relative humidity of waste gas [%]	Flow rate [m³/h]	Odour concentration [Ou_e/m^3]	Odour emission rate [Ou_e/s]
5	point	1,5	1.45 m²	2	26.6	58	48.566	406	10.954
6	point	6	0.50 m²	36	23.7	58	17.690	512	90.573
7	volume	/	2.100 m³	1	17.5	62	/	16.402	/
8	area	1,5	1.200 m²	1	24.3	51	4.920	64	87
9	point	10	0.26 m²	1	31.0	49	6.176	2.048	3.513
10	point	10	0.2 m²	1	29.7	46	2.334	142	92
11	point	20	0.385 m²	1	42.1	27	8.472	29.670	69.823
12	point	17	0.283 m²	1	87.9	100	626	781.456	135.886
13	point	15	2.64 m²	3	31.6	47	7.968	14.596	96.917
14	point	16	1.9 m²	11	27.6	54	1.402	287	1.229
15	point	18	0.25 m²	7	24.5	60	13.428	114	2.977
16	area	15	48 m²	1	27.6	70	1.440	512	205
17	area	15	48 m²	1	26.8	81	1.440	271	108
18	area	1	7.500 m²	1	12.1	87	30.750	303	2.588
19	point	25	0.385 m²	1	31	74	9.286	917.204	2.365.877
20	area	0	2 m²	2	242	64	16	1.258.200	11.184

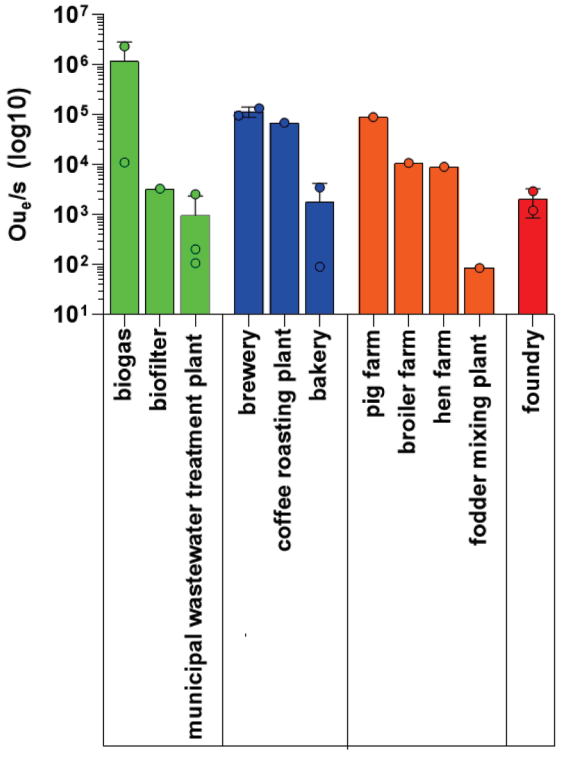

Fig. A1. *Comparison of odour emission rates*

Evaluation between groups of odour emission rates:

Column B: biogas, brewery, pig farm, coffee roasting plant (Sample size $n = 4$) as highest measured emissions vs. Column A: rest/other (Sample size $n = 11$). At Fig. A2 actual values are on the horizontal axis, and the predicted values (assuming sampling from a Gaussian distribution) are on the vertical axis. Since the data were not sampled from a Gaussian (normal) distribution, the points were not following a straight line that matches the line of identity

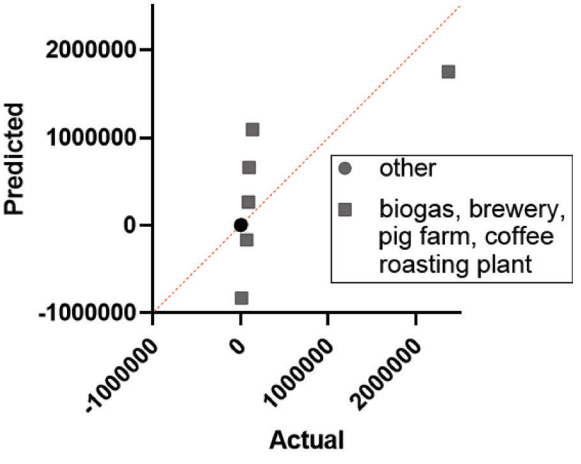

Fig. A2. QQ plot of a normality test (Column A, Column B);

Unpaired *t* test:

where P value is 0.0759, P value summary not significant (ns), not significantly different ($P < 0.05$), two-tailed P value, and $t = 1.929$ and $df = 13$.

How big is the difference?

The mean of column A is 61023 while the mean of column B is 2554550. Difference between means (B – A) ± SEM is 2493526 ± 1292932, 95 % confidence interval is between –299683 and 5286736. R squared (eta squared) is 0.2225.

F test:

To compare variances, where $F = 2106$, $DFn = 3$, $Dfd = 10$, P value is <0.0001 and significantly different ($P < 0.05$).

Evaluation between groups of in-field odour concentrations using portable olfactometer:

Column A: P-F (Sample size $n = 54$) as the highest measured concentrations vs. Column B: A-T and C-Z (Sample size $n = 102$)

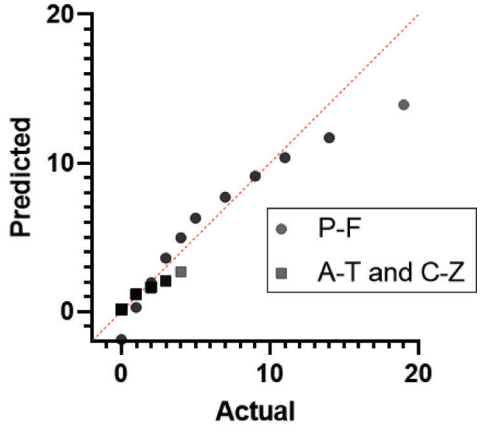

Fig. A3. *This figure presents a QQ plot of the normality test (Column A, Column B)*

At Fig. A3 actual values are on the horizontal axis, and the predicted values (assuming sampling from a Gaussian distribution) are on the vertical-axis. Since the data were sampled from a Gaussian (normal) distribution, the points were following a straight line that matches the line of identity

Unpaired *t* test:

where *P* value is < 0.0001, significantly different ($P < 0.05$), two-tailed *P* value, $t = 10{,}52$ and $df = 154$.

How big is the difference?

The mean of column A is 4.704, the mean of column B 0.4510, the difference between means (B - A) ± SEM –4.253 ± 0.4042, 95 % confidence interval is between–5.051 and –-3.454 and *R* squared (eta squared) is 0.4182.

F test:

to compare variances: $F = 20.59$, $DFn = 53$, $Dfd = 101$, P value is < 0.0001 and significantly different ($P < 0.05$).

6 REFERENCES

[1] Brancher, M., Griffiths, K.D., Franco, D., de Melo Lisboa, H. (2017). A review of odour impact criteria in selected countries around the world. *Chemosphere*, vol. 168, p. 1531-1570, **DOI:10.1016/j.chemosphere.2016.11.160**.

[2] EN 13725:2006. *Stationary Source Emissions - Determination of Odour Concentration by Dynamic Olfactometry and Odour Emission Rate from Stationary Sources.* European Committee for Standardization, Brussels.

[3] EN 16842:2016. *Ambient Air. Determination of Odour in Ambient Air by Using Field Inspection – Part 1: Grid method.* European Committee for Standardization, Brussels.

[4] Barret, K.E., Barman, S.M., Boitano, S., Brooks, H.L. (2012). *Ganong's Review of Medical Physiology*, McGraw-Hill, New York.

[5] Schauberger, G., Piringer, M., Petz, E. (2001). Separation distance to avoid odour nuisance due to livestock calculated by the Austrian odour dispersion model (AODM). *Agriculture, Ecosystems & Environment*, vol. 87, no, 1, p. 13-28, **DOI:10.1016/s0167-8809(00)00299-1**.

[6] Janicke, L., Janicke, U., Ahrens, D., Hartmann, U., Müller, W.J. (2004). Development of the Odour Dispersion Model AUSTAL2000G in Germany. *Environmental Odour Management,* VDI-Berichte 1850, p. 411-417.

[7] Smith, M. (1973). *Recommended Guide for the Prediction of the Dispersion of Airborne Effluents*. American Society for Mechanical Engineers, New York.

[8] Beychok, M.R. (1979). *Fundamentals of Stack Gas Dispersion*. M.R. Beychok, Newport Beach.

[9] Piringer, M., Petz, E., Groehn, I., Schauberger, G. (2007). A sensitivity study of separation distances calculated with the Austrian Odour Dispersion Model (AODM). *Atmospheric Environment*, vol. 41, no. 8, p. 1725-1735, **DOI:10.1016/j.atmosenv.2006.10.028**.

[10] Piringer, M., Knauder, W., Petz, E., Schauberger, G. (2014). Site-dependent decrease of odour-related peak-to-mean factors with distance. *Advances in Science and Research*, vol. 11, p. 69-73, **DOI:10.5194/asr-11-69-2014**.

[11] Piringer, M., Knauder, W., Petz, E., Schauberger, G. (2015). A comparison of separation distances against odour annoyance calculated with two models. *Atmospheric Environment*, vol. 116, p. 22-35, **DOI:10.1016/j.atmosenv.2015.06.006**.

[12] Mylne, K.R. (1992). Concentration fluctuation measurements in a plume dispersing in a stable surface layer. *Boundary-Layer Meteorology*, vol. 60, p. 15-48, **DOI:10.1007/BF00122060**.

[13] Daoud, W.Z., Kahl, J.D.W., Ghorai, J.K., (2003). On the synoptic-scale Lagrangian autocorrelation function. *Journal of Applied Meteorology*, vol. 42, no. 2, p. 318-324, **DOI:10.1175/1520-0450(2003)042<0318:0TSSLA>2.0.C0;2**.

[14] Oettl, D., Ferrero, E. (2017). A simple model to assess odour hours for regulatory purposes. *Atmospheric Environment*, vol. 155, p. 162-173, **DOI:10.1016/j.atmosenv.2017.02.022**.

[15] VDI 3940, Part 1. 2006. *Measurement of odour impact by field inspection – Measurement of the impact frequency of recognizable odour. Grid measurement*. VDI-Verlag, Duesseldorf, Germany, GmbH.

[16] GOAA (2008). *Determination and Evaluation of Odour Immissions – Guideline on Odour in Ambient Air –. Detection and Assessment of Odour in Ambient Air.* (https://mma.gob.cl/wp-content/uploads/2017/06/Detection-and-Assessment-of-Odour-in-Ambient-Air.pdf).

[17] Gostelow, P., Parsons, S.A., Stuetz, R.M., (2001). Odour measurements for sewage treatment works. *Water Research*, vol. 35, no. 3, p. 579-597, **DOI:10.1016/S0043-1354(00)00313-4**.

[18] Watts, P.J., Sweeten, J.M. (1995). Toward a better regulatory model for odour. *Proceedings of the Xth Feedlot Association of Australia Conference*, Benowa.

[19] Freeman, T., Cudmore, R. (2002). Review of odour management in New Zealand. *Air Quality Technical Report 24. New Zealand Ministry of Environment*, Wellington.

[20] Griffiths, K.D. (2014). Disentangling the frequency and intensity dimensions of nuisance odour, and implications for jurisdictional odour impact criteria. *Atmospheric Environment*, vol. 90, p. 125-132, **DOI:10.1016/j.atmosenv.2014.03.022**.

[21] Anfossi, D., Oettl, D., Degrazia, G.A. (2004). Some aspects of turbulence and dispersion in low wind speed conditions. *Air Pollution Modelling and Its Application XVI*, p. 331-338, **DOI:10.1007/978-1-4419-8867-6_30**.

[22] Walgraeve, C., Van Hufffel, K., Bruneel, J., Van Langenhove, H. (2015). Evaluation of the performance of field olfactometers by selected ion flow tube mass spectrometry. *Biosystem Engineering*, vol. 137, p. 84-94, **DOI:10.1016/j.biosystemseng.2015.07.007**.

[23] Scire, J.S., Strimaitis, D.G., Yamartino, R.J. (2000). A *User's Guide for the CALPUFF Dispersion Model*. Version 5, Earth Tech, Inc., Concord.

[24] Scire J.S., Robe F.R., Fernau M.E., Yamartino R.J. (2000). *A User's Guide for the CALMET Meteorological Model*. Version 5, Earth Tech, Inc.

[25] VDI 3882-2 (1994). *Olfactometry - Determination of Hedonic Odour Tone*. Verein Deutscher Ingenieure, Duesseldorf.

[26] VDI 3880 (2011). *Olfactometry Static Sampling*. Verein Deutscher Ingenieure, Duesseldorf.

Strojniški vestnik - Journal of Mechanical Engineering 66(2020)11, 655-667
DOI:10.5545/sv-jme.2020.6868
Original Scientific Paper
Received for review: 2020-07-20
Received revised form: 2020-10-02
Accepted for publication: 2020-10-13

A Loaded Analysis Method for RV Cycloidal-pin Transmission Based on the Minimum Energy Principle

Tianxing Li[1,2,*] – Hang Xu[3] – Meng Tian[2]

[1] Henan University of Science and Technology, School of Mechatronics Engineering, China
[2] Collaborative Innovation Center of Machinery Equipment Advanced Manufacturing of Henan Province, China
[3] Zhongyuan University of Technology, School of Mechatronics Engineering, China

Due to the complexity of load distribution and contact conditions, as well as the lack of effective analysis methods, the theoretically designed rotary vector (RV) cycloidal-pin drive with good meshing characteristics shows poor loaded performance in practical applications. In this paper, an effective analysis method based on the minimum energy principle is proposed, which can accurately obtain the real loaded characteristics in line with the actual operations. In the process of loaded analysis, through the innovative introduction of the minimum energy principle, the actual number of teeth engaged simultaneously was accurately determined, which directly affects the quality of meshing. The results of simulation and measurement experiment demonstrate the correctness and practicability of the theoretical analysis method and the effectiveness of the introduction of the minimum energy principle. This study solves the problem that the actual meshing performance is inconsistent with the theoretical analysis results, and provides an effective way for the improvement and pre-control of the transmission accuracy and meshing quality of the robot RV reducer.

Keywords: cycloidal-pin gear, loaded characteristics, minimum energy principle, rotary vector (RV) reducer, transmission error

Highlights

- *An analysis method based on the minimum energy principle is proposed, which can accurately obtain the real loaded characteristics in line with the actual operations of the RV transmission.*
- *Through the innovative introduction of the minimum energy principle, the actual number of teeth engaged simultaneously is accurately determined.*
- *The possible meshing teeth and their numbers are quickly estimated according to the distribution of the minimum meshing clearance and the maximum deformation of the cycloidal-pin gear.*
- *The nonlinear mathematical relationship between the meshing load and the deformation is established.*

0 INTRODUCTION

The rotary vector (RV) reducer, accounting for about 38 % of the total cost, is the core component of a robot [1] and [2]. The RV reducer is mainly composed of a two-stage mechanism. The cycloidal-pin gear at the low-speed stage is directly connected to the output shaft, so its transmission performance determines the output accuracy of a reducer [3] and [4], which directly affects the motion accuracy, repeated positioning accuracy and service life of the robot.

One of the main features of cycloidal-pin transmission is simultaneous multi-tooth engagement. The error equalization effect generated by multi-tooth meshing is conducive to improving the transmission accuracy, which allows high meshing rigidity and large carrying capacity. However, due to the complicated load distribution and contact conditions of the cycloidal-pin gear with simultaneous multi-tooth meshing, as well as the lack of effective load analysis methods, the theoretically designed RV mechanism with good meshing characteristics shows poor load performance in practical applications. Low transmission precision, insufficient bearing capacity, and short accuracy retention are common problems to be solved in RV transmission.

Many researchers have conducted in-depth studies on the meshing characteristics of cycloidal-pin drives. Lin et al. [1] analysed the kinematic characteristics of the cycloidal drive by using the tooth contact analysis. Through analysing the contact dynamics in a cycloidal-pin transmission, Xu et al. [3] concluded that multi-tooth meshing characteristics have the main influence on the kinematic accuracy and the contact force. Based on unloaded and loaded contact analyses of the cycloid speed reducer, Li et al. [5] predicted the loads on various components in the presence of clearances and eccentricity errors. Li et al. [6] proposed an unloaded meshing analysis method for RV cycloidal-pin drive considering the influence of manufacturing errors. Based on the influence coefficient method, Huang and Tsai [7] proposed a computerized approach of loaded tooth contact analysis for the contact tooth pairs of the involute stage and the cycloid stage. Demenego et al. [8] developed a computer program for tooth contact analysis, which

*Corr. Author's Address: Henan University of Science and Technology, School of Mechatronics Engineering, Luoyang, China, litianxing@haust.edu.cn

can determine the virtual pair of contacting profiles, the backlash and the transmission errors.

Furthermore, the research on the meshing characteristics of ordinary gears laid the foundation for cycloidal-pin transmission. Hao et al. [9] established an analysis model to obtain the load-sharing characteristics of the aeronautical two-stage five-branching planets gear train. Tsai and Ye [10] proposed a computerized approach based on the influence coefficient method to solve the statically indeterminate problem of multiple loaded contact tooth pairs in planetary gear drives. Wang et al. [11] solved the meshing characteristic problem of orthogonal face-gear drives in real working conditions. Bodzas [12] carried out loaded tooth contact analysis of straight bevel gears and obtained the mechanical characteristics by different loads. Vivet et al. [13] proposed a multi-body meshing analysis method and analysed the transmission error and contact patterns of spiral bevel gears. Lin [14] presented the loaded contact analysis of curve-face gear pair. Nishino [15] developed a computerized tool to predict the loaded tooth contact pattern and static transmission error of hypoid gears. Kolivand and Kahraman [16] proposed a practical methodology based on ease-off topography for loaded tooth contact analysis of hypoid gears. Batsch [17] conducted tooth contact analysis on the convexo-concave helical bevel Novikov gear. Wang et al. [18] improved the transmission characteristics of equal base bevel gears from a processing perspective. Yang et al. [19] proposed a dynamic analysis method to improve the transmission performance of spiral bevel and hypoid gears. Changbin et al. [20] simulated the dynamic meshing process of the elliptic cylinder gear.

The load distribution and actual contact situation of the multi-tooth meshing of the cycloidal-pin gear are extremely complicated, and its load-bearing transmission process is a multi-body contact process. The key to loaded analysis is to accurately determine the actual number of meshing teeth and the nonlinear relationship between the contact force and deformation. In order to solve the static problems of elastic components, the principle of minimum energy is often used. It avoids the complex process of integral calculation directly using the relationship between force and deformation but gives a more concise result from the stability of energy. Li et al. [21] proposed a calculation method for cutting force based on an energy method. Based on the energy balance, Wang et al. [22] predicted the contribution of the axial force of the gear. Wang and Feng [23] derived the formula of time-varying mesh stiffness of the gear train based on the energy method. Liang et al. [24] evaluated the time-varying mesh stiffness of a planetary gear set by means of the potential energy method. Wan et al. [25] proposed an accumulated integral potential energy method to calculate the mesh stiffness of helical gears. Song et al. [26] proposed a potential energy-based slice grouping method to calculate the mesh stiffness of straight bevel gears. Wang et al. [27] studied the chaos and stability of spur gear based on the energy method and floquet theory. The above work provides a novel idea for the study of the complex meshing characteristics of cycloidal-pin gears.

In this paper, the nonlinear mathematical relationship between the meshing load and the deformation is established first. Next, the possible meshing teeth and their numbers are quickly estimated according to the distribution of the minimum meshing clearance and the maximum elastic deformation. More importantly, the principle of minimum energy is innovatively introduced into the loaded analysis process to accurately determine the actual number of teeth engaged simultaneously and their tooth numbers. Finally, according to the loaded analysis model of cycloid-pin gear, some important parameters of loaded characteristics are calculated and analysed.

1 TRANSMISSION CHARACTERISTICS OF CYCLOIDAL-PIN GEAR

The RV reducer is a closed differential gear system composed of a two-stage transmission mechanism, as shown in Fig. 1. The sun gear (driving gear) is connected to the input shaft. The planet gear meshed with the sun gear is fixedly connected with the crankshaft. Two cycloidal gears with the phase difference of 180° are installed on the crankshaft and engage with the pin gear fixed on the pin box. If the driving gear rotates counter-clockwise at a certain speed, the planetary gear meshing with the sun gear rotates clockwise, and the crankshaft fixed to the planetary gear rotates clockwise. The rotation of the crankshaft drives the cycloidal gear to revolve clockwise, and at the same time, the cycloidal gear rotates counter-clockwise under the action of the pin gear. The rotation of the cycloidal gear, in turn, causes the crankshaft to revolve counter-clockwise around the input shaft. The angular velocity of this revolution is the output angular velocity of the RV reducer, and its direction is the same as that of the input shaft. When the crankshaft rotates 360°, the cycloidal gear rotates by a pitch angle in the opposite direction. The rotation angular velocity of the cycloidal gear is equal to the revolution angular velocity of the crankshaft

connected to the output mechanism, so the angular velocity of the cycloidal gear can be transmitted and output by the output mechanism at a speed ratio of 1:1. It can be seen that the transmission performance of the cycloidal-pin mechanism directly connected to the output shaft has an important effect on the motion accuracy of the RV reducer.

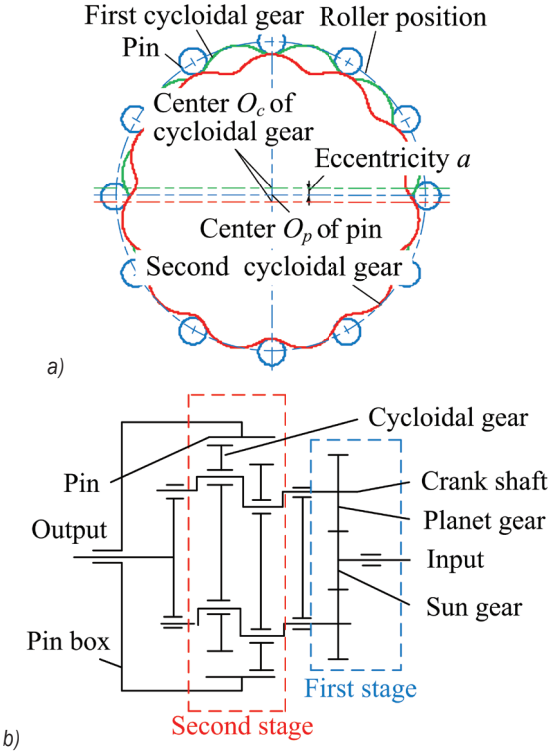

Fig. 1. *Transmission mechanism of RV reducer; a) cycloidal-pin gear; and b) transmission mechanism*

The simultaneous meshing of multiple teeth of the cycloidal-pin gear not only allows the load to be distributed to each tooth pair, which improves the carrying capacity, and its error equalization effect greatly improves the transmission accuracy. However, the load distribution and actual contact conditions of the multi-tooth meshing are quite complicated, and higher requirements are also placed on the machining errors and assembly processes [6]. In practical applications, many factors, such as machining errors, assembly errors, and modification errors, have significant and complex effects on the meshing contact state of gear teeth. In fact, according to the meshing principle of the gear, the interactive influence of various error factors indirectly changes the profile shape of the meshing tooth pair, which in turn affects the meshing contact state and transmission accuracy. In this case, the characteristics of simultaneous multi-tooth engagement no longer exist. Under no-load conditions, the smaller or larger cycloid gear and the pin gear only have a pair of teeth to maintain contact. There are initial clearances of different sizes between the other gear teeth. In the loaded state, only when the deformation of the first contact tooth is greater than the initial clearance, the remaining teeth can come into contact one after another. Therefore, the modification errors, machining errors, and thermal deformations have caused the change in the contact characteristics of cycloidal-pin gear, which inevitably produce transmission errors and lost motion. The change in the shape of the tooth profile leads to uneven load distribution, which will aggravate wear and reduce the accuracy retention of RV transmission.

2 MESHING MODEL OF CYCLOIDAL-PIN GEAR

Tooth contact analysis is one of the important means of studying meshing characteristics. The analysis method and model have been generated by some researchers [28] and [29]. In this section, the mathematical model of the cycloidal-pin transmission will be given for later use [6]. As shown in Fig. 2, $S_f(x_f,y_f)$ is a coordinate system fixedly connected to the frame. The coordinate systems of the pin gear and cycloidal gear are defined as $S_p(x_p,y_p)$ and $S_c(x_c,y_c)$, respectively. Their rotation angles are denoted as ϕ_1 and ϕ_2. The eccentricity is represented by a.

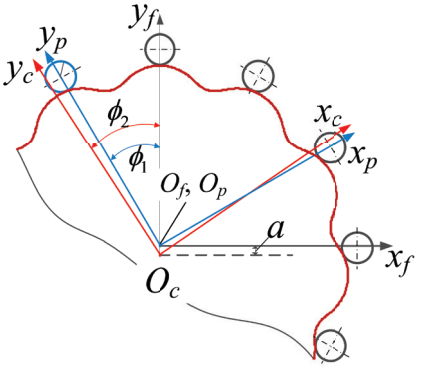

Fig. 2. *Meshing contact model of cycloidal-pin gear*

In the RV transmission process, the position vector and normal vector of the cycloidal gear and the pin gear at any meshing point should be consistent. Therefore, the meshing contact equation can be established [6]

$$\begin{cases} \mathbf{R}_c^{(f)}(\varphi,\phi_2) = \mathbf{R}_p^{(f)}(\beta,\phi_1) \\ \mathbf{n}_c^{(f)}(\varphi,\phi_2) = \mathbf{n}_p^{(f)}(\beta,\phi_1) \end{cases}, \tag{1}$$

where the superscript (f) is indicated in the coordinate system S_f. The vector $\mathbf{R}_c$ and $\mathbf{n}_c$ respectively represent the position and normal of the cycloidal gear, with φ and ϕ_2 as variables [1] and [6]. The vector $\mathbf{R}_p$ and $\mathbf{n}_p$ are the position and normal of the pin gear, with β and ϕ_1 as variables.

There are three nonlinear equations and four unknowns in Eq. (1). By giving different driving angle ϕ_1, a series of driven angles ϕ_2 and contact position parameters φ and β can be solved. The process of solving the meshing model is described as follows: first, an initial value of the driving angle ϕ_1 is given, which is denoted as $\phi_1^{(0)}$. In this case, Eq. (1) is a nonlinear equation system consisting of three equations and three unknowns. The driven angle $\phi_2^{(0)}$ and the initial contact position parameters $\beta^{(0)}$ and $\varphi^{(0)}$ can be solved by the optimization method. Then, by continuously changing ϕ_1 in small increments, a series of meshing contact parameters $\phi_1^{(k)}$, $\phi_2^{(k)}$, $\beta^{(k)}$ and $\varphi^{(k)}$ can be solved (superscript $k=1,2,...$ is the index of the meshing contact point). The nonlinear relationship between ϕ_1 and ϕ_2 determines the transmission error. The parameters φ and β determine the contact position on a tooth profile. Under no-load conditions, the transmission error is mainly determined by the actual clearance between the gear teeth. In the loaded state, the transmission error is mainly caused by the contact deformation and the meshing clearance, which is the main difference between the meshing characteristics analysis under unloaded and loaded conditions.

3 LOADED ANALYSIS BASED ON MINIMUM ENERGY PRINCIPLE

In theory, the deformation quantity at a meshing position should be the sum of the contact deformation and bending deformation. However, in order to increase the rigidity of the mechanism, a pillow-like pin-tooth structure is often used. Therefore, the bending deformation is ignored, and the contact deformation is mainly considered in this paper. Also, the error equalization effect of multi-tooth engagement makes the two symmetrically installed cycloidal gears have similar meshing characteristics, so only one cycloidal gear is considered.

3.1 Meshing Force at Contact Position

In the loaded transmission, the cycloidal gear bears the load torque. At the same time, due to its meshing contact with the pin gear, a torque opposite to the direction of the load torque is also imposed. According to the principle of torque balance, when the RV transmission runs stably, the algebraic sum of all torques should be zero. Therefore, the nonlinear relationship between the torque and the meshing force can be established.

$$T_c = \sum_{i=1}^{m} F_i(\varphi_i, \beta_i, \phi_{1i}, \phi_{2i}) \cdot L_i(\varphi_i), \tag{2}$$

where $i=1\sim m$, m is the number of simultaneous meshing teeth, and the meaning is the same below. The meshing force of the i^{th} tooth is represented by F_i, which is related to parameters ϕ_1, ϕ_2, φ and β. The distance L_i is the force arm at the contact point of the i^{th} tooth, with φ as the variable.

By solving Eq. (1), the contact position parameters φ and β of the cycloidal gear and the pin gear can be determined. Assuming that the number of meshing teeth m is determined, the force arm L_i can be calculated. According to Eq. (2), the meshing force of the contact position can be obtained.

3.2 Meshing Contact Deformation and Coordination Relationship

According to the Hertz contact theory, the elastic contact problem of the cycloidal-pin gear at the meshing position is simplified in this paper [30]. The contact is considered as the smooth contact of the elastic body without friction. The vertical pressure on the contact surface is considered to be uniformly distributed, and the contact area is a small deformation. Thus, the meshing contact of the cycloidal-pin gear can be simplified into an elastic contact between two parallel cylinders, as shown in Fig. 3.

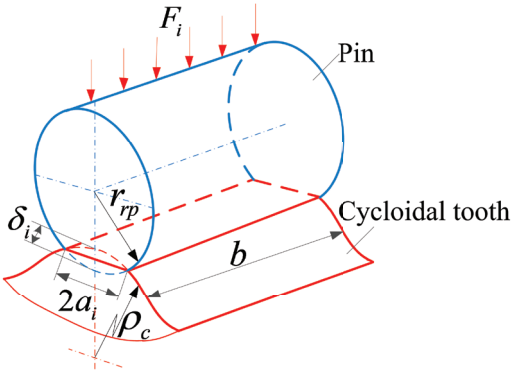

Fig. 3. *Contact deformation model of cycloidal-pin gear*

Under no-load conditions, the contact pattern of the cycloidal-pin gear should be a straight line. After loading, the contact pattern will become rectangular. The contact half-width a_i can be expressed as:

$$a_i(\varphi_i,\beta_i,\phi_{1i},\phi_{2i}) = \sqrt{\frac{4\cdot F_i(\varphi_i,\beta_i,\phi_{1i},\phi_{2i})\cdot\rho_i(\varphi_i)}{\pi\cdot b}\left(\frac{1-\mu_c^2}{E_c}+\frac{1-\mu_p^2}{E_p}\right)}, \quad (3)$$

where b is the width of the cycloidal gear. Young's modulus of the cycloidal gear and the pin gear are denoted as E_c and E_p, respectively. Their Poisson ratio are μ_c and μ_p. The comprehensive curvature radius, ρ_i, at the meshing point, which can be determined by the radius of curvature of the cycloidal gear and the pin gear.

$$\rho_i(\varphi)=\frac{1}{\frac{1}{\rho_{ci}(\varphi)}\pm\frac{1}{r_{rp}}}=\frac{\rho_{ci}(\varphi)\cdot r_{rp}}{\rho_{ci}(\varphi)\pm r_{rp}}, \quad (4)$$

where the positive sign is used for external contact and the negative sign is used for internal contact. The roller radius, which is represented by r_{rp}, is the radius of curvature of the pin gear. The radius of curvature at the contact point of the cycloidal gear is denoted as ρ_{ci}, which can be calculated as follows:

$$\rho_{ci}(\varphi)=\left|\frac{(r_p+\Delta r_p)\cdot(1+k_1^2-2k_1\cdot\cos(z_c\cdot\varphi))^{3/2}}{k_1\cdot(z_p+1)\cdot\cos(z_c\cdot\varphi)-(1+z_p\cdot k_1^2)}+r_{rp}+\Delta r_{rp}\right|, \quad (5)$$

where z_c and z_p is the number of teeth of cycloidal gear and pins; k_1 is the short width coefficient; r_p is the roller position; Δr_p and Δr_{rp} is the modification by the radius and position of the roller.

According to the geometric relationship in Fig. 3, the deformation δ_{ci} and δ_{pi} of the cycloidal-pin gear at the i^{th} contact position can be calculated as follows

$$\delta_{ci}=\rho_{ci}-\sqrt{\rho_{ci}^2-a_i^2}, \quad (6)$$

$$\delta_{pi}=r_{rp}-\sqrt{r_{rp}^2-a_i^2}. \quad (7)$$

The normal stiffness K_{ci} and K_{pi} at the i^{th} contact position of the cycloidal gear and the pin gear can be determined respectively:

$$K_{ci}=\frac{F_i}{\delta_{ci}}, \quad (8)$$

$$K_{pi}=\frac{F_i}{\delta_{pi}}. \quad (9)$$

From this, the normal meshing stiffness K_{ni} of a pair of teeth of the cycloid-pin gear can be obtained:

$$K_{ni}=\frac{K_{ci}K_{pi}}{K_{ci}+K_{pi}}. \quad (10)$$

The equivalent torsional stiffness K_{ti} of the cycloidal-pin gear at the i^{th} contact position can be expressed as follows:

$$K_{ti}=K_{ni}\cdot L_i^2. \quad (11)$$

Therefore, the nonlinear relationship between the meshing force F_i and the deformation δ_i can be determined as follows:

$$\delta_i(\varphi_i,\beta_i,\phi_{1i},\phi_{2i})=\frac{F_i}{K_{ti}}. \quad (12)$$

Additionally, the contact deformation of the cycloidal gear and the pin gear is not independent. A certain coordination relationship should be met, which ensures the integrity and continuity after contact deformation. In the paper, the ratio of the sum of δ_i and d_i to L_i is defined as the error rotation angle. According to the coordination relationship, the angles should be equal at all contact positions. Thus, the deformation coordination equation can be obtained

$$\frac{\delta_1+d_1}{L_1}=\frac{\delta_2+d_2}{L_2}=\cdots=\frac{\delta_i+d_i}{L_i}=\cdots=\frac{\delta_m+d_m}{L_m}. \quad (13)$$

3.3 Determination of Possible Number of Meshing Teeth

Under no-load conditions, only one pin tooth maintains meshing contact with the cycloidal tooth, and there are initial clearances of different sizes between the other teeth. According to Eq. (1), the distribution of the minimum meshing clearance of the cycloidal-pin gear can be obtained [6], as shown in Fig. 4.

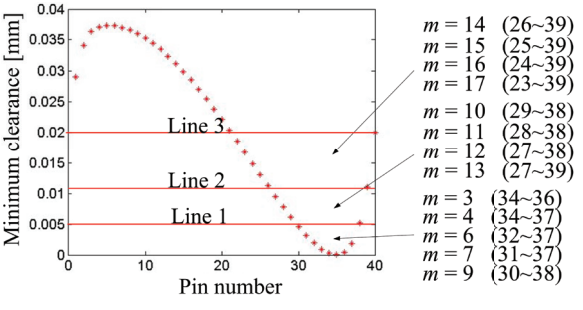

Fig. 4. *Minimum meshing clearance and maximum deformation*

It can be seen from the distribution of the minimum clearance shown in Fig. 4 that the clearance between the 35th pin tooth and the cycloidal profile is

zero. Therefore, the 35th pin should be the first tooth in contact under no-load condition. After loading, the 35th pin tooth produces a certain deformation displacement under the action of the meshing force. When the next pin comes into contact, the deformation quantity reaches the maximum value. Only when the deformation value is greater than the meshing clearance of other pin teeth can they come into contact with the cycloidal tooth. Lines 1, 2, and 3 in Fig. 4 illustrate the position of the maximum deformation with respect to the clearance distribution. If the maximum deformation is at the position of line 1, the No. 30~38 pin teeth bellow line 1 will be most likely to contact after load. In this case, the maximum number of meshing teeth can be estimated to be 9.

It should be noted that the estimated number of meshing teeth and their tooth numbers are only the maximum possible value. Each possibility needs to be grouped to discuss the actual number of meshing teeth. The detailed process of estimating the number of teeth that may be meshed and their tooth numbers is shown in Fig. 5.

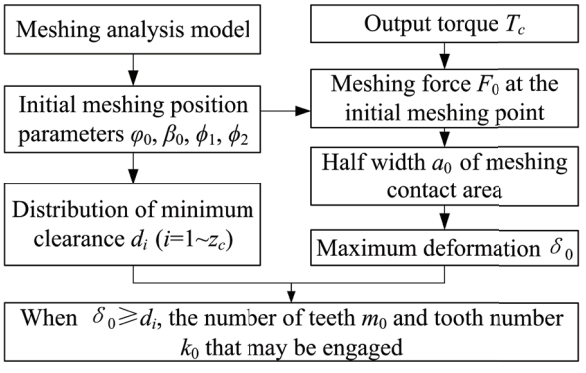

Fig. 5. *Flowchart of determination of the possible number of meshing teeth*

3.4 Actual Number of Meshing Teeth Based on Minimum Energy Principle

Energy is conserved. In order to maintain the balance of the system, the energy will automatically decrease until the whole system reaches a state of dynamic balance. The state at the minimum energy is relatively stable. The RV cycloidal-pin transmission should also conform to this energy conversion process.

The total energy of the cycloidal-pin transmission system in the stable state should be the minimum. Therefore, the principle of minimum energy can be used to accurately determine the actual number of meshing teeth of the cycloidal-pin gear. The total energy *NE* of the cycloidal-pin gear is the sum of the product of the meshing force F_i and the deformation δ_i, which can be expressed as follows:

$$NE(\varphi_i, \beta_i, \phi_{1i}, \phi_{2i}) = \sum_{i=1}^{m} F_i(\varphi_i, \beta_i, \phi_{1i}, \phi_{2i}) \cdot \delta_i(\varphi_i, \beta_i, \phi_{1i}, \phi_{2i}), \quad (14)$$

The specific method is to first group the possible meshing tooth pairs of the cycloidal-pin gear under the loaded state, and then calculate and compare the total energy of each group separately. The number of meshing teeth with the minimum total energy is the actual number of meshing teeth. The actual meshing state of the cycloidal-pin gear can be determined based on the number of teeth engaged simultaneously and their tooth numbers. The determination process is shown in Fig. 6.

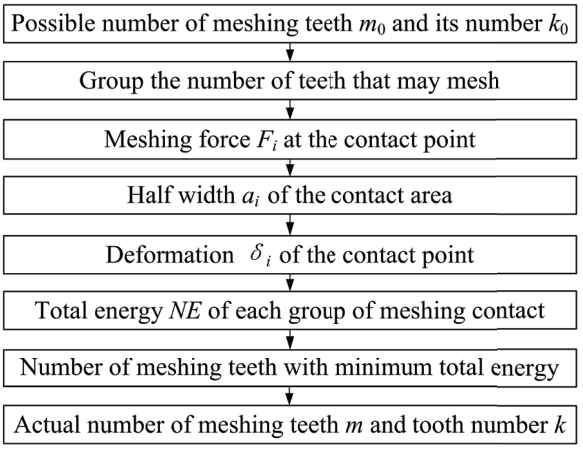

Fig. 6. *Flowchart of determination of the actual number of meshing teeth*

3.5 Loaded Analysis Strategy

According to the loaded analysis model and calculation method of meshing parameters, the loaded analysis process of the cycloidal-pin gear is planned, as shown in Fig. 7. The specific implementation process is as follows:

1. According to the unloaded contact analysis method, the initial meshing position of the cycloidal-pin gear is solved. On this basis, the distribution of the minimum meshing clearance of the RV transmission is determined.
2. According to the loaded analysis model, the maximum deformation at the initial meshing position is determined.
3. By comparing the minimum meshing clearance and the maximum deformation, the possible number of meshing teeth and the tooth numbers

are estimated, and the reasonable grouping is performed.

4. Based on the loaded analysis model, the meshing force and deformation at the meshing contact point of each group are calculated in sequence, and then the total energy of deformation of each group is obtained.
5. By comparing the total energy of each group, the meshing force, deformation, the number of simultaneous meshing teeth and the tooth numbers, as well as the meshing position parameters, are determined at the minimum energy. These data reflect the actual loaded meshing state.
6. Continuously changing the rotation angle of driving gear and the contact position, the instantaneous meshing parameters of the corresponding meshing point can be calculated in sequence until it is disengaged.
7. According to the meshing position parameters, the loaded contact patterns can be determined. According to the relationship between the theoretical and actual output angle, the loaded transmission error curve can be drawn.

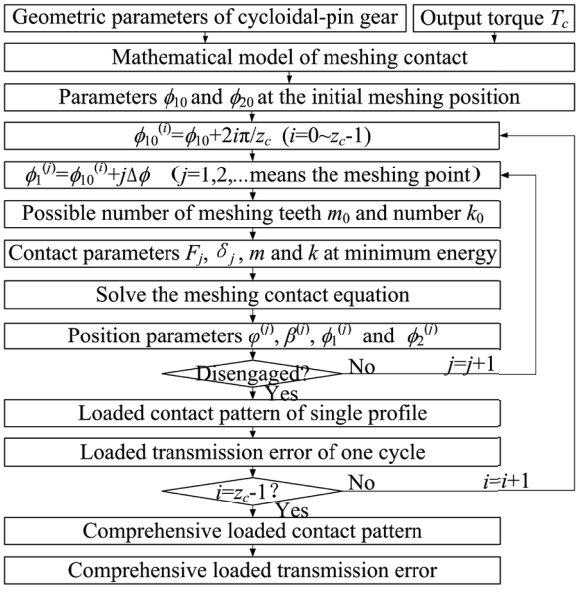

Fig. 7. *Flowchart of loaded analysis*

4 RESULTS OF LOADED ANALYSIS

Taking the cycloidal-pin gear of a robot reducer as an example, the loaded meshing performance is analysed according to the proposed strategy. The cycloidal gear and the pin gear are made of GCr15 bearing steel with the Poisson ratio of 0.3 and Young's modulus of 2.08×10^5 MPa. The geometric parameters of the cycloidal-pin gear are shown in Table 1.

In the experiment, 10 % of the rated torque, T_c = 57 N·m, was applied to the cycloidal-pin gear. According to the loaded analysis model, the meshing force and deformation energy of the cycloidal-pin gear were solved. The actual number of meshing teeth is m = 16 and the tooth number k is No. 24 ~ 39. According to the planned strategy of loaded analysis, the deformation, meshing stress, contact patterns and loaded transmission errors at each meshing point were obtained.

Table 1. *Geometric parameters of cycloidal-pin gear*

Parameters	Values
Number of teeth of sun gear	12
Number of teeth of planet gear	48
Pressure angle [deg]	20
Number of pins	40
Number of teeth of cycloid gear	39
Roller position [mm]	52.15
Roller radius [mm]	2
Eccentricity [mm]	0.9
Width of cycloidal gear [mm]	10
Width of pin gear [mm]	22
Modification by roller radius [mm]	0.01
Modification by roller position [mm]	–0.012

4.1 Loaded Contact Force and Contact Pressure

Fig. 8 shows the contact force and its distribution at each meshing point when the rotation angle of the pin gear is 0.02 rad, 0.04 rad, 0.06 rad, and 0.08 rad respectively.

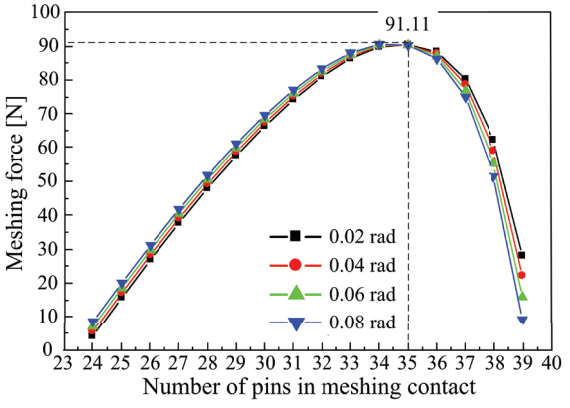

Fig. 8. *Contact force distribution at meshing points*

It can be seen from Fig. 8 that the force distribution of the meshing positions at different

rotation angles of the cycloidal-pin gear is essentially the same. As the number of pins in meshing contact gradually increases, the contact force first increases to the peak and then decreases. The maximum contact force is 91.11 N at the 35th pin. If the pin gear rotates counter-clockwise, as the rotation angle of the pin gear increases, the contact force before the peak increases, and the contact force after the peak decreases. According to the distribution of the contact force, with the rotation of the pin gear, the contact force of the 39th pin will gradually decrease until it reaches 0, at which time this pair of gear teeth are disengaged. At the same time, the 23rd pin teeth come into contact in sequence, and the contact force increases until it reaches the peak and then gradually decreases until disengaged.

According to the contact force and contact area at each meshing position, the contact pressure was also calculated, as shown in Fig. 9.

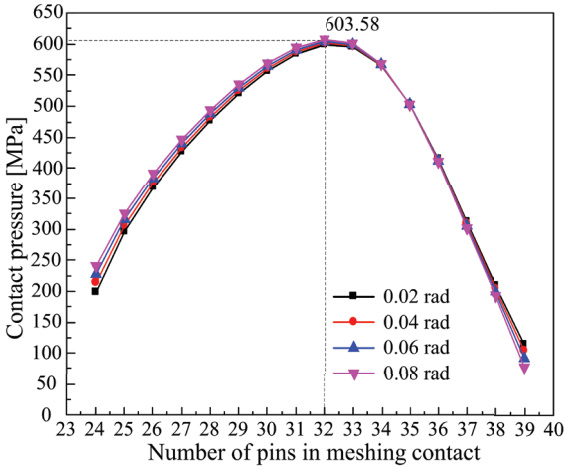

Fig. 9. *Contact pressure at meshing points*

It can be seen that the contact pressure at each meshing position increases to the peak first and then decreases with the increase of the number of pins. The maximum pressure is at the 32nd pin tooth, and its value is 603.58 MPa. Compared with the distribution of the contact force in Fig. 8, the peak position of the maximum contact pressure is different. The pressure value is related not only to the contact force F_i, but also to the comprehensive curvature radius ρ_i. If the contact force is larger, the corresponding comprehensive radius of curvature is also larger, but the contact pressure is not necessarily larger. Therefore, the influence of the curvature radius on contact pressure is more obvious.

4.2 Loaded Deformation

Fig. 10 shows the deformation distribution at each meshing point when the rotation angle of the pin gear is different.

It can be seen from Fig. 10 that the loaded deformation at the meshing position of the cycloidal-pin gear is essentially consistent with the contact force. With the increase of the pin number, the deformation value at each meshing point first increases to the peak and then decreases. The maximum deformation is 0.057 mm at the 35th pin. If the pin gear rotates counter-clockwise, the deformation before the peak increases, and the deformation after the peak decreases with the increase of the angle of the pin gear. According to the deformation distribution trend, with the rotation of the pin gear, the deformation of the 39th pin gradually decreases until it becomes zero, at which time the pair of pin teeth are disengaged. At the same time, the 23rd pin tooth is in meshing contact immediately, and its deformation quantity increases until it reaches the peak and then gradually decreases until disengaged.

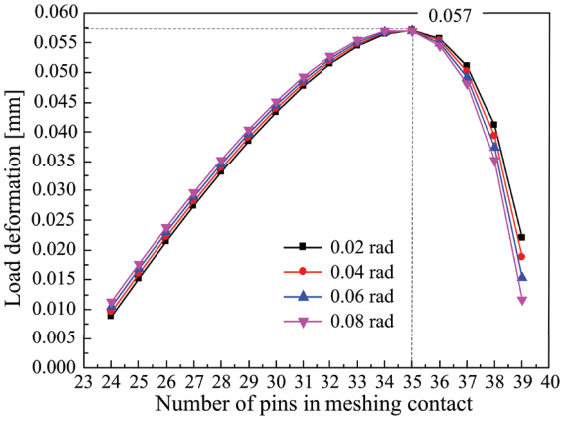

Fig. 10. *Deformation distribution at each meshing point*

According to Eq. (12), the deformation δ_i is influenced by the contact force F_i and the curvature radius ρ_i. The changes in the meshing force and deformation shown in Figs. 8 and 10 are similar. It can be concluded that the curvature radius ρ_i has little effect on the loaded deformation.

4.3 Loaded Contact Pattern

At the initial meshing position of the cycloidal-pin gear, the contact parameter φ_i and the half-width a_i were calculated, as shown in Table 2.

Table 2. *Position parameters and contact half-width*

Parameters	Number of simultaneous meshing teeth								
Pin number	24	25	26	27	…	36	37	38	39
Position [rad]	-2.51	-2.36	-2.2	-2.04	…	-0.63	-0.47	-0.31	-0.16
Half-width [mm]	0.15	0.19	0.24	0.27	…	0.44	0.37	0.34	0.24

In order to more clearly compare the positions of the contact patterns when multiple teeth are in contact, all positions are displayed on the same tooth surface, as shown in Fig. 11. It can be seen that the loaded contact pattern of the cycloidal-pin gear is approximately rectangular. From the 24th to 39th teeth, the contact patterns at each meshing position are gradually widened from 0.15 mm to 0.47 mm, and then gradually reduced to 0.24 mm. The change rule of the loaded contact pattern is essentially the same as that of the meshing force and contact pressure, that is, the greater the loaded contact force and the contact pressure is, the larger the area of the contact pattern is.

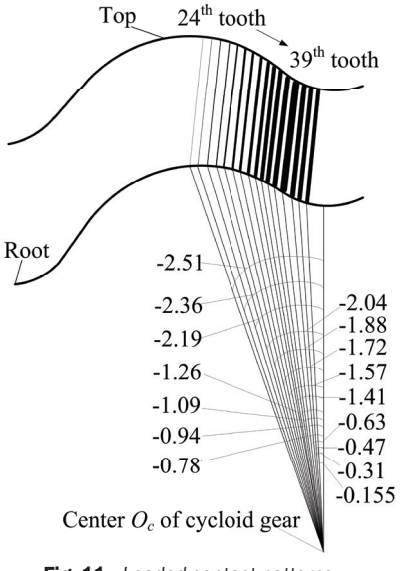

Fig. 11. *Loaded contact patterns*

4.4 Loaded Transmission Error

Using the loaded analysis model, continuously changing the rotation angle ϕ_1 of the pin gear, the actual rotation angles of the cycloidal gear can be obtained. Then the loaded transmission error curve was drawn, as shown in Fig. 12.

It can be seen from Fig. 12 that the loaded transmission error of the cycloidal-pin gear changes periodically and is smooth. In one cycle, as the rotation angle of the pin gear increases, the transmission error gradually decreases to -3.80 arcmin and then slowly increases to -7.46 arcmin until the next cycle begins. The amplitude of the fluctuation is approximately 3.66 arcmin. Since the assembly error and machining error are not considered, the transmission error in the theoretical model mainly depends on the contact deformation, torsional deformation and meshing clearance. Therefore, the fluctuation amplitude of each meshing cycle is consistent and relatively small.

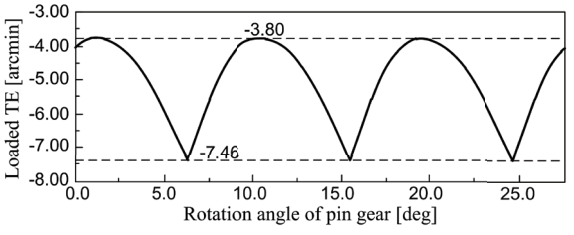

Fig. 12. *Loaded transmission error curve (Three cycles)*

It should be mentioned that the design purpose of the holes in the blank of the cycloid is mainly to reduce the weight. The prerequisite for lightweight design is that the meshing performance of the gear train cannot be changed. Therefore, the effect of the stiffness of holes in the blank on the contact pressure and transmission error can be ignored, which was proved in the comparison and analysis of ABAQUS results.

5 EXAMPLES AND DISCUSSION

The parametric modelling of the RV reducer was completed through Unigraphics (UG) software. Due to the pillow-like structure of the pin gear and the symmetrical distribution of the cycloidal gear in the robot reducer, the model is simplified to the meshing contact form of a cycloidal gear and a pin gear. The simplified model was imported into ABAQUS for finite element analysis.

In order to better compare the examples, two ABAQUS models have been established, as shown in Fig. 13. Model A in Fig. 13a is the "full blank". Model B in Fig. 13b is the "blank with holes".

The finite element mesh has a significant impact on the analysis results. The meshing contact

deformation of the cycloidal-pin gear is mainly located near the contact area. Therefore, a method of mesh refinement near the contact area was adopted. The approximate size of the elements of the refined mesh is 0.2 mm. The element type is C3D8R (8-node linear brick). The total number of meshes of the cycloidal gear (without holes) and the pin gear are 203,973 and 183,792, respectively. Also, the gear axes (Z-axis) of the cycloid and pin gears were free, and other degrees of freedom were restricted. The bending moment imposed on a cycloidal gear was set to 28.5 Nm, which is half of the actual load. The contact property was defined as frictionless and "hard" contact. The pin surface was assigned as the master surface and the cycloidal surface as the slave surface.

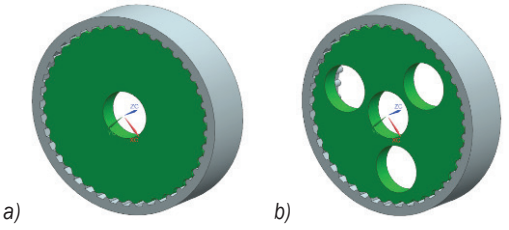

a) b)

Fig. 13. *ABAQUS model; a) model A; and b) model B*

5.1 Comparison and Analysis of Contact Pressure

The contact pressure distributions of the finite element simulation of the cycloidal gear and the pin gear are shown in Figs. 14 and 15, respectively. It can be seen from Fig. 14 that the maximum contact pressures of the cycloidal gear are 601.3 MPa and 600.0 MPa, respectively. The difference between the two is within 0.22 %, which shows that the stiffness of the hole in the blank has almost no effect on the contact pressure. For the pin gear in Fig. 15, the conclusions are similar.

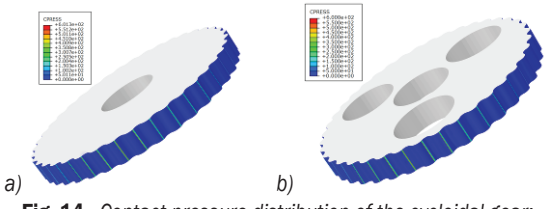

a) b)

Fig. 14. *Contact pressure distribution of the cycloidal gear; a) Model A; and b) Model B*

In order to verify the correctness of the theoretical model, the contact pressure distribution of the Model B simulation and the theoretical calculation was compared in Fig. 16. It can be seen that their trends are similar, and the maximum pressure is at the 32nd pin. The difference between the two is within 0.6 %, which shows the correctness of the theoretical model and the results.

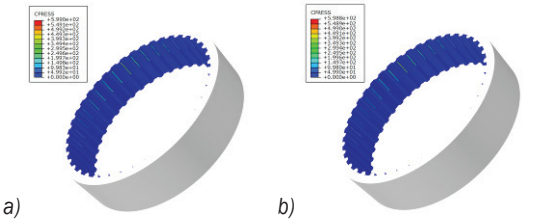

a) b)

Fig. 15. *Contact stress distribution of the pin gear; a) Model A; and b) Model B*

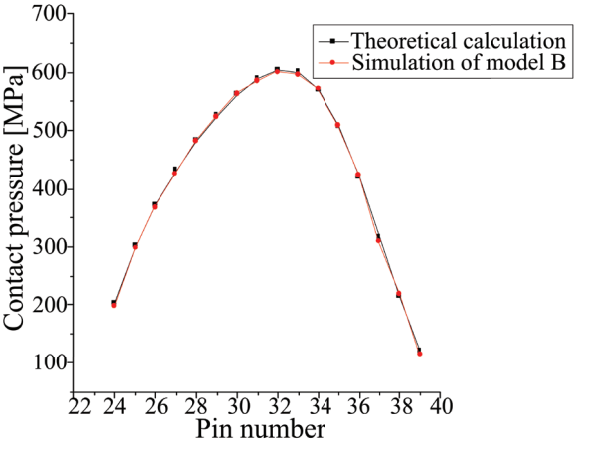

Fig. 16. *Comparison of contact pressure between simulation and theoretical calculation*

5.2 Comparison and Analysis of Contact Pattern

According to the contact stress of the finite element analysis, the actual number of meshing teeth and the tooth numbers were determined, and the meshing patterns of the cycloidal-pin gear was obtained, as shown in Fig. 17.

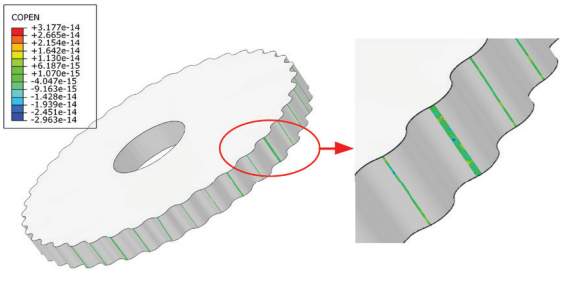

Fig. 17. *Contact patterns of simulation*

From the simulation results, it was found that the contact patterns of Models A and B were the same, which shows that the stiffness of the holes in the cycloidal gear has a very small effect on the contact

patterns. Only the results of Model A were drawn in Fig. 17. It can be seen from the comparison with Fig. 11 that the actual number of meshing teeth is also 16. The size of the meshing area is slightly different from the theoretical one, which is due to the influence of the mesh fineness in the simulation model and the rotation angle error of the theoretical model on the comparison results.

5.3 Measurement of Loaded Transmission Error

In order to better compare and analyse the results of the theoretical model and the ABAQUS model, the loaded transmission errors of Models A and B in ABAQUS were respectively extracted, as shown in Fig. 18.

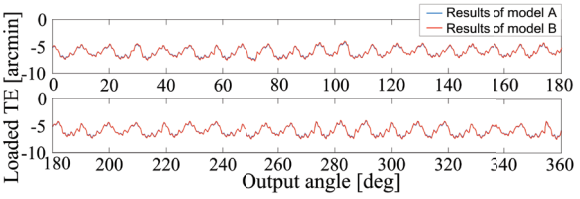

Fig. 18. *Loaded transmission errors of Models A and B*

In Fig. 18, the fluctuation amplitudes of loaded transmission errors of models A and B are 3.69 arcmin and 3.7 arcmin, respectively. The difference in simulation results is 0.01 arcmin. Therefore, the influence of the stiffness of the holes in Model B on the loaded transmission error can be ignored. The simulation results of Models A and B are the same. In addition, compared with the theoretical results in Fig. 12, the difference between Model B and the theoretical model is within 1.1 %, which indicates the correctness of the theoretical model.

Furthermore, a measurement experiment of the loaded transmission error was completed on a RV reducer comprehensive performance tester, as shown in Fig. 19. The assembled reducer and its cycloidal gear with holes are shown in Fig. 20. During the measurement process, the RV reducer is mounted on a precision bracket. The input is driven by the input motor. The output end is connected to the output assembly through a coupling, and is loaded through a load motor and a torque sensor. Through the high-precision circular grating installed at the input and output ends, the angle changes of the input and output are collected in real time to realize the transmission error measurement. The measurement accuracy of the tester is within 8.0 arcsec, which can meet the experiment requirements.

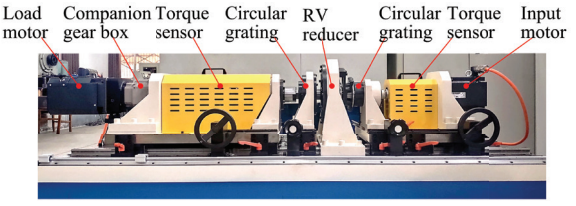

Fig. 19. *RV reducer comprehensive performance tester*

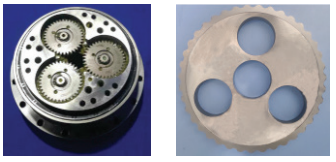

Fig. 20. *a) RV reducer and b) cycloidal gear*

In the 360° range of the output shaft, 1800 angles of the output shaft were collected. By calculating the difference between the theoretical and actual output angle, the loaded transmission error curve was drawn, as shown in Fig. 21.

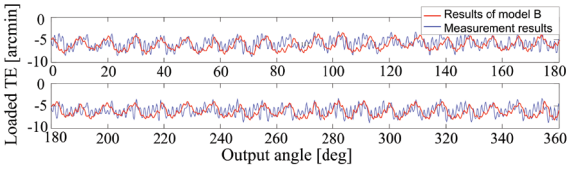

Fig. 21. *Loaded transmission errors of measurement*

It can be seen from Figs. 12 and 21 that the transmission error curves of theoretical calculation, actual measurement and simulation analysis all show a relatively consistent parabolic trend. In Fig. 21, the actual measured transmission error is larger than those of the numerical model and experimental results. Their maximum fluctuation amplitudes are 3.83 arcmin, 3.66 arcmin and 3.7 arcmin, respectively. The maximum difference is about 4.4 %. From the comparison of data and trends, it can be concluded that the transmission error of the numerical model, the finite element model and the experimental results have good consistency. The effectiveness and practicability of the proposed method and simulation analysis can also be validated.

However, further improvement of the experimental results is an important topic for future work. The second-stage mechanism in the RV reducer has a certain influence on the experimental results. In addition, there are many influencing factors in the actual measurement process, such as assembly errors, profile errors and pitch errors of cycloidal gears, processing errors of other key components, bearing clearance, etc. The comprehensive influence of these

factors is very complex and cannot be accurately determined **[31]** to **[33]**.

6 CONCLUSIONS

This paper presents the loaded analysis method based on the minimum energy principle for RV cycloidal-pin transmission. The main conclusions include:

1. The Hertz contact theory, the principle of minimum energy and the finite element method were integrated into the loaded contact analysis of the cycloidal-pin drive, and the actual loaded characteristics were obtained.
2. The possible meshing teeth and their numbers were quickly estimated according to the distribution of the minimum meshing clearance and the maximum deformation of the cycloidal-pin gear.
3. By comparing the minimum energy of the contact tooth pair, the actual number of teeth engaged simultaneously was accurately determined, which is critical to the accuracy of the loaded analysis.
4. The comparison and verification of theoretical modelling, finite element analysis and measurement experiment show that the difference in contact pressure, the number of meshing teeth, contact pattern and transmission errors were essentially the same, which proves the effectiveness and correctness of the proposed method.

This study solves the bottleneck problem in which the actual meshing performance is inconsistent with the theoretical analysis results in the loaded transmission of RV reducer, and has an important reference value for the improvement and pre-control of the kinematic accuracy of the robot RV Reducer. However, for the proposed method, some work remains to be done, including the comprehensive transmission characteristics of RV reducer in the theoretical model, the influence law of load torque on transmission error and the number of meshing teeth, and experimental research more in line with the actual working conditions.

7 ACKNOWLEDGEMENTS

This work supported by National Natural Science Foundation of China (No. U1504522, 51705134, and 51675161), Key Scientific Research Projects of Higher Education Institutions in Henan Province of China (No. 20A460010) and Key Scientific and Technological Project in the Henan Province of China (No. 202102210079).

8 REFERENCES

[1] Lin, W.S., Shih, Y.P., Lee, J.J. (2014). Design of a two-stage cycloidal gear reducer with tooth modifications. *Mechanism and Machine Theory*, vol. 79, p. 184-197, **DOI:10.1016/j.mechmachtheory.2014.04.009**.

[2] Li, T.X., Zhou, J.X., Deng, X.Z., Li, J.B., Xing, C.R., Su, J.X., Wang, H.L. (2018). A manufacturing error measurement methodology for a rotary vector reducer cycloidal gear based on a gear measuring center. *Measurement Science and Technology*, vol. 29, art. ID 075006, **DOI:10.1088/1361-6501/aac00a**.

[3] Xu, L.X., Yang, Y.H. (2016). Dynamic modeling and contact analysis of a cycloid-pin gear mechanism with a turning arm cylindrical roller bearing. *Mechanism and Machine Theory*, vol. 104, p. 327–349, **DOI:10.1016/j.mechmachtheory.2016.06.018**.

[4] Li, T.X., Li, J.B., Deng, X.Z., Yang, J.J., Li, G.G., Ma, W.S. (2017). A new digitized reverse correction method for hypoid gears based on a one-dimensional probe. *Measurement Science and Technology*, vol. 28, no. 12, art. ID 125004, **DOI:10.1088/1361-6501/aa8dd7**.

[5] Li, X., Li, C.Y., Wang, Y.W., Chen, B.K., Lim, T.C. (2017). Analysis of a cycloid speed reducer considering tooth profile modification and clearance-fit output mechanism. *Journal of Mechanical Design*, vol. 139, no. 3, art. ID 033303, **DOI:10.1115/1.4035541**.

[6] Li, T.X., Tian, M., Xu, H., Deng, X.Z., An, X.T., Su, J.X. (2020). Meshing contact analysis of cycloidal-pin gear in RV reducer considering the influence of manufacturing error. *Journal of the Brazilian Society of Mechanical Sciences and Engineering*, vol. 42, art. ID 133, **DOI:10.1007/s40430-020-2208-7**.

[7] Huang, C.H., Tsai, S.J. (2017). A study on loaded tooth contact analysis of a cycloid planetary gear reducer considering friction and bearing roller stiffness. *Journal of Advanced Mechanical Design, Systems, and Manufacturing*, vol. 11, no. 6, p. 17-00213, **DOI:10.1299/jamdsm.2017jamdsm0077**.

[8] Demenego, A., Vecchiato, D., Litvin, F.L., Nervegna, N., Manco, S. (2002). Design and simulation of meshing of a cycloidal pump. *Mechanism and Machine Theory*, vol. 37, no. 3, p. 311-332, **DOI:10.1016/S0094-114X(01)00074-X**.

[9] Hao, D., Fang, Z.D., Hu, Y.H. (2018). Study on the load-sharing characteristics of an aeronautical ii-stage five-branching planets gear train based on the loaded tooth contact analysis. *Mathematical Problems in Engineering*, vol. 2018, art. ID. 5368294, **DOI:10.1155/2018/5368294**.

[10] Tsai, S.J., Ye, S.Y. (2018). A computerized approach for loaded tooth contact analysis of planetary gear drives considering relevant deformations. *Mechanism and Machine Theory*, vol. 122, p. 252-278, **DOI:10.1016/j.mechmachtheory.2017.12.026**.

[11] Wang, Y.Z., Wu, C.H., Gong, K., Wang, S., Zhao, X.F., Lv, Q.J. (2012). Loaded tooth contact analysis of orthogonal face-gear drives. *Proceedings of the Institution of Mechanical Engineers, Part C: Journal of Mechanical Engineering Science*, vol. 226, no. 9, p. 2309-2319, **DOI:10.1177/0954406211432976**.

[12] Bodzás, S. (2020). Computer-aided design and loaded tooth contact analyses of bevel gear pair having straight teeth by

different loaded torques. *Mechanics and Industry*, vol. 21, no. 1, art. ID 109, **DOI:10.1051/meca/2019076**.

[13] Vivet, M., Mundo, D., Tamarozzi, T., Desmet, W. (2018). An analytical model for accurate and numerically efficient tooth contact analysis under load, applied to face-milled spiral bevel gears. *Mechanism and Machine Theory*, vol. 130, p. 137-156, **DOI:10.1016/j.mechmachtheory.2018.08.016**.

[14] Lin, C., He, C.J., Gu, S.J., Wu, X.Y. (2017). Loaded tooth contact analysis of curve-face gear pair. *Advances in Mechanical Engineering*, vol. 9, no. 10, art. ID 1687814017727473, **DOI:10.1177/1687814017727473**.

[15] Nishino, T. (2009). Computerized modeling and loaded tooth contact analysis of hypoid gears manufactured by face hobbing process. *Journal of Advanced Mechanical Design, Systems, and Manufacturing*, vol. 3, no. 3, p. 224-235, **DOI:10.1299/jamdsm.3.224**.

[16] Kolivand, M., Kahraman, A. (2010). An ease-off based method for loaded tooth contact analysis of hypoid gears having local and global surface deviations. *Journal of Mechanical Design*, vol. 132, no. 7, art. ID 071004, **DOI:10.1115/1.4001722**.

[17] Batsch, M. (2020). Mathematical model and tooth contact analysis of convexo-concave helical bevel Novikov gear mesh. *Mechanism and Machine Theory*, vol. 149, art. ID 103842, **DOI:10.1016/j.mechmachtheory.2020.103842**.

[18] Wang, B., Sun, X., Feng, P.Y., Yan, C.X., Jia, X.J. (2019). Solution and verification of cutter position for machining split equal-base circle bevel gear. *Mathematical Problems in Engineering*, vol. 2019, art. ID 8024701, **DOI:10.1155/2019/8024701**.

[19] Yang, J.J., Shi, Z.H., Zhang, H., Li, T.X., Nie, S.W., Wei, B.Y. (2018). Dynamic analysis of spiral bevel and hypoid gears with high order transmission errors. *Journal of Sound and Vibration*, vol. 417, p. 149–164, **DOI:10.1016/j.jsv.2017.12.022**.

[20] Changbin, D., Yongping, L., Yongqiao, W. (2020). Dynamic meshing characteristics of elliptic cylinder gear based on tooth contact analysis. *International Journal of Engineering*, vol. 33, no. 4, p. 676-685, **DOI:10.5829/IJE.2020.33.04A.19**.

[21] Li, J., Wang, P., Jin, Y. Q., Hu, Q., Chen, X.C. (2016). Cutting force calculation for gear slicing with energy method. *International Journal of Advanced Manufacturing Technology*, vol. 83, p. 887-896, **DOI:10.1007/s00170-015-7630-0**.

[22] Wang, Y.R., Ye, H., Jiang, X.H., Tian, A.M. (2018). On the existence of self-excited vibration in thin spur gears: A theoretical model for the estimation of damping by the energy method. *Symmetry*, vol. 10, no. 12, art. ID 664, **DOI:10.3390/sym10120664**.

[23] Wang, J., Feng, F.Z. (2020). Calculation and simulation of time-varying mesh stiffness of involute gear based on energy method. *World Scientific Research Journal*, vol. 6, no. 1, p. 181-190, **DOI:10.6911/WSRJ.202001_6(1).0026**.

[24] Liang, X.H., Zuo, M.J., Patel, T.H. (2014). Evaluating the time-varying mesh stiffness of a planetary gear set using the potential energy method. *Proceedings of the Institution of Mechanical Engineers, Part C: Journal of Mechanical Engineering Science*, vol. 228, no. 3, p. 535-547, **DOI:10.1177/0954406213486734**.

[25] Wan, Z.G., Cao, H.R., Zi, Y.Y., He, W.P., Chen, Y.M. (2015). Mesh stiffness calculation using an accumulated integral potential energy method and dynamic analysis of helical gears. *Mechanism and Machine Theory*, vol. 92, p. 447-463, **DOI:10.1016/j.mechmachtheory.2015.06.011**.

[26] Song, C.S., Zhou, S.W., Zhu, C.C., Yang, X.Y., Li, Z.F., Sun, R.H. (2018). Modeling and analysis of mesh stiffness for straight beveloid gear with parallel axes based on potential energy method. *Journal of Advanced Mechanical Design, Systems, and Manufacturing*, vol. 12, no. 7, art art. ID JAMDSM0122, **DOI:10.1299/jamdsm.2018jamdsm0122**.

[27] Wang, J.G., Lv, B., Zhao, Y.X. (2018). Chaos and stability of spur gear transmission system for locomotive based on energy method and floquet theory. *Shock and Vibration*, vol. 2018, art. ID 5691892, **DOI:10.1155/2018/5691892**.

[28] Li, T.X., An, X.T., Deng, X.Z., Li, J.F., Li, Y.L. (2020). A new tooth profile modification method of cycloidal gears in precision reducers for robots. *Applied Sciences*, vol. 10, no. 4, art. ID 1266, **DOI:10.3390/app10041266**.

[29] Li, T.X., Li, J.F., Deng, X.Z., Tian, M., Li, Y.L. (2020). Quantitative correction method for the grinding errors of cycloidal gears in precision reducer. *Journal of Advanced Mechanical Design, Systems, and Manufacturing*, vol. 14, no. 4, art. ID JAMDSM0052, **DOI:10.1299/jamdsm.2020jamdsm0052**.

[30] Gonzalez-Perez, I., Fuentes-Aznar, A. (2018). Implementation of a finite element model for gear stress analysis based on tie-surface constraints and its validation through the Hertz's theory. *Journal of Mechanical Design*, vol. 140, no. 2, art. ID 023301, **DOI:10.1115/1.4038301**.

[31] Xu, H., Shi, Z.Y., Yu, B., Wang, H. (2019). Optimal measurement speed and its determination method in the transmission precision evaluation of precision reducers. *Applied Sciences*, vol. 9, no. 10, art. ID 2146, **DOI:10.3390/app9102146**.

[32] Song, M., Wang, H.L., Liu, H.O., Peng, P., Wang, X.H., Pi, D.W., Yang, C., He, G. (2018). Double-layer control of an automatic mechanical transmission clutch during commercial vehicle start-up. *Strojniški Vestnik - Journal of Mechanical Engineering*, vol. 65, no. 9, p. 515-524, **DOI:10.5545/sv-jme.2019.6144**.

[33] Chen, Y.Z., Li, Z., Xie, X.D., Lyu, Y.L. (2018). Design methodology for coplanar axes line gear with controllable sliding rate. *Strojniški Vestnik - Journal of Mechanical Engineering*, vol. 64, no. 6, p. 362-372, **DOI:10.5545/sv-jme.2017.5110**.

Strojniški vestnik - Journal of Mechanical Engineering 66(2020)11, 668-676
DOI:10.5545/sv-jme.2020.6810
Original Scientific Paper
Received for review: 2020-06-07
Received revised form: 2020-08-24
Accepted for publication: 2020-10-06

Research on the Performance of a New External Occlusion Device for Pressure Vessel Leakage

Hongwei Yan – Xiong Yang – Xiangrong Hou – Lu Wang– Pengcheng Li
North University of China, School of Mechanical Engineering, China

Given the advantages and disadvantages of the existing plugging technology, a new type of external sealing device for pressure vessel leakage is proposed, which has the advantages of fast installation speed, small installation resistance, and stronger adaptability to the leakage surface. The connecting rod propulsion mechanism provides power, uses the fluidity of materials in the annular cavity to adapt to the complex curved surface, and carries out real-time monitoring and self-healing of the plugging process. Through the establishment of a finite element model of conventional top pressure plugging and the new type of external sac plugging method, simulation analysis of the leakage point and the pressure distribution around the crack leak has shown that: in the installation process of the new type of external liquid sac plugging device, a pressure-equalizing contact area and a sealing area are formed around the leakage point, and there is no obvious stress concentration phenomenon. When the thickness of the gasket is low, the deformation is uniform, which overcomes the problems of insufficient adaptability of the gasket in the conventional jacking method, and enhances the stability and reliability of emergency plugging.
Keywords: leakage, diversion channel, ANSYS, fluid capsule sealing, adaptive contact

Highlights
- *A new type of external occlusion device based on magnetic installation and linkage mechanism was designed to provide power for real-time monitoring and maintenance.*
- *A finite element model was established to analyse the sealing performance.*
- *Compared with the traditional method, the effective sealing area of the new liquid capsule sealing method is increased to 90 %.*
- *When the thickness of the gap is small, it is easy to install, the thickness of the gasket is small, and the effective sealing area is increased.*

0 INTRODUCTION

With the development of the process industry, pipeline transportation has been rapidly developed turned into an economically dangerous medium on a global scale [1] and [2]. Leakage accidents caused by self-defects [3], environmental factors [4] and human factors [5] have occurred, causing huge casualties, environmental pollution, and waste of resources. Therefore, there is an urgent need for a fast, effective, and safe plugging equipment for the treatment and disposal of accident pipelines and storage tanks, the control of dangerous sources, and the reduction of the harm caused by leakage [6] and [7].

In recent years, some emergency blocking repair methods have appeared at home and abroad [8] and [9]. The Furman-ITE company (USA) developed the open hole-plugging device as one of the earliest professional technical companies to solve the problem of pipeline leakage [10]. With the gradual maturity of the technology, the TDW company (USA) has developed a two-way isolation and repair equipment. The system can remotely control and isolate the pipeline with fluid medium [11]. The intelligent in-tube occlusion developed by Bowie is composed of a traction unit, a plugging unit, and a braking unit, which has the advantages of a simple structure [12]. Due to the different physical and chemical properties of materials and various leakage modes, there are many unforeseen technical problems in the emergency treatment and disposal of leakage accidents at this stage [13] and [14]. In observations of leakage problems, such as holes and cracks in large pipelines and storage tanks, a new type of external plugging device is proposed. Through the simulation analysis of the installation positioning and sealing process of the plugging device, the conclusion is drawn that, the new external plugging device has faster installation speed, smaller installation resistance, and stronger adaptability to the leakage surface in comparison with the conventional plugging method.

1 STRUCTURE AND PRINCIPLE

In this paper, a new external sealing device is proposed to address the leakage problems such as holes and cracks in large pipelines and storage tanks. The design indexes of the device are shown in Table 1.

The new sac-sealing device primarily comprises a permanent magnet module, a universal joint, a beam, a propulsion mechanism, and a plugging component. The device uses magnetic adsorption to locate the

*Corr. Author's Address: School of Mechanical Engineering, North University of China, Taiyuan, China, aweigeyan@nuc.edu.cn

leak. The strong magnetic force generated by the two permanent magnet modules is used to install and fix the device on the work surface to achieve the positioning and installation of the blocking device. The permanent magnet module is connected with the beam through the universal joint to form the static-bearing structure of the blocking device, which can be rotated around the hinge to adapt to the installation requirements of the sealing surface with different radius of curvature; thus, the adaptability of the device is enhanced to some extent. The two propulsion mechanisms are installed between the beam and the blocking assembly. The thrust generated by the self-motor is used as the power. The sealing assembly is pressed against the leakage sealing working surface to perform the sealing operation. The model of the occlusion device is shown in Fig. 1.

Table 1. *Design index of external occlusion device for pressure vessel leakage*

Serial number	Design index	
1	Pipe diameter [mm]	≥ 500
2	Minimum radius of curvature of elbow [mm]	≥ 250
3	Under maximum pressure [MPa]	$1.6 \leq P < 10.06$
4	Leakage rate of leakage port [kg/s]	0.08
5	Equipment capacity [kg]	12
6	Two magnets load bearing [kg]	2000
7	Effective treatment of maximum crack size [m^2]	0.00006

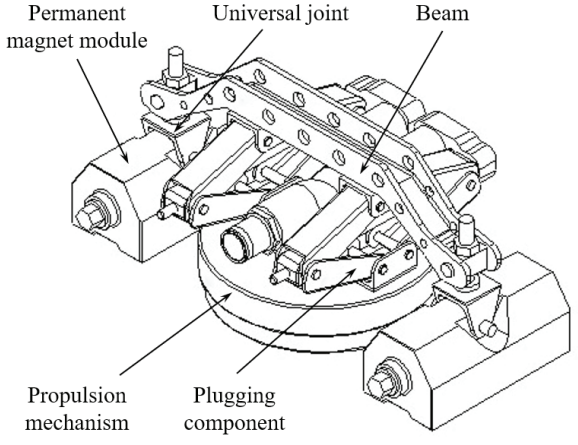

Fig. 1. *Schematic diagram of the plugging device mode*

When a leak occurs, the first task is to determine the shape or location of the leak. The magnetic force of the two permanent magnet modules is closed by the magnetic switch, the flow guiding channel of the blocking assembly is aligned with the leakage point, and the screw on the universal hinge is adjusted to find the suitable mounting position of the permanent magnet module. Then, the magnetic force of the two permanent magnet modules is turned on, to be adsorbed on the wall of the pipe around the leaking point, and the installation and fixing of the blocking device are completed. Finally, two propulsion devices are started (both synchronous and asynchronous according to the blocking condition) to push the plugging component to the blocking working surface.

During the process of contacting the sealing surface of the plugging device with the tube wall, the fluidity and pressure transferability of the fluid material in the annular chamber are utilized to convert the concentrated load loaded on the housing by the propulsion mechanism into the internal pressure of the fluid in the chamber, which is applied vertically, which allows the pressure load on the plugging surface to be evenly distributed. In this way, the phenomenon of stress concentration caused by local extrusion of sealing cushion in conventional top pressure plugging technology can be avoided [15].

The leak detection system in the occlusion device can monitor the pressure of the fluid in the cavity. After reaching a predetermined plugging pressure, the propulsion mechanism stops moving; the screw self-locking thus maintains a stable plugging pressure. At this moment, the harmful substances leaked into the emergency diversion pipe connected to the diversion channel, and the electromagnetic valve can also be installed at the expansion interface to close the valve to complete the sealing operation.

A sound wave collector (which can also monitor small leaks) is installed at the expansion interface. After the plugging is completed, the flow state of the fluid in the pipe and the plugging state of the plugging device are monitored in real time [16] and [17]. If the plugging fails, the shape of the leak is characterized by the acoustic signal of the fluid; a command is then issued to the propulsion mechanism to enhance the plugging pressure to block the operation again [18].

2 INSTALLATION AND POSITIONING ANALYSIS

This paper establishes the common hole leakage and crack leakage models in pipeline and storage tank leakage accidents.

2.1 Principle Analysis

The new type of liquid bag outer plugging device uses a permanent magnet module similar to a permanent magnet jack to complete the installation

and positioning process. During the plugging process, sufficient pressure must be applied to prevent the internal pressure of the leaking fluid from causing the plugging device to fall off. No bolts are required during installation. The minimum radius of the pipeline curvature that the new external plugging device is adapted to is 250 mm.

When the pipeline is corroded by material or impacted by an external force, perforation or cracks often occur [19] and [20]. In such cases, it is necessary to seal the leakage point. Due to the high internal pressure and high energy density of the leaking materials at most of the leakage points, a Bernoulli equation is selected to express the fluid energy at the leakage point [21] and [22]. The plugging mainly deals with the fluid state at the leakage point; there will be no large displacement in the vertical direction. The change in potential energy has little effect on the energy density of the fluid, which can be ignored [23]. Bernoulli's equation can be simplified as follows:

$$C = p + \frac{1}{2}\rho v^2, \tag{1}$$

C is the energy per unit volume of fluid, p is fluid pressure, ρ is fluid density, and v is fluid velocity.

The energy density of the fluid directly determines the difficulty of the plugging operation. The existing external plugging technology is pressed with a sealing material at the leak point to achieve the plugging operation. With the top pressure plugging as an example [24], the sealing process is shown in Fig. 2.

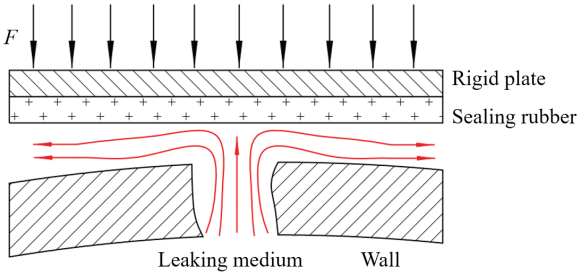

Fig. 2. *Schematic of hole leakage pressure seal*

When the sealing surface of the occlusion device gradually approaches the leak point, the flow pattern of the leaked material is forced to change. The fluid material ejected from the leaking point enters the crevice formed by the sealing surface of the occlude and the wall of the vessel. The narrowing of the crevices hinders the flow of the fluid, and the flow rate of the material continuously decreases until it reaches zero. In this process, accompanied by the energy loss caused by internal irregular flow [25], Eq. (1) can be rewritten as:

$$C = p + \frac{1}{2}\rho v^2 + Q, \tag{2}$$

Q is heat generated by friction during unit volume fluid flow (assuming heat is not transferred)

The main factor affecting the installation of the plugging device is the static pressure $F = p \cdot S$ of the fluid acting on the plugging device [26], which is obtained by the Eq. (2):

$$F = \int \left[C_0 - \left(\frac{1}{2}\rho v^2 + Q \right) \right] ds, \tag{3}$$

$$C_0 = p_0 + \frac{1}{2}\rho v_0^2, \tag{4}$$

$$Q = \lambda \cdot \frac{1}{2}\rho v^2, \tag{5}$$

F is installation resistance, C_0 is the raw energy density of the leaked material, S is the area of the sealing surface of the plugging device, p_0 is the pressure of the original fluid in the container, v_0 is the velocity of the original fluid in the container and λ is fluid friction coefficient.

It can be obtained from Eq. (3) that the main factors affecting the installation resistance of the plugging device are:

1. The energy density of the leaking material itself (the pressure and flow rate).
2. The coefficient of flow friction of the leaked material is determined by the shape of the leak and the geometry of the sealing surface of the plugging device.
3. The size of the sealing surface of the plugging device.

As shown in Fig. 2, the material ejected from the leak point collides with the sealing surface that is constantly approaching, and the kinetic energy is converted into static pressure in the impact region, forcing the fluid material to enter the nip. As the thickness of the gap decreases, λ gradually increases, the flow rate v_0 of the material decreases continuously, and the static pressure region at the leak point diffuses into the nip, forming an annular static pressure zone with different gradients around the leak point, and the installation resistance is large, the installation resistance has increased significantly.

In observation of the above problems, the occlusion of the new type of sac-sealing device adopts a diversion installation method, which is installed first and then blocked by a valve to reduce the installation

resistance of the occlusion device, so as to make the installation and positioning more accurate and reliable. The specific process of implementing the plugging operation is shown in Fig. 3.

During the installation process, most of the fluid material ejected from the leaking point flows out of the flow channel of the occlude, as shown in Fig. 3. Part of the fluid enters the nip, and a small part hits the sealing surface of the occlusion device, which effectively restrains the conversion of the kinetic energy of the fluid material to the pressure energy. The fluid flow rate and static pressure entering the nip are greatly reduced, which further greatly reduces the load on the sealing surface of the occlusion.

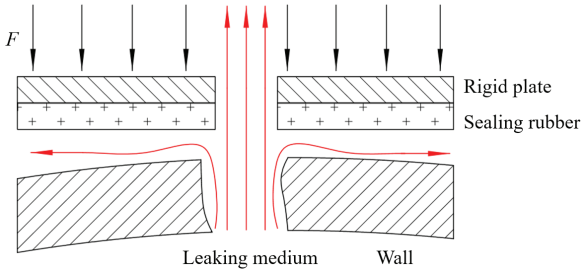

Fig. 3. *Schematic diagram of diversion plugging*

2.2 Flow Field Velocity Analysis

At present, the most common form of leakage in pipelines and tanks is crack leakage [27] and [28]. Two different leak point models, a hole with a diameter of 50 mm and a crack with a width of 4 mm and a length of 100 mm, are used to simulate the above method [29]. Both leakage models are based on a cylindrical storage tank with a radius of 3000 mm. The inside of the tank is a methane gas with a pressure of 1 MPa, the external pressure is 0.1 MPa, and the sealing surface of the occlusion is a circular area with a diameter of 190 mm, and the diameter of the reverse flow passage is 40 mm. Due to the large volume of the tank, the following approximate assumptions can be made: (a) the pressure in the tank is not affected by the leakage; (b) the pressure loss caused by the friction in the vessel after the leakage is ignored. The results of the analysis are shown in the figure below.

The gap between the sealing surface and the outer wall of the tank is 4 mm. The flow field characteristics of the non-conducting plugging device are shown in Fig. 4. The leaked fluid material flows out from the nip, forming a flow field with a high flow velocity (100 m/s) on both sides of the crack. The flow field characteristics of the diversion blocking device are shown in Fig. 5. Only a small amount of material flows out of the nip at a relatively low flow rate (56 m/s), and most of the material flows out of the device through the flow-guiding channel. In this way, part of the material can be recovered through the flow guiding channel, the leakage amount of the fluid material in the tank is reduced, the spraying speed of the fluid in the nip is reduced, the influence of the fluid jet on the sealing operation is reduced, and the safety factor is enhanced.

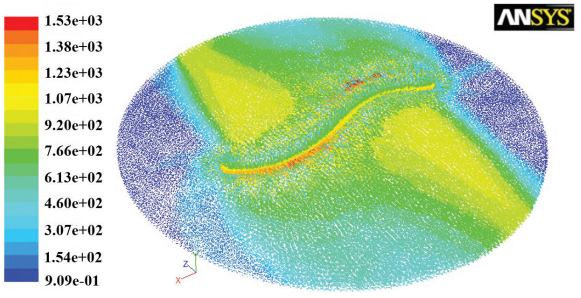

Fig. 4. *Flow field vector in the case of no diversion plugging device 4 mm*

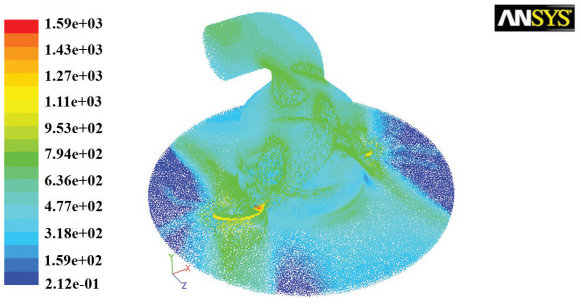

Fig. 5. *Flow field vector graph of the diversion and closure device with 4 mm*

2.3 Crack Thickness Analysis

The thickness of the nip affects the ejection speed of the leaked material and determines the ease of sealing operation. The clamping resistance of the two models (step size 5 mm) is used as a variable to simulate the installation resistance of the two blocking devices during the installation process. The results are shown in Fig. 6.

During the installation of the plugging device, the mounting resistance is not significantly different between the two plugging methods when the thickness of the gap is large (>30 mm). In this case, the proportion of the fluid material passing through the flow guiding channel is small, and the influence on the overall flow field is small, and the installation resistance changes of the two occlusions are basically the same. When the thickness of the gap is reduced, the

fluid motion resistance increases, forcing the material flow in the diversion channel to increase, and the installation resistance shows a difference. Compared with the non-diversion channel, the diversion channel reduces the peak of the installation resistance by nearly 36 %.

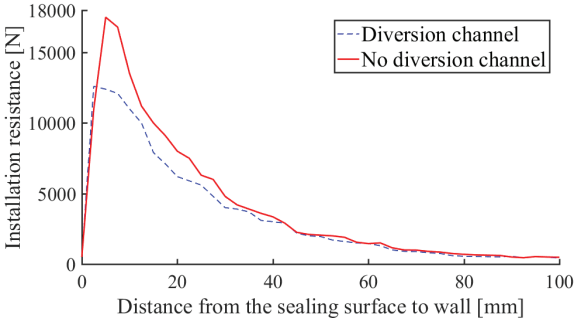

Fig. 6. *Comparison of the resistance in the process of crack leakage model*

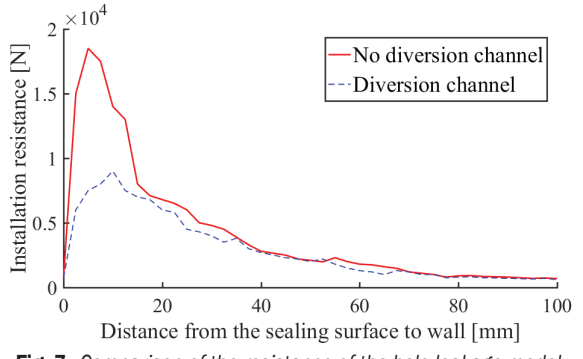

Fig. 7. *Comparison of the resistance of the hole leakage model*

The same analysis was done for the hole leakage model. The results are shown in Fig. 7. The peak value of the mounting resistance was reduced by nearly 53 %. It can be seen that the diversion function is affected by the geometry of the leakage point, and the corresponding diversion channel needs to be designed for the specific leakage form to meet the requirements of the diversion. Similar results were obtained when the medium in the tube was changed from gas to liquid water.

3 PLUGGING PROCESS ANALYSIS

This paper compares the sealing process of the device with the conventional top pressure sealing method.

3.1 Principle Analysis

Large pipes and pressure vessels are most common in small hole leaks or cracks at welds and are representative. It is necessary to analyse the stress distribution of the plugging device at the weld [30] and [31].

The existing large-scale storage tanks are mostly sealed with the top pressure sealing method. The loading is applied on the rigid body, and the flexible composite rubber is pressed on the sealing working face to form the plugging area [32]. The working principle is shown in Fig. 8.

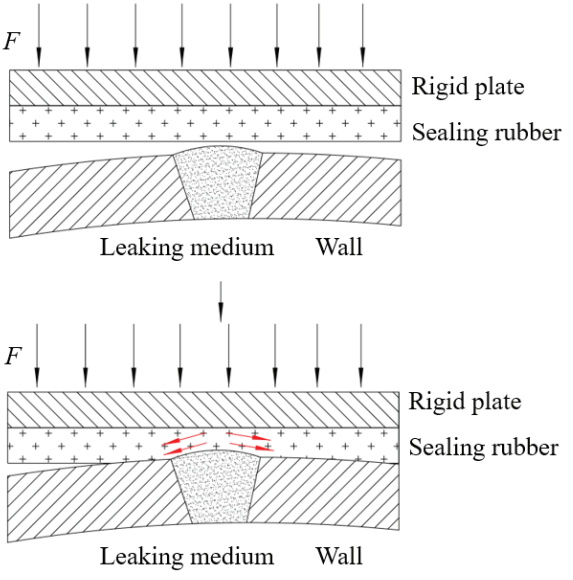

Fig. 8. *Principle of common top pressure plugging*

When sealing irregular surfaces, such as welds, the sealing rubber gaskets must use their deformation to adapt to the undulating changes of the curved surface. In non-linear large deformation weld, rubber material can be regarded as volume incompressible continuum, and the internal stress state will be uneven during deformation [33]. In the non-linear large deformation weld, the rubber material can be approximated as a volume incompressible flow body, and local flow phenomenon of the internal material occurs during the deformation process. The rubber element has the following stress relationship inside the compression deformation.

$$\sigma = \frac{E\alpha\left[\left(1+\varepsilon\right)-\left(1+\varepsilon\right)^{-2}\right]}{3}, \tag{6}$$

$$\varepsilon = \frac{f}{h}, \tag{7}$$

σ is internal stress of rubber components, $E\alpha$ is the elastic modulus of rubber components, ε is the strain of rubber components, f is the shaped variable of

rubber component and h is the thickness of rubber component.

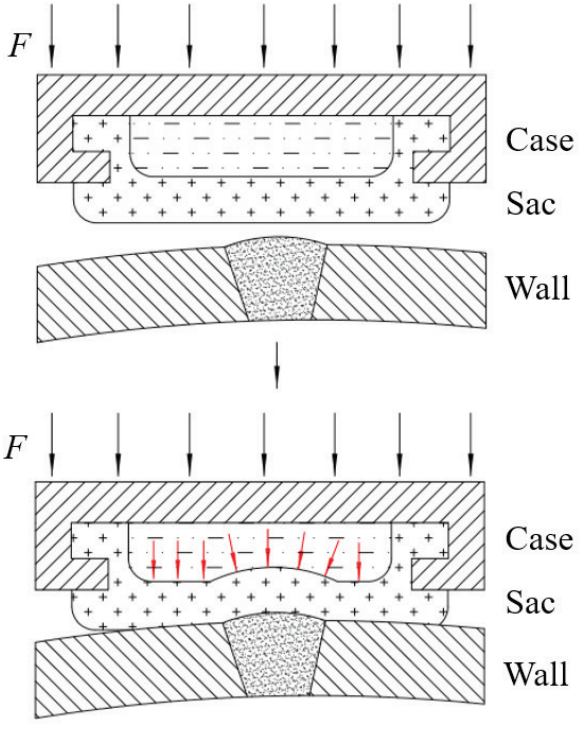

Fig. 9. *Schematic diagram of loading and sealing of the liquid bag*

Rubber materials use their deformation to adapt to the ups and downs of the curved surface, which makes the internal stress state of the material uneven. At the same time, when the material is compressed, it will produce the shear stress to prevent the deformation of the material. The welding seam imposes constraints on the rubber material, which enhances the longitudinal bearing capacity and further promotes uneven stress. To avoid this situation, this article uses the fluid pressure loading method to perform the plugging. The plugging process is shown in Fig. 9.

3.2 Analysis of Pressure Distribution

In this paper, the leakage model of the tank weld with the outer wall radius of 3000 mm is established as the blocked object. The weld height is 5 mm, and the width is 40 mm. There is a crack with a length of 100 mm on the weld. The conventional top pressure plugging method and the liquid bag plugging method were used for plugging respectively. The plugging pressure load was set at 1 MPa, and the sealing gasket material was set as NBR. The simulation results are shown in Figs. 10 and 11.

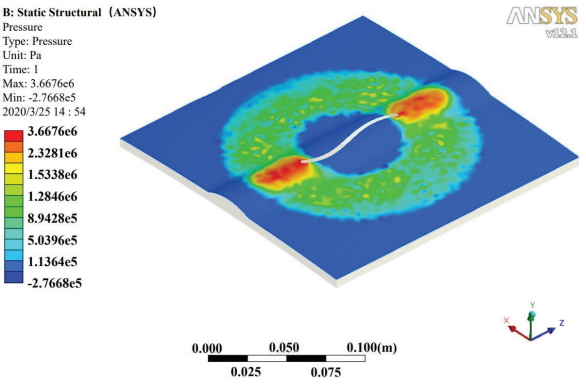

Fig. 10. *Sealing surface pressure of conventional sealing method*

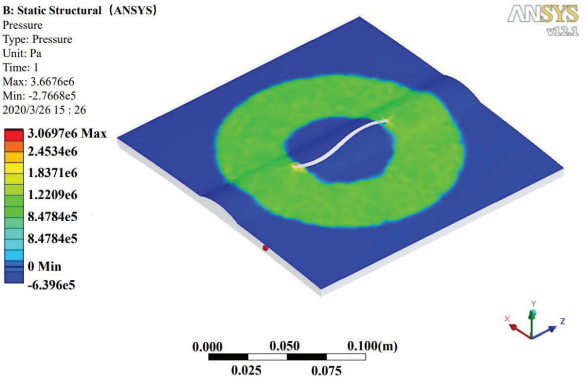

Fig. 11. *Pressure of the sealing surface of the liquid reservoir sealing method*

As can be seen from Figs. 10 and 11, the conventional sealing method only uses the deformation of the rubber material to adapt to the concave and convex fluctuation of the sealing surface, resulting in a strong stress concentration area at the convex part of the weld, which becomes an obvious high-pressure area, while the annular area outside the weld is a low-pressure area, which has a great potential safety hazard.

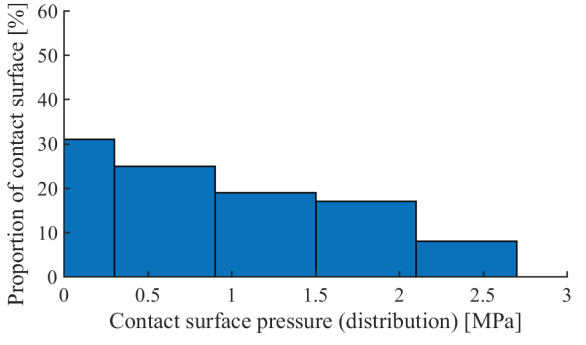

Fig. 12. *Pressure section of conventional sealing method*

In the new sac-sealing device, the sealing gasket forms a pressure-sensitive contact sealing zone (0.9 MPa) around the leak point around the crack, and no obvious low-pressure annular region appears. The pressure distribution of the sealing surface was counted to obtain the results of Figs. 12 and 13.

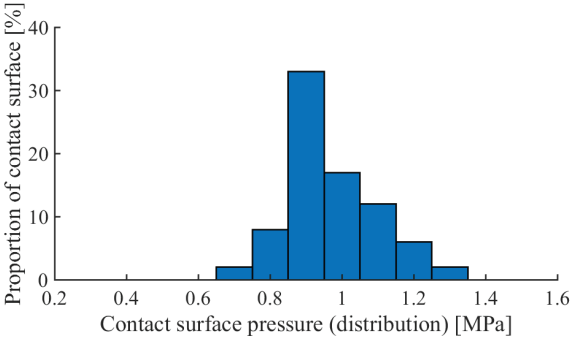

Fig. 13. *Pressure section of sealing surface of liquid reservoir*

The pressure distribution of the contact surface affects the working effect of the plugging device. Assuming that more than 90 % (0.9 MPa) of the plugging load is the effective plugging pressure, a large number of low-pressure (less than 0.9 MPa) areas appear on the contact surface of the conventional plugging method, reaching 56 % of the total area, and the effective plugging surface is only about 44 %. In the new method of sealing the outer capsule, the effective sealing area reaches nearly 90 %, mainly distributed between 0.9 and 1.2 MPa, and the load is evenly transmitted to the sealing working surface.

3.3 Seal Thickness Analysis

The thickness of the gasket is also a key factor affecting the sealing performance, which determines the sealing performance of the sealing device. Based on the above model, the two plugging methods are further simulated and analysed with the thickness of the gasket as a variable. The results obtained are shown in Fig. 14.

The conventional plugging methods use the material properties of rubber pads to accommodate irregular sealing surfaces around leak points. When the thickness is small, the adaptability of the gasket is poor, and the proportion of forming an effective sealing surface is also low. As the thickness of the gasket increases, its self-adaptation ability gradually increases, and the proportion of the effective sealing surface increases. When the thickness is 24 mm, the peak value (76 %) is reached. Due to the lack of corresponding constraints on the outer side of the gasket cylinder, the rubber material is forced to flow out from the side, resulting in a decrease in the bearing capacity of the rubber material and a low-stress phenomenon. As the thickness increases, the phenomenon becomes more apparent, and the proportion of the effective pressure region is also reduced.

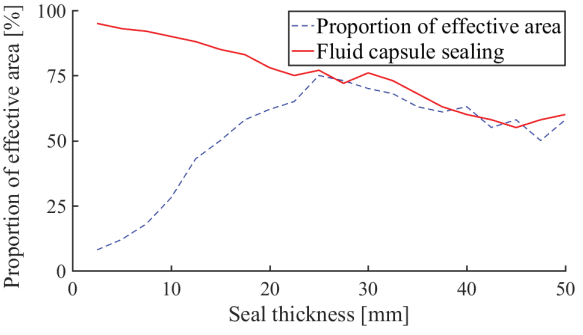

Fig. 14. *Product ratio curve distribution of effective sealing surface under different sealing surface thickness*

The novel capsular plugging method utilizes the fluidity of the liquid in the chamber to convert the load on the housing into fluid pressure and load it on the gasket. During the sealing process, the deformation of the thickness direction of the gasket is relatively uniform, which overcomes the shortage of the adaptability of the gasket in the conventional sealing method, and the effective pressure region formed is improved. When the thickness is small, the effective area ratio of the plugging reaches about 90 %. As the thickness increases, the sac-sealing method also shows the same proportion of decline. Similar results were obtained in simulation analysis under different pressures.

4 CONCLUSIONS

In this paper, the finite element model is established, and ANSYS is used to simulate and analyse the installation and sealing process of the conventional top pressure plugging device and the proposed new external sealing device.

1. During the installation process, when analysing the flow field velocity on both sides of the crack, it was found that only a small part of the material flowed out from the gap, and most of the material flowed out from the diversion channel, which was effectively recovered. When analysing the thickness of the gap, it was found that when the thickness of the gap is small, the installation resistance of the sac plugging method is smaller.

2. During the plugging process, an analysis of the pressure distribution around the leak found that compared with the traditional plugging method, the effective plugging area was increased to nearly 90 %, and the pressure distribution was more uniform. The analysis of the thickness of the gasket found that the smaller the thickness, the stronger the adaptability of the sac plugging method, the uniform shape change of the gasket, and the larger the effective sealing area and the longer the life.

5 ACKNOWLEDGEMENTS

The work described in this article is supported by the Research Project Supported by Shanxi Scholarship Council of China (2020-110) the Key Technology Research and Development Program of China's Shanxi Province (201603D321117) and the Natural Science Foundation of China's Shanxi Province (2013011026-2), which is mainly reflected in the innovation of plugging device. Moreover, the author sincerely thanks Professor Wu Wenge of North University of China for his critical discussion and reading in the process of manuscript preparation.

6 REFERENCES

[1] Liu, Y., Cheng, Q.L., Gan, Y.F., Wang, Y.X., Li, Z.D., Zhao, J. (2019). Multi-objective optimization of energy consumption in crude oil pipeline transportation system operation based on exergy loss analysis. *Neurocomputing*, vol. 332, p. 100-110, **DOI:10.1016/j.neucom.2018.12.022**.

[2] Cheng, Q.L., Zheng, A.B., Yang, L., Pan, C.L., Sun, W., Liu, Y. (2018). Studies on energy consumption of crude oil pipeline transportation process based on the unavoidable exergy loss rate. *Case Studies in Thermal Engineering*, vol. 12, p. 8-15, **DOI:10.1016/j.csite.2018.02.005**.

[3] Xu, H.F., Bbosa, B., Pereyra, E., Volk, M., Manna, M.S. (2018). Oil transportation in pipelines with the existence of ice. *Journal of Loss Prevention in the Process Industries*, vol. 56, p. 137-146, **DOI:10.1016/j.jlp.2018.08.015**.

[4] Yang, S., Jeon, K., Kang, D.J., Han, C.H. (2017). Accident analysis of the Gumi hydrogen fluoride gas leak using CFD and comparison with post-accidental environmental impacts. *Journal of Loss Prevention in the Process Industries*, vol. 48, p. 207-215, **DOI:10.1016/j.jlp.2017.05.001**.

[5] Liu, Q., Yu, H.Y., Zhu, G.C., Wang, P.B., Song, S.Y. (2020). Investigation on leakage cause of oil pipeline in the west oilfield of China. *Engineering Failure Analysis*, vol. 113, art. ID 104552, **DOI:10.1016/j.engfailanal.2020.104552**.

[6] Jia, Z.G., Ho, S.-C., Li, Y., Kong, B., Hou, Q.M. (2019). Multipoint hoop strain measurement-based pipeline leakage localization with an optimized support vector regression approach. *Journal of Loss Prevention in the Process Industries*, vol. 62, art. ID 103926, **DOI:10.1016/j.jlp.2019.103926**.

[7] Wang, C.L., Li, Y.X., Teng, L., Gu, S.W., Hu, Q.H., Zhang, D.T., Ye, X., Wang, J.H. (2019). Experimental study on dispersion behavior during the leakage of high-pressure CO_2 pipelines. *Experimental Thermal and Fluid Science*, vol. 105, p. 77-84, **DOI:10.1016/j.expthermflusci.2019.03.014**.

[8] Chaudhari, P., Zerpa, L.E., Sum, A.K. (2018). A correlation to quantify hydrate plugging risk in oil and gas production pipelines based on hydrate transportability parameters. *Journal of Natural Gas Science and Engineering*, vol. 58, p. 152-161, **DOI:10.1016/j.jngse.2018.08.008**.

[9] Qu, Z., Wang, Y., Yue, H., An, Y., Wu, L., Zhou, W., Wang, H., Su, Z., Li, J., Zhang, Y, Wang, L., Yang, X., Cai, Y., Yan, D. (2017). Study on the natural gas pipeline safety monitoring technique and the time-frequency signal analysis method. *Journal of Loss Prevention in the Process Industries*, vol. 47, p. 1-9, **DOI:10.1016/j.jlp.2017.02.016**.

[10] An, Y., Wang, X., Yue, B., Wu, L., Qu, Z., Yue, H., Yan, D. (2018). Natural gas pipeline safety monitoring technique based on chaotic characteristics of the detected signals. *Process Safety and Environmental Protection*, vol. 118, p. 279-284, **DOI:10.1016/j.psep.2018.07.007**.

[11] Wang, W., Guo, J., Fan, J., Zhang, S., Zhu, X., Wang, C. (2020). Research on the proportional-integral-derivative synchronous control method of the marine spherical isolation plug in the rotation process. *Proceedings of the Institution of Mechanical Engineers, Part M: Journal of Engineering for the Maritime Environment*, vol. 234, no. 4, p. 810-819, **DOI:10.1177/1475090220913704**.

[12] Park, S., Kim, H. (2014). Structural analysis of gas pipeline repaired by carbon fiber composite materials. *Journal of The Korean Institute of Gas*, vol. 18, no. 2, p. 62-68, **DOI:10.7842/kigas.2014.18.2.62**. (in Korean)

[13] Zhang, K., Huang, H., Duan, M.L., Hong, Y., Estefen, S.F. (2017). Theoretical investigation of the compression limits of sealing structures in complex load transferring between subsea connector components. *Journal of Natural Gas Science and Engineering*, vol. 44, p. 202-213, **DOI:10.1016/j.jngse.2017.03.034**.

[14] Kumar, R., Banerjee, S., Banik, A., Bandyopadhyay, T.K., Naiya, T.K. (2017). Simulation of single phase non-Newtonian flow characteristics of heavy crude oil through horizontal pipelines. *Petroleum Science & Technology*, vol. 35, no. 6, p. 615-624, **DOI:10.1080/10916466.2016.1266365**.

[15] Koc, P. (2019). An exacting wall-penetration pipe analysis. *Strojniški vestnik - Journal of Mechanical Engineering*, vol. 65, no. 3, p. 189-197, **DOI:10.5545/sv-jme.2018.5651**.

[16] Gupta, P., Zan, T.T.T., Wang, M., Dauwels, J., Ukil, A. (2018). Leak detection in low-pressure gas distribution networks by probabilistic methods. *Journal of Natural Gas Science and Engineering*, vol. 58, p. 69-79, **DOI:10.1016/j.jngse.2018.07.012**.

[17] An, Y., Wang, X.C., Yue, B., Qu, Z.G., Wu, L.Q., Chu, R.G. (2019). Compensation of sound velocity variation based on resampling algorithm for natural gas pipeline safety monitoring. *Measurement*, vol. 148, art. ID 106942, **DOI:10.1016/j.measurement.2019.106942**.

[18] Araújo, M.V., Neto, S.R.F, Lima, A.G.B., Luna, F.D.T. (2015) Hydrodynamic study of oil leakage in pipeline via CFD. *Advances in Mechanical Engineering*, vol. 6, art. ID. 170178, **DOI:10.1155/2014/170178**.

[19] Sievers, J., Heckmann, K., Pallas-Moner, G., Lerchl, G. (2015). Structural mechanical and thermal hydraulic aspects on the behavior of crack like leaks in piping. *Progress in Nuclear Energy*, vol. 84, p. 18-23, **DOI:10.1016/j.pnucene.2015.03.023**.

[20] Hasegawa, K., Li, Y.S., Lacroix, V., Mares, V. (2020). Application scope of limit load criterion for uctile material pipes with circumferentially external cracks. *Journal of Pressure Vessel Technology*, vol. 142, no. 3, p. 031506, **DOI:10.1115/1.4046055**.

[21] Boujleben, A., Ibrahimbegovic, A., Lefrançois, E. (2020). An efficient computational model for fluid-structure interaction in application to large overall motion of wind turbine with flexible blades. *Applied Mathematical Modelling*, vol. 77, p. 392-407, **DOI:10.1016/j.apm.2019.07.033**.

[22] Mohammadi, N., Asadi, H., Aghdama, M.M. (2019). An efficient solver for fully coupled solution of interaction between incompressible fluid flow and nanocomposite truncated conical shells. *Computer Methods in Applied Mechanics and Engineering*, vol. 351, p. 478-500, **DOI:10.1016/j.cma.2019.03.044**.

[23] Bohorquez, J., Alexander, B., Simpson, A.R., Lambert, M.F. (2020). Leak detection and topology identification in pipelines using fluid transients and artificial neural networks. *Journal of Water Resources Planning and Management*, vol. 146, no. 6, p. 04020040, **DOI:10.1061/(ASCE)WR.1943-5452.0001187**.

[24] Bbosa, B., Ozbayoglu, E., Volk, M. (2019). Experimental investigation of hydrate formation, plugging and flow properties using a high-pressure viscometer with helical impeller. *Journal of Petroleum Exploration and Production Technology*, vol. 9, p. 1089-1104, **DOI:10.1007/s13202-018-0524-6**.

[25] Jia Z.G., Ren, L., Li, H.N., Ho, S.C., Song, G.B.. (2015). Experimental study of pipeline leak detection based on hoop strain measurement. *Structural Control & Health Monitoring*, vol. 22, p. 799-812, **DOI:10.1002/stc.1718**.

[26] Guedri, A, Belyamna, M.A., Boutelidja, R., Djebbar, Y. (2019). Interpretation of the effect of hydrostatic test in components working under pressure. *Engineering Failure Analysis*, vol. 106, art. ID 104174, **DOI:10.1016/j.engfailanal.2019.104174**.

[27] Amara, M., Bouledroua, O., Hajd Meliani, M., Azari, Z., Tahar Abbess, M., Pluvinage, G., Bozic, Z. (2019). Effect of corrosion damage on a pipeline burst pressure and repairing methods. *Archive of Applied Mechanics*, vol. 89, p. 939-951. **DOI:10.1007/s00419-019-01518-z**.

[28] Shen, Y.P., Lin, Y.R., Li, P., Fu, Y.J., Wang, Y.Q. (2020). Simulation and detection leakage of underground water pipeline by ground penetrating radar. *Journal of Testing and Evaluation*, vol. 48, no. 3, p. 2003-2027, **DOI:10.1520/JTE20190181**.

[29] Raafat, E., Nassef, A., El-hadek, M., El-Megharbel, A. (2019). Fatigue and thermal stress analysis of submerged steel pipes using ANSYS software. *Ocean Engineering*, vol. 193, art. ID 106574, **DOI:10.1016/j.oceaneng.2019.106574**.

[30] Jiao, Z., Shuai, J. (2014). A cyclic internal pressure characteristics analysis of long-distance transmission pipelines. *Petroleum Science and Technology*, vol. 32, no. 1, p. 61-67, **DOI:10.1080/10916466.2011.582064**.

[31] Lu, H.F., Ma, G.G., Li, X.T., Wu, S.J. (2018). Stress analysis of LNG storage tank outlet pipes and flanges. *Energies*, vol. 11, no. 4, art. ID 877, **DOI:10.3390/en11040877**.

[32] Sohaib, M., Islam, M., Kim, J., Jeon, D.-C., Kim, J.-M.. (2019). Leakage detection of a spherical water storage tank in a chemical industry using acoustic emissions. *Applied Sciences*, vol. 9, no. 1, art. ID 196, **DOI:10.3390/app9010196**.

[33] Quan, D., Cardiff, P., Murphy, N., Ivankovic, A. (2018). Damage behaviour of nano-modified epoxy adhesives subject to high stress constraint. *The Journal of Adhesion*, vol. 94, no. 5, p. 387-405, **DOI:10.1080/00218464.2017.1279542**.

Strojniški vestnik - Journal of Mechanical Engineering 66(2020)11, 677-683

DOI:10.5545/sv-jme.2020.6836 Original Scientific Paper
Received for review: 2020-06-27
Received revised form: 2020-10-01
Accepted for publication: 2020-10-27

Thermodynamic Analysis of a Cascade Heat Pump Incorporated in High-Temperature Heating System

Nedžad Rudonja* – Milan Gojak – Ivan Zlatanović – Ružica Todorović
University of Belgrade, Faculty of Mechanical Engineering, Serbia

In this article is presented thermodynamic analysis of a cascade heat pump system designed for using in high-temperature heating systems. The own thermodynamic model was built by using properties of working fluids from the CoolProp base. The cascade heat pump was designed to use ambient air as heat source with temperature t_{amb}= –20 °C and for heating water in the high-temperature heating system up to 70 °C. The projected heating capacity of the cascade heat pump was 100 kW. The coefficient of performance (COP) of the cascade heat pump system due to use of different working mediums combinations in cycles of the cascade heat pump was investigated. For the best combination of working fluids (mediums) sub-cooling, super-heating, pressure loss in compressor's suction line, as well as exergy efficiency of the heat pump were analysed as a function of the mean temperature of the cascade heat exchanger.
Keywords: cascade heat pumps, working mediums, coefficient of performance, exergy efficiency

Highlights
- *The influence of different combinations of working mediums on thermodynamic characteristics of the cascade heat pump was studied.*
- *The influence of the mean temperature of the cascade heat exchanger on COP was analysed and obtained thermodynamically the optimum value of the mean temperature.*
- *The impact of sub-cooling, super-heating, pressure loss in compressor's suction line and isentropic efficiency of compressor on COP were analysed.*
- *The exergy efficiency of the heat pump was calculated for the best combination of working mediums and obtained its dependence on the mean temperature of the cascade heat exchanger.*

0 INTRODUCTION

Energy consumption permanently increases and consequently makes higher impact on environmental pollution and global warming [1]. Final energy consumption by end-users in residential sector was 25.4 % in overall final energy consumption in Europe in 2015 [2]. By improving energy efficiency of systems and using renewable energy resources, such as biomass, geothermal energy, energy obtained from solar thermal and photovoltaic systems, both energy consumption and environmental pollution can be greatly reduced. Heat pumps as energy efficient systems are widely used because of their closely neutral impact on environmental and global warming [3].

The selection of heat pump type depends on heat source, temperature of both heat source and heat sink, as well as the temperature range in witch heat pump operates [4]. Serbia has huge potential for utilization of hydro-geothermal water as heat source [5], but utilization of those heat sources depends on location and for this reason in this article was analysed an air source heat pump for utilization in high-temperature heating systems. Although water and ground as heat sources are thermodynamically more favourable, those types of sources require high investment and exploitation costs. On the other hand, air as heat source is less thermodynamically unfavourable, but it is easy to use and available at all locations.

Traditional heat pumps are suitable for low-temperature heating systems such as underfloor heating, low-temperature radiators or fan convection heaters [6]. When temperature range is too high, for instance, in high-temperature heating system, cascade heat pumps can be used as an economically acceptable solution [7] and better solution than single or two-stage heat pump [8] and [9]. Comparing to the single-stage heat pump, the compressors of a cascade heat pump has a smaller compression ratio and consequently heat pump achieves better performances.

In last decades, many researchers investigated various working mediums of heat pumps in order to improve their performance and consequently to maximize the coefficient of performance. In the article [10] was analysed several working mediums combinations in a cascade heat pump and thermodynamically the best case was with R600 in low-temperature (LT) circuit and R245fa in high-temperature (HT) circuit of the cascade heat pump (R600/R245fa). Ma et al. [11] analysed a high temperature cascade heat pump with R245fa (LT)

*Corr. Author's Address: University of Belgrade, Faculty of Mechanical Engineering, Serbia, nrudonja@mas.bg.ac.rs

and BY-3 (HT) as working mediums. They built the numerical model of the heat pump and validated model by own experimental results. Xu et al. [12] experimentally analysed a high temperature cascade heat pump for implementation in cold regions. The temperature of supply hot water was between 55 °C and 75 °C, while ambient temperature was –21 °C. As working medium in LT circuit was selected R404A, while in HT circuit it was R134a. The greatest COP, with water supply temperature near 55 °C, was 2.48. Song et al. [13] and [14] studied the characteristics of the CO_2 and R134a cycles in both combined and cascade system. The temperature of supply water was between 55 °C and 75 °C, while ambient temperature was varied from –20 °C up to 0 °C. Bhattacharyya et al. [15] optimized the cascade system for refrigeration as well as for heating using combination R744/R290 as working mediums. In the article [16] a mathematical model was built to enable the prediction of optimal value of the mean temperature of cascade heat exchanger for combination R134a/R410A of a cascade heat pump. In the article [17] analysed the influence of the mean temperature of the cascade heat exchanger on performance of an air source cascade heat pump system. The mean temperature has been proven as a key factor in affecting the operating performance for heat pump system.

In literature so far there are few articles for cascade air source heat pump that operates at low temperature and provides high-temperature heating [11]. On the other hand, in this research was investigated the effect of different working mediums combinations on the heat pump performances. Four combinations of working mediums were analysed with aim to obtain the combination that gives the highest values of COP for given temperature range. Temperature range was selected in order to cover possibility of heating buildings with high temperature heating systems by using outdoor air as heat source. The COP was calculated for each combinations of working mediums by changing the mean temperature of the cascade heat exchanger. The condensing temperature in HT circuit was 75 °C, while evaporating temperature in LT circuit was –25 °C. The heating capacity of the cascade heat pump was 100 kW. Furthermore, for the best combination of working mediums sub-cooling, super-heating, pressure loss in compressor's suction line, as well as exergy efficiency of the heat pump were analysed as a function of the mean temperature of the cascade heat exchanger. Obtained results are important for designers and engineers who design air source cascade heat pumps in given temperature range, because it was suggested the best combination of working mediums that gives the highest thermal performance of an air source cascade heat pump. Furthermore, scientists will have better insight of influence analyzed working phenomena on thermodynamic performances of cascade heat pump systems.

1 THERMODYNAMIC MODEL

A schematic diagram of an air source cascade heat pump system is presented in Fig. 1.

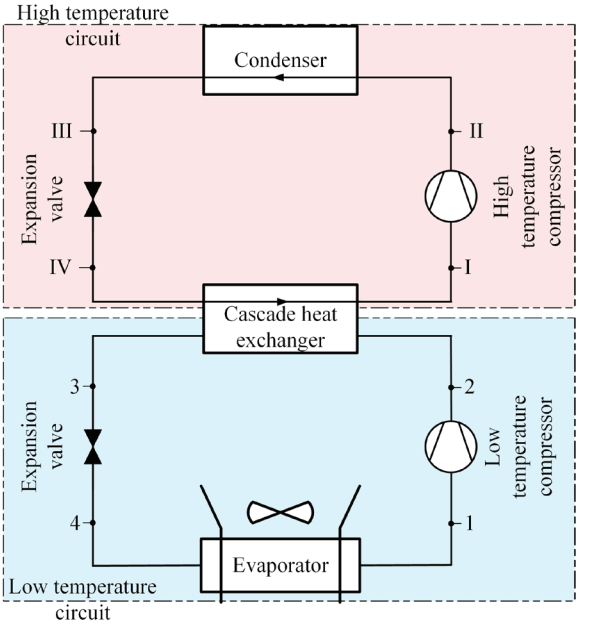

Fig. 1. *An air source cascade heat pump*

The heat pump consists of a low-temperature and a high-temperature circuits that are connected by a cascade heat exchanger. In this article all states of working mediums in low-temperature circuit are marked by arabic and in high-temperature circuit by roman numbers. Moreover, indexes of evaporating and condensing temperatures in LT circuit (T_e, T_c) were lower letters and upper letters for HT circuit (T_E, T_C).

Corresponding *T–S* diagram of cycles of the cascade heat pump is shown in Fig. 2.

To simplify analysis in the article following assumptions were used:

- Heat transfer processes in all heat exchangers were isobaric;
- Heat transfer between surroundings and pipeworks was neglected;
- Pressure losses in all pipeworks were neglected;

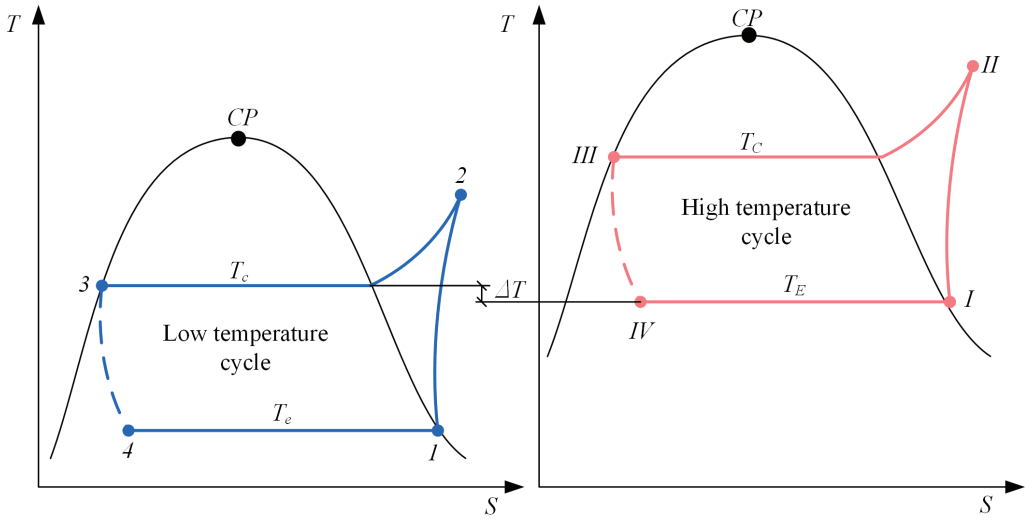

Fig. 2. *T–S diagram of process of the cascade heat pump*

- The difference between condensing temperature in LT and evaporating temperature in HT circuit was set at $\Delta T = 7$ K;
- Evaporating temperature in LT circuit was $T_e = 248$ K (for 5 K lower than the ambient air temperature);
- Condensing temperature in HT circuit was $T_C = 348$ K;
- Heating power of heat pump was $\dot{Q}_{out} = 100$ kW.

The mean temperature of the cascade heat exchanger was defined as:

$$T_m = \frac{T_E + T_c}{2}, \tag{1}$$

where T_E and T_c are evaporating temperature in HT and condensing temperature in LT circuit, respectively.

For given value of the mean temperature of the cascade heat exchanger, evaporating temperature in HT circuit as well as condensing temperature in LT circuit were calculated as:

$$T_E = T_m - \frac{\Delta T}{2}, \tag{2}$$

$$T_c = T_m + \frac{\Delta T}{2}. \tag{3}$$

The mass flow rate in HT circuit was calculated as following:

$$\dot{m}_{HT} = \frac{\dot{Q}_{out}}{h_{II} - h_{III}}, \tag{4}$$

where h_{II} and h_{III} are specific enthalpies of working medium in HT circuit at inlet and outlet of the condenser.

The power consumption of HT compressor is:

$$P_{c,HT} = \dot{m}_{HT}(h_{II} - h_I), \tag{5}$$

where h_I and h_{II} are specific enthalpies of working medium at inlet and outlet of HT compressor.

Based on introduced assumptions the heating capacity of LT circuit is equal to cooling capacity of HT circuit and follows:

$$\dot{Q}_{out,LT} = \dot{Q}_{in,HT} = \dot{Q}_{out} - P_{c,HT}, \tag{6}$$

where $\dot{Q}_{in,HT}$ is cooling capacity of HT circuit.

The mass flow rate of working medium in LT circuit is:

$$\dot{m}_{LT} = \frac{\dot{Q}_{out,LT}}{h_2 - h_3}, \tag{7}$$

where h_2 and h_3 are specific enthalpies of working medium at inlet and outlet of LT condenser.

The power consumption of LT compressor is:

$$P_{c,LT} = \dot{m}_{LT}(h_2 - h_1), \tag{8}$$

where h_1 and h_2 are specific enthalpies of working medium at inlet and outlet of LT compressor.

The *COP* of the cascade heat pump was calculated as:

$$COP_{HP} = \frac{\dot{Q}_{out}}{P_{c,LT} + P_{c,HT}}. \tag{9}$$

Exergy efficiency (the second-law efficiency) is measure of perfection of a system in given working conditions. It can be defined as the ratio of the thermal efficiency of the actual process compared to the reversible process. For heat pumps, exergy efficiency

can be defined as the ratio of the *COP* of actual heat pump cycle to *COP* of Carnot heat pump cycle, that operate between the same temperatures of heat source and heat sink [18]:

$$\eta_{ex} = \frac{COP_{HP}}{COP_{Carnot}}. \quad (10)$$

The isentropic efficiency of a compressor is defined as the ratio of the work input to an isentropic process to the work input to the actual process, which takes place between the same inlet and exit pressures. The isentropic efficiency of both compressors was same and defined as:

$$\eta_c = \frac{h_{out,i} - h_{in}}{h_{out} - h_{in}}, \quad (11)$$

where $h_{out,i}$ is specific enthalpy of the working medium at outlet of the compressor in the case of its isentropic compression.

2 RESULTS AND DISCUSSION

2.1 Working Mediums Selection - Basic Thermodynamic cycle

The first step of thermodynamic analysis, for given working conditions of the cascade heat pump, was conducted in order to obtain the best combination of working mediums in LT and HT circuits. Based on literature review, the next combinations of working mediums were used: R717 - R245fa, R245fa - R717, R134a - R600 and R1270 - R717. The results of conducted analyses are shown in Fig. 3. During simulations the mean temperature of the cascade heat exchanger was varied for all working mediums combinations and it was obtained that R245fa in LT and R717 in HT give the maximum value of COP. In this case the isentropic efficiency of compressors was η_c = 1.0, the cycles were without sub-cooling, super-heating and pressure loses at compressor's suction line.

Based on Fig. 3 it can be also concluded that the maximum value of *COP* for the combination R245fa/R717 was obtained for the mean temperature of cascade 21 °C as well as that for different working mediums combinations there is different value of the mean temperature of the cascade heat exchanger which gives maximum value of *COP*.

The next steps of thermodynamic analysis were conducted for the best working mediums combination R245fa/R717 and for thermodynamic cycles modified in accordance with the considered impacts.

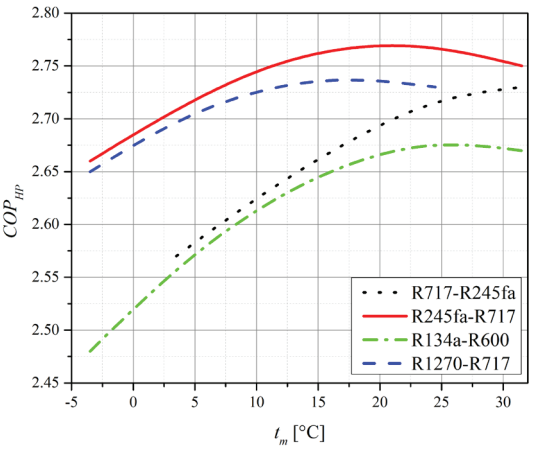

Fig. 3. *COP dependence on working mediums combinations and the mean temperature of the cascade heat exchanger*

2.2 The Impact of Sub-cooling

The influence of sub-cooling on COP is shown in Fig. 4. In this case the isentropic efficiency of the compressors was η_c = 1.0, the cycles were without super-heating and pressure loses at compressor's suction line.

In this case the temperature at outlet of the condenser was calculated using temperature of condensing in LT, i.e. in HT circuit as follows:

$$T_3 = T_c - \Delta T_{sc}, \quad (12)$$

$$T_{III} = T_C - \Delta T_{sc}, \quad (13)$$

where ΔT_{sc} is difference between corresponding the condensing temperature and the temperature at outlet of the condenser. In this case ΔT_{sc} was same for both LT and HT circuit.

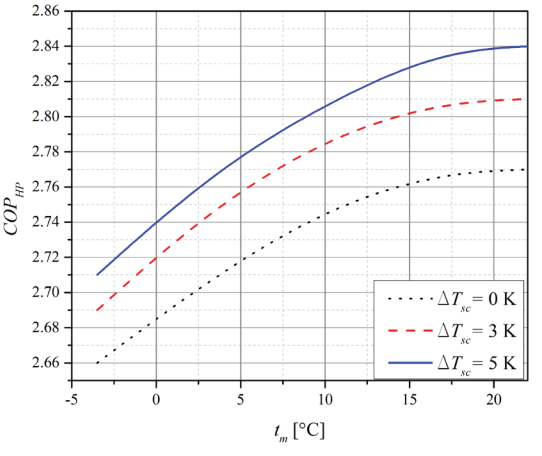

Fig. 4. *COP dependence on the mean temperature of the cascade heat exchanger and the temperature of sub-cooling*

From Fig. 4 it can be concluded that sub-cooling working medium for 5 K gives the increase in COP value for approximately 2.5 %.

The Experimental section should provide details of the experimental set-up and the methods used to obtain the results. To make this section interesting, explain the choices you made in your experimental procedure. This section should provide sufficient detail for other scientists to be able to reproduce the experiments presented in this paper.

2.3 The Impact of Super-heating

The influence of super-heating of working medium at inlet of the compressor on *COP* is shown in Fig. 5. In this case the isentropic efficiency of the compressors was $\eta_c = 1.0$, the cycles were without sub-cooling and pressure loses at compressor's suction line. In this case the temperature at inlet of the compressor was calculated using the temperature of evaporating in LT, i.e. in HT circuit as follows:

$$T_1 = T_e + \Delta T_{sh}, \tag{14}$$

$$T_I = T_E + \Delta T_{sh}, \tag{15}$$

where ΔT_{sh} was same for both LT and HT circuit.

From Fig. 5 it can be concluded that super-heating has small influence on *COP*, but it is still important from the point of view of compressor protection.

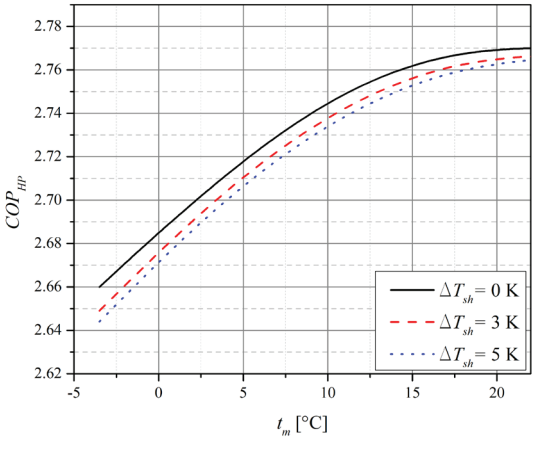

Fig. 5. *COP dependence on the mean temperature of the cascade heat exchanger and the temperature of super-heating*

2.4 The Impact of Pressure Looses at Compressor's Suction line

The influence of pressure loses at suction line of the compressor on *COP* for selected working mediums is shown in Fig. 6.

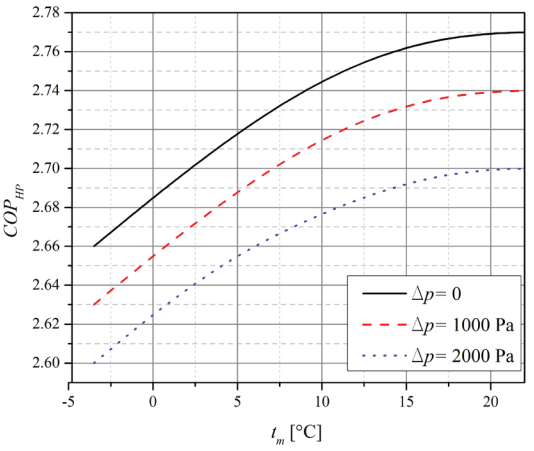

Fig. 6. *COP dependence on the mean temperature of the cascade heat exchanger and the loss of pressure at the compressor suction line*

In this case the isentropic efficiency of the compressors was was $\eta_c = 1.0$, the cycles were without sub-cooling and super-heating. The pressure of working mediums at inlet of the compressors were calculated as following:

$$p_1 = p_e - \Delta p, \tag{16}$$

$$p_I = p_E - \Delta p, \tag{17}$$

where p_e and p_E are functions of corresponding evaporating temperatures, i.e. $p_e = f(T_e)$ and $p_E = f(T_E)$. It can be concluded that pressure drop of 2000 Pa at the suction line produces the decrease in *COP* by approximately 2.5 %.

2.5 The Impact of Isentropic Efficiency of the Compressors

The influence of isentropic efficiency of the compressors on *COP* depending on the mean temperature of the cascade heat exchanger is shown in Fig. 7.

In this case the cycles were without sub-cooling, super-heating and pressure loses at compressor's suction line. As expected, it was shown that isentropic efficiency of the compressor (η_c) has considerable impact on *COP* and that dependence is a linear function Fig. 8, where maximum value of *COP* was obtained for optimum value of the mean temperature of the cascade heat exchanger (21 °C).

2.6 Exergy Efficiency

The maximum value of the exergy efficiency of the cascade heat pump for selected working mediums was calculated according Eq. (10) and obtained values

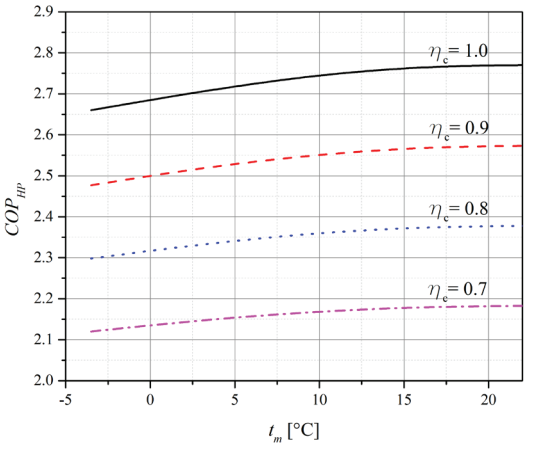

Fig. 7. *COP dependence on the mean temperature of the cascade heat exchanger and the isentropic efficiency of the compressors*

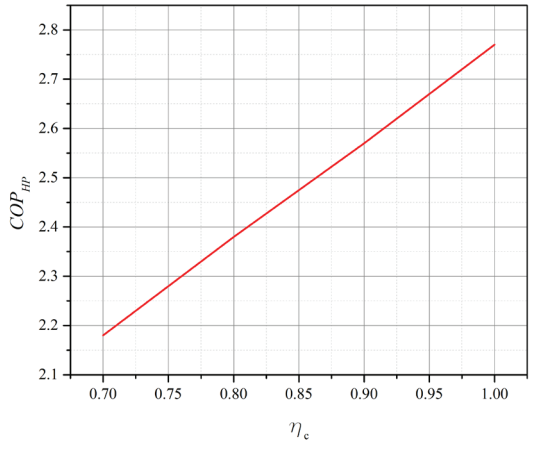

Fig. 8. *The maximum COP value depending on the isentropic efficiency of the compressors*

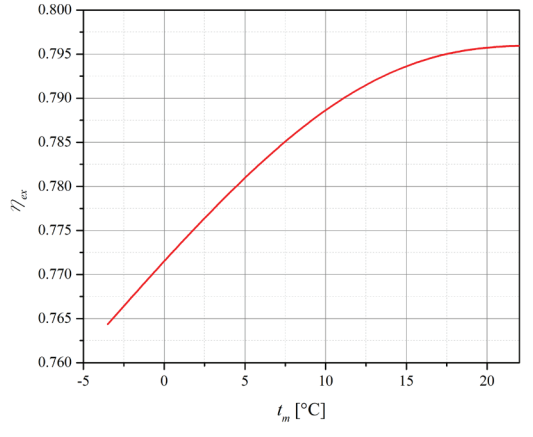

Fig. 9. *The exergy efficiency of the cascade heat pump depending on the mean temperature of the cascade heat exchanger*

are presented in Fig. 9. In this case the isentropic efficiency of the compressors was η_c = 1.0, the cycles were without sub-cooling, super-heating and pressure loses at compressor's suction line.

For analysed the cascade heat pump, for given assumptions, the maximum value of the exergy efficiency was about 0.796 which obtained for optimum value of the mean temperature of the cascade heat exchanger (21 °C). The character of dependence is same as the dependence of *COP*.

3 CONCLUSIONS

A cascade heat pump system can be used as heat source of high temperature heating systems. The combination of working mediums is very important from point of view energy efficiency of heat pump system. For given working conditions the best combination of working mediums was R245fa in low-temperature circuit and R717 in high-temperature heat pump circuit. The maximum value of the *COP* was 2.77 and it can be concluded that use of cascade heat pumps in high-temperature heating systems is justified. For each combination of working mediums there is the optimal value of the mean temperature of the cascade heat exchanger that gives maximum value of *COP*. The pressure loses at compressor's suction line by 2000 Pa contributes to decreasing in *COP* for closely 2.5 %. Sub-cooling working mediums at outlet of the condenser for 5 K gives the increase of *COP* value approximately by 2.5 %. Super-heating of working mediums at the compressor inlet is important for compressor protection but has a small and negative impact on *COP* value. Decreasing of the isentropic efficiency of the compressors significantly decreases *COP* value as well as linearly impacts on it.

4 ACKNOWLEDGEMENTS

The research was conducted as a part of the agreement on realization and financing of scientific research work in 2020 between the Ministry of Education, Science and Technological Development of the Republic of Serbia and the Faculty of Mechanical Engineering in Belgrade - contract number: 451-03-68 / 2020-14 / 200105.

5 REFERENCES

[1] Bilgen, S., (2014). Structure and environmental impact of global energy consumption. *Renewable and Sustainable Energy Reviews*, vol.38, p. 890-902, **DOI:10.1016/j.rser.2014.07.004**.

[2] European Commision (2015). Energy, transport and environment - statistics on three closely related domains, from:

https://ec.europa.eu/eurostat/statistics-explained/index.php?title=File:Final_energy_consumption,_EU-28,_2015_(%25_of_total,_based_on_tonnes_of_oil_equivalent).png, accessed on 2020-06-01.

[3] Hammond, G.P., Norman, J.B. (2014). Heat recovery opportunities in UK industry, *Applied Energy*, vol. 116, p. 387-397, **DOI:10.1016/j.apenergy.2013.11.008**.

[4] Boahen, S., Anka, S.K., Lee, K.H., Choi, J.M. (2021). Performance analysis of cascade multi-functional heat pump in summer season, *Renewable Energy*, vol. 163, p. 1001-1011, **DOI:10.1016/j.renene.2020.09.036**.

[5] Martinović, M., Andrjević, S., Saljnikov, A., Komatina, M., Rudonja, N., Stevanović, Z. (2008). Hydrogeothermal resources & heat pumps – district heating alternative of Serbia. *KGH Conference Proceedings*, p. 314-320.

[6] Ivanovski, I., Goričanec, D., Salamunić, J., Žagar, T. (2018). The comparison between two high-temperature heat-pumps for the production of sanitary water. *Strojniški vestnik - Journal of Mechanical Engineering*, vol. 64, no. 7-8, p. 437-442, **DOI:10.5545/sv-jme.2017.5082**.

[7] Goričanec, D. Rudonja, N., Komatina, M., Andrejević, S., Krope, J., Zlatanović, I. (2008). Cascade type geothermal heat pump – economic analysis and environmental impact, *KGH Conference Proceedings*, p. 140-146.

[8] Bertsch, S.S., Groll, E.A. (2008). Two-stage air-source heat pump for residential heating and cooling applications in northern U.S. climates. *International Journal of Refrigeration*, vol. 31, no. 7, p. 1282-1292, **DOI:10.1016/j.ijrefrig.2008.01.006**.

[9] Jung, H.W., Kang, H., Yoon, W.J., Kim, Y. (2013). Performance comparison between a single-stage and a cascade multi-functional heat pump for both air heating and hot water supply. *International Journal of Refrigeration*, vol. 36, no. 5, p. 1431-1441, **DOI:10.1016/j.ijrefrig.2013.03.003**.

[10] Uusitalo, A., Turunen-Saaresti, T., Honkatukia, J., Tiainen, J., Jaatinen-Värri, A. (2020). Numerical analysis of working fluids for large scale centrifugal compressor driven cascade heat pumps upgrading waste heat. *Applied Energy*, vol. 269, art. ID 115056, **DOI:10.1016/j.apenergy.2020.115056**.

[11] Ma, X., Zhang, Y., Fang, L., Yu, X., Li, X, Sheng, Y., Zhang, Y. (2008). Performance analysis of a cascade high temperature heat pump using R245fa and BY-3 as working fluid. *Applied Thermal Engineering*, vol. 140, p. 466-475, **DOI:10.1016/j.applthermaleng.2018.05.052**.

[12] Xu, L., Li, E., Xu, Y., Mao, N., Shen, X., Wang, X. (2020). An experimental energy performance investigation and economic analysis on a cascade heat pump for high-temperature water in cold region. *Renewable Energy*, vol. 152, p. 674-683, **DOI:10.1016/j.renene.2020.01.104**.

[13] Song, Y., Li, D., Cao, F., Wang, X. (2017). Theoretical investigation on the combined and cascade CO2/R134a heat pump systems for space heating. *Applied Thermal Engineering*, vol. 124, p. 1457-1470, **DOI:10.1016/j.applthermaleng.2017.06.014**.

[14] Song, Y., Li, D., Yang, D., Jin, L., Cao, F., Wang, X. (2017). Performance comparison between the combined R134a/CO2 heat pump and cascade R134a/CO2 heat pump for space heating. *International Journal of Refrigeration*, vol. 74, p. 592-605, **DOI:10.1016/j.ijrefrig.2016.12.001**.

[15] Bhattacharyya, S., Garai, A., Sarkar, J. (2009). Thermodynamic analysis and optimization of a novel N20–CO2 cascade system for refrigeration and heating. *International Journal of Refrigeration*, vol. 32, no. 5, p. 1077-1084, **DOI:10.1016/j.ijrefrig.2008.09.008**.

[16] Park, H., Kim, D.H., Kim, M.S. (2013). Thermodynamic analysis of optimal intermediate temperatures in R134a–R410A cascade refrigeration systems and its experimental verification. *Applied Thermal Engineering*, vol. 54, no. 1, p. 319-327, **DOI:10.1016/j.applthermaleng.2013.01.005**.

[17] Wang, W., Zhou, Q., Tian, G., Hu, B., Li, Y., Cao, (2020). F. The intermediate temperature optimization for cascade refrigeration system and air source heat pump via extreme seeking control. *International Journal of Refrigeration*, vol. 117, p. 150-162, **DOI:10.1016/j.ijrefrig.2020.05.007**.

[18] Balmer, R.T. (2011). *Modern Engineering Thermodynamics*, Elsevier, Amsterdam, **DOI:10.1016/B978-0-12-374996-3.00028-2**.

Vsebina

Strojniški vestnik - Journal of Mechanical Engineering
letnik 66, (2020), številka 11
Ljubljana, november 2020
ISSN 0039-2480

Izhaja mesečno

Razširjeni povzetki (extended abstracts)

Strojniški vestnik - Journal of Mechanical Engineering 66(2020)11, SI 79

Prejeto v recenzijo: 2020-07-01
Prejeto popravljeno: 2020-09-08
Odobreno za objavo: 2020-10-13

Temperatura in prehajanje toplote iz območja rezanja v orodje pri struženju jekla AISI 321

Marian Bartoszuk
Tehniška univerza v Opolah, Poljska

Navdih za ta članek izhaja iz dolgoletnih izkušenj na področju numeričnih simulacij disipacije toplote v območju rezanja. Izračuni po metodi elementarnih bilanc (MEB) so jasno pokazali, da znani koeficienti particije toplote po avtorjih Reznikov, Kato-Fujji ali Shaw ne izpolnjujejo svojega namena. Uporaba teh koeficientov v izračunih povzroči velika odstopanja med simulirano in eksperimentalno določeno povprečno temperaturo na stiku. To odstopanje se z višanjem rezalne hitrosti le povečuje. Analiza teh dejstev je privedla do domneve, da se vrednost koeficienta particije toplote z naraščanjem rezalne hitrosti zmanjšuje in ne povečuje, kot je bilo privzeto pri oblikovanju obstoječih koeficientov. Zato je bila sprejeta odločitev za izvedbo eksperimentalne študije in simulacij za oceno novega koeficienta particije toplote R_B, ki bo bolje opisoval porazdelitev toplote med odrezkom in orodjem.

V članku so prikazani rezultati teh študij, in sicer rezultati eksperimentalnih študij ter rezultati analitičnih in numeričnih modelov toplotnih lastnosti procesa odrezavanja. Opravljeni so bili preskusi suhega ortogonalnega struženja avstenitnega jekla AISI 321 z rezalnim robom z ravno cepilno ploskvijo, izdelanim iz finozrnatega karbida H10F. Uporabljeno je bilo orodno držalo PTNGR 2020-16 in rezalne ploščice TNMA 160408 brez zaščitnih prevlek. V preskusih ni bila uporabljena hladilno-mazalna tekočina.

Z numeričnimi izračuni so bile določene nove vrednosti koeficienta particije toplote in v ta namen je bila uporabljena metoda postopne aproksimacije. V nadaljnjih ponovitvah so bile privzete določene vrednosti koeficienta R_B za doseganje pravilnih rezultatov izračunov. S privzetimi vrednostmi je bila nato razvita formula za novi koeficient porazdelitve toplote R_B. Iz poteka sprememb novega koeficienta porazdelitve toplote je razvidno, da se njegova vrednost zmanjšuje z naraščanjem rezalne hitrosti. To se ujema z dejanskim stanjem, saj se s povečevanjem rezalne hitrosti krajša stik med odrezkom in cepilno ploskvijo. Obenem se povečuje hitrost pretoka odrezkov, s tem pa se skrajša čas vplivanja toplotnega toka na rezalni rob. Oba dejavnika pripomoreta k temu, da se z naraščanjem rezalne hitrosti zmanjšuje odstotni delež toplotnega toka, ki vstopa v orodje po kontaktni dolžini. Formula za novi koeficient particije toplote temelji na medsebojnih odvisnostih termofizikalnih lastnosti rezalnega roba in obdelovanega materiala. Za povečanje točnosti izračunov toplotne prevodnosti sta bili določeni toplotna difuzivnost in specifična toplota obeh materialov.

Raziskava je dokazala, da dosedanja metodologija za računanje povprečne kontaktne temperature s Shawovimi empiričnimi formulami ne deluje. Razlika med povprečnimi kontaktnimi temperaturami iz izračunov in iz eksperimentalnih študij znaša do 23 %. Zato je predlagana nova formula za računanje povprečne vrednosti kontaktne temperature na osnovi zakona toplotne prevodnosti. Izračuni, narejeni z novo formulo, so bistveno točnejši. Največja razlika med rezultati eksperimentov in izračunov po novi formuli je 3,5 %.

Rezultati kažejo, da so lahko razvite formule uporabno orodje za hitro ocenjevanje porazdelitve toplote v območju rezanja. Vsestransko uporabnost formul pa bo mogoče potrditi le z nadaljnjimi raziskavami obdelanih materialov z različnimi termofizikalnimi in obdelovalnimi lastnostmi. Preliminarna analiza rezultatov za jeklo AISI 1045 je pokazala točnost domnev in dobro delovanje izpeljanih formul.

Ključne besede: proces odrezavanja, numerično modeliranje, kontaktna temperatura, porazdelitev toplote

*Naslov avtorja za dopisovanje: Tehniška univerza v Opolah, Prószkowska 76, 45-758 Opole, Poljska, m.bartoszuk@po.edu.pl

Strojniški vestnik - Journal of Mechanical Engineering 66(2020)11, SI 80,

Prejeto v recenzijo: 2020-06-01
Prejeto popravljeno: 2020-07-14
Odobreno za objavo: 2020-07-14

Temelji ocenjevanja vonja v Sloveniji

Martin Dobeic[1] – Vincenc Butala[2] – Matjaž Prek[2] – Jan Leskovšek[3] – Žiga Švegelj[3,*]

[1] Univerza v Ljubljani, Veterinarska fakulteta, Slovenija
[2] Univerza v Ljubljani, Fakulteta za strojništvo, Slovenija
[3] Studio okolje d.o.o., Slovenija

Namen projekta je bil izdelati smernice za ocenjevanje vonja v Sloveniji na podlagi ocene razpoložljivih metod in tehnik ocenjevanja vonjav in predpisov o vonju v izbranih državah. Rezultati, predstavljeni v tem prispevku, temeljijo na stopnjah emisij vonjav iz različnih stacionarnih industrijskih virov, terenskih meritvah koncentracij vonjev in izračunu koncentracij vonjev z uporabo disperzijskega modela.

Onesnaževanje z vonjem je s sociološkega in ekonomskega vidika eden najbolj zapletenih problemov na področju kakovosti zraka. Zato so različni pristopi in merila za vpliv vonja še posebej pomembni za oceno izpostavljenosti vonjava na območjih različne rabe zemljišč. Število metod za oceno vonja je omejeno, pomanjkanje analitičnih tehnik za določanje koncentracije vonja pa naredi ocenjevanje vonja še bolj zapleteno. Da bi lahko ocenili neprijetne vonjave v zunanjem zraku je bistveno analizirati prostorsko in časovno porazdelitev koncentracij vonjav. Analizirani so bili različni viri glede emisij vonja, ofenzivnosti vonja in vrste vira emisij. Med 17 lokacijami emisij je bilo izbrano eno območje ocenjevanja za oceno vpliva vsakega posameznega vira vonja. Ker je reprezentativnost simulacij disperzijskega modela odvisna predvsem od vhodnih podatkov, smo na tem območju z meritvami pridobili 11-mesečne meteorološke podatke, podatke o namembnosti zemljišč in topografske podatke. Za izračun vetrnih polj sta bila povezana diagnostični meteorološki model in mezoskalni prognostični meteorološki model. Urne povprečne koncentracije vonja so bile izračunane z uporabo disperzijskega modela, kratkoročno povišane koncentracije pa s tako imenovano peak-to-mean metodo. Poleg tega so bile s prenosnim olfaktometrom ocenjene koncentracije vonja neposredno na terenu. Na podlagi teh analiz so bila določena merila za ocenjevanje vpliva vonja glede na namembnost zemljišč, hedonični ton vonja, pogostost pojavljanja vonja, namembnost zemljišč ter za obstoječe ali nove objekte.

Na podlagi meritev emisij vonjav iz 17 različnih virov smo ugotovili, kateri viri imajo največji vpliv na okolje. Rezultati so bili analizirani za določitev meril vpliva vonja na okolje. Vpliv vonja je odvisen od dejavnikov, kot so koncentracija oziroma intenzivnost, hedonični ton (ofenzivnost), pogostost izpostavljenosti itd. Med temi dejavniki hedonični ton vonjav še posebej vpliva na obremenjenost okolja z vonjem. Primerjava vplivov izbranih emisijskih virov je bila izvedena na območju z znanimi meteorološkimi razmerami, topografijo in namembnostjo zemljišč.

Medtem ko so disperzijski modeli zelo uporabno orodje za oceno učinka neprijetnega vonja, preverjanje njihovih rezultatov zahteva več raziskav v prihodnosti. Zlasti je treba izvesti oceno vpliva vonja z različnimi metodami terenskih pregledov in študijami odziva izpostavljenih prebivalcev na obremenitve z vonjem.

Izvedba in oblikovanje ustreznega pristopa sta bila temelj te raziskave in sta podlaga za nadaljnje in podrobnejše raziskave, pri čemer sta dodana vrednot in znanstveni prispevek tega dela prikaz kako je mogoče v specifičnem okolju na podlagi rezultatov meritev določiti smernice za oblikovanje modelskih postopkov vrednotenja obremenjevanja okolja z vonji.

Ključne besede: viri emisij vonja, koncentracija vonja, obremenjevanje okolja z vonjem, ocenjevanje obremenjenosti zunanjega zraka z vonjem, ofenzivnost vonja, 95. in 99. percentil zaznavanja vonja, matematični model disperzije

*Naslov avtorja za dopisovanje: Studio okolje d.o.o., Slovenija, ziga.svegelj@studiookolje.si

Strojniški vestnik - Journal of Mechanical Engineering 66(2020)11, SI 81

Prejeto v recenzijo: 2020-07-20
Prejeto popravljeno: 2020-10-02
Odobreno za objavo: 2020-10-13

Obremenitvena analiza cikloidnega reduktorja RV na osnovi načela minimalne energije

Tianxing Li[1,2,*] – Hang Xu[3] – Meng Tian[2]

[1] Znanstveno-tehniška univerza v Henanu, Šola za mehatroniko, Kitajska
[2] Sodelovalno inovacijsko središče province Henan za napredno proizvodnjo strojne opreme, Kitajska
[3] Tehniška univerza v Zhongyuanu, Šola za mehatroniko, Kitajska

Ena glavnih komponent robotov je reduktor RV (rotacijski vektor), ki predstavlja približno 38 % celotnih stroškov. Učinek izenačevanja napak, ki ga zagotavlja sočasno ubiranje več zob, omogoča izboljšanje natančnosti prenosa tega reduktorja za visoko togost in nosilnost. Teoretični reduktorji RV s cikloidnimi čepi pa zaradi kompleksne porazdelitve obremenitev in kontaktnih razmer ter zaradi pomanjkanja učinkovitih analitičnih metod izkazujejo razmeroma slabo zmogljivost pod obremenitvijo v praktičnih aplikacijah. Znani nerazrešeni problemi prenosnikov RV vključujejo nizko natančnost prenosa, nezadostno nosilnost in le kratkotrajno ohranitev natančnosti.

V članku je podana učinkovita analitična metoda na osnovi načela minimalne energije, ki omogoča določanje realnih obremenitvenih lastnosti prenosnikov RV. V kontaktno analizo prenosnika s cikloidnimi čepi pod obremenitvijo so bili integrirani teorija Hertzovega kontakta, načelo minimalne energije in metoda končnih elementov, določena je bila nelinearna povezava med obremenitvijo pri ubiranju in deformacijo in ugotovljena je bila dejanska obremenitvena karakteristika. Možno število zob v ubiranju je bilo hitro ocenjeno na podlagi porazdelitve minimalnega razstopa in maksimalne deformacije cikloidnega čepa. V obremenitveni analizi je bilo z inovativno uvedbo načela minimalne energije natančno določeno dejansko število zob, ki ubirajo sočasno. To število neposredno vpliva na natančnost obremenitvene analize in na dejansko kakovost ubiranja. Primerjava in validacija teoretičnega modela, simulacija po metodi končnih elementov in eksperimenti so pokazali praktično enako razliko v kontaktnem tlaku, številu zob v ubiranju, obliki kontakta in napaki prenosa. S tem je bila dokazana pravilnost in uporabnost teoretične analitične metode ter uspešnost uporabe načela minimalne energije. Študija je obrodila tudi druge uporabne rezultate. Radij ukrivljenosti cikloidnega zobnika ima očitnejši vpliv na kontaktni tlak in majhen vpliv na deformacijo v obremenjenem stanju. Pravilo spreminjanja oblike obremenitvenega kontakta je praktično enako kot pri sili ubiranja in kontaktnem tlaku: večja kot sta kontaktna sila in kontaktni tlak, večja je kontaktna površina. Kontaktna deformacija, torzijska deformacija in razstop so pomembni povzročitelji napak pri prenosu pod obremenitvijo, kar je tudi glavna razlika v analizi lastnosti ubiranja cikloidnega prenosnika v neobremenjenem in obremenjenem stanju.

Študija je tako razrešila problem neujemanja dejanske učinkovitosti ubiranja obremenjenega reduktorja RV z rezultati teoretičnih analiz. Zato predstavlja tudi pomembno izhodišče za izboljšave in spremljanje kinematične točnosti reduktorjev RV za robote. Obravnava predlagane metode pa še ni končana, saj bodo potrebne podrobnejše analize lastnosti prenosa reduktorja RV v teoretičnem modelu, vpliva obremenitvenega navora na napake v prenosu, in analiza števila zob v ubiranju. Potrebne bodo tudi eksperimentalne raziskave v realnih delovnih pogojih.

Ključne besede: cikloidni prenosnik, obremenitvena karakteristika, princip minimalne energije, reduktor RV (rotacijski vektor), napake v prenosu, oblika kontakta, število zob v ubiranju

*Naslov avtorja za dopisovanje: Znanstveno-tehniška univerza v Henanu, Šola za mehatroniko, Luoyang, Kitajska, litianxing@haust.edu.cn

Strojniški vestnik - Journal of Mechanical Engineering 66(2020)11, SI 82

Prejeto v recenzijo: 2020-06-07
Prejeto popravljeno: 2020-08-24
Odobreno za objavo: 2020-10-06

Raziskava delovanja nove zunanje naprave za mašenje netesnosti na tlačnih posodah

Hongwei Yan – Xiong Yang – Xiangrong Hou – Lu Wang – Pengcheng Li
Šola za strojništvo, Kitajska severna univerza, Kitajska

Pri izvajanju intervencij za odpravo netesnosti se pojavljajo mnoge nepredvidljive tehnične težave, ki izvirajo iz različnih fizikalnih in kemijskih lastnosti materialov in različnih vrst uhajanja. V članku je zato podan predlog nove zunanje priprave za mašenje netesnosti kot so luknje in razpoke na velikih cevovodih in skladiščnih rezervoarjih, ki lahko učinkovito obvlada nevarne vire uhajanja in zmanjša posledično škodo.

Na podlagi raziskave trga so bile določene konstrukcijske zahteve za novo zunanjo mašilno pripravo in postavljen je bil tridimenzionalni model. Simuliran in analiziran je bil postopek namestitve in mašenja s konvencionalno zgornjo tlačno mašilno pripravo in z novo zunanjo mašilno pripravo, nato pa so bile primerjalno določene prednosti nove rešitve.

Postavljeni so bili modeli po metodi končnih elementov za konvencionalno zgornjo mašilno pripravo in novo zunanjo mašilno pripravo, nato pa je bil simuliran in analiziran postopek namestitve in zatesnitve z obema pripravama. Primerjava je pokazala, da nova zunanja mašilna priprava omogoča hitro namestitev, majhen upor pri namestitvi in dobro prilagajanje površini netesnosti.

Analizirane so prednosti in pomanjkljivosti obstoječe tehnologije za mašenje in predlagana je nova vrsta zunanje priprave za mašenje netesnosti na tlačnih posodah. Simulacijska analiza razpok in porazdelitve tlaka je pokazala, da se z vgradnjo nove zunanje mašilne priprave oblikujeta kontaktno območje z enakomernim tlakom in območje zatesnitve, medtem ko pojava koncentracije napetosti ni bilo mogoče opaziti. Stabilnost in zanesljivost zasilne zatesnitve se izboljšata z zmanjšanjem debeline tesnila.

Omejitve raziskave, implikacije:

Pri novi zunanji mašilni pripravi je uporabljen način namestitve s preusmeritvijo, kjer se priprava najprej namesti in nato blokira z ventilom (na preusmeritveni cevi) za zmanjšanje upora pri nameščanju. Namestitev je tako natančnejša in zanesljivejša. V nadaljnjih raziskavah bo treba določiti še optimalno velikost preusmeritvene odprtine za učinkovito zmanjšanje mašilnega tlaka brez kompromisov glede učinka zatesnitve.

Nova zunanja mašilna priprava lahko zatesni manjše luknje in razpoke na posodah. V prihodnjih raziskavah bo treba preučiti še neprekinjeno zatesnitev daljših razpok.

Nova vrsta zunanje mašilne priprave mora učinkovito zatesniti zunanjo površino tlačne posode. Za to bo zelo pomembna tudi preučitev prilagodljivosti materiala zunanje kontaktne kapsule kompleksni površini.

V članku je podan predlog nove vrste zunanje priprave za zatesnitev netesnosti na tlačnih posodah, tj. lukenj in razpok na velikih cevovodih in skladiščnih rezervoarjih. Priprava zagotavlja hitrost in majhen upor pri namestitvi ter se bolje prilagaja površini netesnosti. Za aktiviranje naprave je vgrajen ročični mehanizem, fluidna snov v prostoru kolobarjaste oblike pa omogoča prilagajanje kompleksnim ukrivljenim površinam, sprotni nadzor in samodejno prilagajanje zatesnitve. V predlogu nove rešitev je predstavljena nova zamisel za optimizacijo konstrukcije priprav za mašenje cevovodov. Predlog bo koristen za vrednotenje zanesljivosti priprav tega tipa.

Ključne besede: uhajanje, preusmeritveni kanal, ANSYS, zatesnitev s fluidno kapsulo, prilagodljiv stik, koncentracija napetosti, tlačna posoda

*Naslov avtorja za dopisovanje: Šola za strojništvo, Kitajska severna univerza, Taiyuan, Kitajska, aweigeyan@nuc.edu.cn

Strojniški vestnik - Journal of Mechanical Engineering 66(2020)11, SI 83

Prejeto v recenzijo: 2020-06-27
Prejeto popravljeno: 2020-10-01
Odobreno za objavo: 2020-10-27

Termodinamična analiza kaskadne toplotne črpalke v visokotemperaturnem ogrevalnem sistemu

Nedžad Rudonja* – Milan Gojak – Ivan Zlatanović – Ružica Todorović
Univerza v Beogradu, Fakulteta za strojništvo, Srbija

V članku je predstavljena termodinamična analiza sistema kaskadne toplotne črpalke, projektiranega za uporabo v visokotemperaturnih ogrevalnih sistemih. V literaturi je le malo člankov o kaskadnih toplotnih črpalkah zrak-voda, ki delujejo pri nizkih temperaturah in zagotavljajo visokotemperaturno ogrevanje. V pričujočem prispevku je zato preučen vpliv različnih kombinacij delovnih medijev na delovanje take toplotne črpalke. Nov termodinamični model je bil zgrajen na osnovi lastnosti delovnih medijev iz baze *CoolProp*. Kaskadna toplotna črpalka je bila projektirana za delo z zunanjim zrakom temperature t_{amb} = –20 °C kot virom toplote in visokotemperaturnim ogrevalnim sistemom do 70 °C. Analizirane so bile štiri kombinacije delovnih medijev za doseganje najvišjih vrednosti grelnega števila (COP) v danem temperaturnem območju. Temperaturno območje je bilo izbrano za ogrevanje objektov z visokotemperaturnimi ogrevalnimi sistemi in uporabo zunanjega zraka kot vira toplote. Za vsako kombinacijo delovnega medija je bila izračunana vrednost grelnega števila s spreminjanjem srednje temperature kaskadnega prenosnika toplote. Temperatura kondenzacije v visokotemperaturnem krogu je bila 75 °C, izparilna temperatura v nizkotemperaturnem krogu pa –25 °C. Napovedana moč kaskadne toplotne črpalke je bila 100 kW. Za najboljšo kombinacijo delovnih medijev so bili analizirani podhlajevanje, pregrevanje, tlačne izgube v sesalnem vodu kompresorja in eksergijska učinkovitost toplotne črpalke kot funkcije srednje temperature kaskadnega prenosnika toplote. Tako kombinacijo pri danih delovnih pogojih predstavljata R245fa v nizkotemperaturnem krogu in R717 v visokotemperaturnem krogu toplotne črpalke. Najvišja vrednost grelnega števila je bila 2,77 in sledi sklep o upravičenosti uporabe kaskadnih toplotnih črpalk v visokotemperaturnih ogrevalnih sistemih. Pri vsaki kombinaciji delovnih medijev obstaja optimalna vrednost srednje temperature kaskadnega prenosnika toplote, pri kateri je vrednost grelnega števila maksimalna. Tlačne izgube v sesalnem vodu kompresorja v višini 2000 Pa prispevajo k zmanjšanju grelnega števila za skoraj 2,5 %. S podhladitvijo delovnega medija na izhodu kondenzatorja za 5 K se vrednost grelnega števila poveča za približno 2,5 %. Pregrevanje delovnega medija na vstopu kompresorja je pomembno za zaščito kompresorja, vendar ima tudi manjši negativen vpliv na vrednost grelnega števila. Zmanjšanje adiabatnega izkoristka kompresorjev znatno zmanjša vrednost grelnega števila, odvisnost pa je linearna.

Rezultati so uporabni za projektante in inženirje, ki projektirajo kaskadne toplotne črpalke za izkoriščanje toplote zraka v danem temperaturnem območju, saj podajajo predlog najboljše kombinacije delovnih medijev za največjo učinkovitost toplotnih črpalk. Znanstvenikom pa daje tudi boljši vpogled v vpliv analiziranih pojavov na termodinamično zmogljivost sistemov kaskadnih toplotnih črpalk. Delo se bo nadaljevalo z verifikacijo rezultatov v eksperimentalni študiji na realni kaskadni toplotni črpalki.

Ključne besede: kaskadne toplotne črpalke, delovni mediji, grelno število, eksergijski izkoristek

*Naslov avtorja za dopisovanje: Univerza v Beogradu, Fakulteta za strojništvo, Srbija, nrudonja@mas.bg.ac.rs

Guide for Authors

All manuscripts must be in English. Pages should be numbered sequentially. The manuscript should be composed in accordance with the Article Template given above. The maximum length of contributions is 12 pages (approx. 5000 words). Longer contributions will only be accepted if authors provide justification in a cover letter. For full instructions see the Information for Authors section on the journal's website: http://en.sv-jme.eu .

SUBMISSION:

Submission to SV-JME is made with the implicit understanding that neither the manuscript nor the essence of its content has been published previously either in whole or in part and that it is not being considered for publication elsewhere. All the listed authors should have agreed on the content and the corresponding (submitting) author is responsible for having ensured that this agreement has been reached. The acceptance of an article is based entirely on its scientific merit, as judged by peer review. Scientific articles comprising simulations only will not be accepted for publication; simulations must be accompanied by experimental results carried out to confirm or deny the accuracy of the simulation. Every manuscript submitted to the SV-JME undergoes a peer-review process.

The authors are kindly invited to submit the paper through our web site: http://ojs.sv-jme.eu. The Author is able to track the submission through the editorial process - as well as participate in the copyediting and proofreading of submissions accepted for publication - by logging in, and using the username and password provided.

SUBMISSION CONTENT:

The typical submission material consists of:

- A **manuscript** (A PDF file, with title, all authors with affiliations, abstract, keywords, highlights, inserted figures and tables and references),
- Supplementary files:
  - a **manuscript** in a WORD file format
  - a **cover letter** (please see instructions for composing the cover letter)
  - a ZIP file containing **figures** in high resolution in one of the graphical formats (please see instructions for preparing the figure files)
  - possible **appendicies** (optional), cover materials, video materials, etc.

Incomplete or improperly prepared submissions will be rejected with explanatory comments provided. In this case we will kindly ask the authors to carefully read the Information for Authors and to resubmit their manuscripts taking into consideration our comments.

COVER LETTER INSTRUCTIONS:

Please add a **cover letter** stating the following information about the submitted paper:

1. Paper **title**, list of **authors** and their **affiliations**. **One** corresponding author should be provided.
2. **Type of paper**: original scientific paper (1.01), review scientific paper (1.02) or short scientific paper (1.03).
3. A **declaration** that neither the manuscript nor the essence of its content has been published in whole or in part previously and that it is not being considered for publication elsewhere.
4. State the **value of the paper** or its practical, theoretical and scientific implications. What is new in the paper with respect to the state-of-the-art in the published papers? Do not repeat the content of your abstract for this purpose.
5. We kindly ask you to suggest at least two **reviewers** for your paper and give us their names, their full affiliation and contact information, and their scientific research interest. The suggested reviewers should have at least two relevant references (with an impact factor) to the scientific field concerned; they should not be from the same country as the authors and should have no close connection with the authors.

FORMAT OF THE MANUSCRIPT:

The manuscript should be composed in accordance with the Article Template. The manuscript should be written in the following format:

- A **Title** that adequately describes the content of the manuscript.
- A list of **Authors** and their **affiliations**.
- An **Abstract** that should not exceed 250 words. The Abstract should state the principal objectives and the scope of the investigation, as well as the methodology employed. It should summarize the results and state the principal conclusions.
- 4 to 6 significant **key words** should follow the abstract to aid indexing.
- 4 to 6 **highlights;** a short collection of bullet points that convey the core findings and provide readers with a quick textual overview of the article. These four to six bullet points should describe the essence of the research (e.g. results or conclusions) and highlight what is distinctive about it.
- An **Introduction** that should provide a review of recent literature and sufficient background information to allow the results of the article to be understood and evaluated.
- A **Methods** section detailing the theoretical or experimental methods used.
- An **Experimental section** that should provide details of the experimental set-up and the methods used to obtain the results.
- A **Results** section that should clearly and concisely present the data, using figures and tables where appropriate.
- A **Discussion** section that should describe the relationships and generalizations shown by the results and discuss the significance of the results, making comparisons with previously published work. (It may be appropriate to combine the Results and Discussion sections into a single section to improve clarity.)
- A **Conclusions** section that should present one or more conclusions drawn from the results and subsequent discussion and should not duplicate the Abstract.
- **Acknowledgement** (optional) of collaboration or preparation assistance may be included. Please note the source of funding for the research.
- **Nomenclature** (optional). Papers with many symbols should have a nomenclature that defines all symbols with units, inserted above the references. If one is used, it must contain all the symbols used in the manuscript and the definitions should not be repeated in the text. In all cases, identify the symbols used if they are not widely recognized in the profession. Define acronyms in the text, not in the nomenclature.
- **References** must be cited consecutively in the text using square brackets [1] and collected together in a reference list at the end of the manuscript.
- **Appendix(-icies)** if any.

SPECIAL NOTES

Units: The SI system of units for nomenclature, symbols and abbreviations should be followed closely. Symbols for physical quantities in the text should be written in italics (e.g. *v*, *T*, *n*, etc.). Symbols for units that consist of letters should be in plain text (e.g. ms^{-1}, K, min, mm, etc.). Please also see: http://physics.nist.gov/cuu/pdf/sp811.pdf .

Abbreviations should be spelt out in full on first appearance followed by the abbreviation in parentheses, e.g. variable time geometry (VTG). The meaning of symbols and units belonging to symbols should be explained in each case or cited in a **nomenclature** section at the end of the manuscript before the References.

Figures (figures, graphs, illustrations digital images, photographs) must be cited in consecutive numerical order in the text and referred to in both the text and the captions as Fig. 1, Fig. 2, etc. Figures should be prepared without borders and on white grounding and should be sent separately in their original formats. If a figure is composed of several parts, please mark each part with a), b), c), etc. and provide an explanation for each part in Figure caption. The caption should be self-explanatory. Letters and numbers should be readable (Arial or Times New Roman, min 6 pt with equal sizes and fonts in all figures). Graphics (submitted as supplementary files) may be exported in resolution good enough for printing (min. 300 dpi) in any common format, e.g. TIFF, BMP or JPG, PDF and should be named Fig1.jpg, Fig2.tif, etc. However, graphs and line drawings should be prepared as vector images, e.g. CDR, AI. Multi-curve graphs should have individual curves marked with a symbol or otherwise provide distinguishing differences using, for example, different thicknesses or dashing.

Tables should carry separate titles and must be numbered in consecutive numerical order in the text and referred to in both the text and the captions as Table 1, Table 2, etc. In addition to the physical quantities, such as *t* (in italics), the units [s] (normal text) should be added in square brackets. Tables should not duplicate data found elsewhere in the manuscript. Tables should be prepared using a table editor and not inserted as a graphic.

REFERENCES:

A reference list must be included using the following information as a guide. Only cited text references are to be included. Each reference is to be referred to in the text by a number enclosed in a square bracket (i.e. [3] or [2] to [4] for more references; do not combine more than 3 references, explain each). No reference to the author is necessary.

References must be numbered and ordered according to where they are first mentioned in the paper, not alphabetically. All references must be complete and accurate. Please add DOI code when available. Examples follow.

Journal Papers:

Surname 1, Initials, Surname 2, Initials (year). Title. Journal, volume, number, pages, DOI code.

[1] Hackenschmidt, R., Alber-Laukant, B., Rieg, F. (2010). Simulating nonlinear materials under centrifugal forces by using intelligent cross-linked simulations. *Strojniški vestnik - Journal of Mechanical Engineering,* vol. 57, no. 7-8, p. 531-538, DOI:10.5545/sv-jme.2011.013.

Journal titles should not be abbreviated. Note that journal title is set in italics.

Books:

Surname 1, Initials, Surname 2, Initials (year). Title. Publisher, place of publication.

[2] Groover, M.P. (2007). *Fundamentals of Modern Manufacturing*. John Wiley & Sons, Hoboken.

Note that the title of the book is italicized.

Chapters in Books:

Surname 1, Initials, Surname 2, Initials (year). Chapter title. Editor(s) of book, book title. Publisher, place of publication, pages.

[3] Carbone, G., Ceccarelli, M. (2005). Legged robotic systems. Kordić, V., Lazinica, A., Merdan, M. (Eds.), Cutting Edge Robotics. Pro literatur Verlag, Mammendorf, p. 553-576.

Proceedings Papers:

Surname 1, Initials, Surname 2, Initials (year). Paper title. Proceedings title, pages.

[4] Štefanić, N., Martinčević-Mikić, S., Tošanović, N. (2009). Applied lean system in process industry. *MOTSP Conference Proceedings*, p. 422-427.

Standards:

Standard-Code (year). Title. Organisation. Place.

[5] ISO/DIS 16000-6.2:2002. *Indoor Air – Part 6: Determination of Volatile Organic Compounds in Indoor and Chamber Air by Active Sampling on TENAX TA Sorbent, Thermal Desorption and Gas Chromatography using MSD/FID.* International Organization for Standardization. Geneva.

WWW pages:

Surname, Initials or Company name. Title, from http://address, date of access.

[6] Rockwell Automation. Arena, from *http://www.arenasimulation.com,* accessed on 2009-09-07.

EXTENDED ABSTRACT:

When the paper is accepted for publishing, the authors will be requested to send an **extended abstract** (approx. one A4 page or 3500 to 4000 characters or approx. 600 words). The instruction for composing the extended abstract are published on-line: http://www.sv-jme.eu/information-for-authors/ .

COPYRIGHT:

Authors submitting a manuscript do so on the understanding that the work has not been published before, is not being considered for publication elsewhere and has been read and approved by all authors. The submission of the manuscript by the authors means that the authors automatically agree to transfer copyright to SV-JME when the manuscript is accepted for publication. All accepted manuscripts must be accompanied by a Copyright Transfer Agreement, which should be sent to the editor. The work should be original work by the authors and not be published elsewhere in any language without the written consent of the publisher. The proof will be sent to the author showing the final layout of the article. Proof correction must be minimal and executed quickly. Thus it is essential that manuscripts are accurate when submitted. Authors can track the status of their accepted articles on http://en.sv-jme.eu/.

PUBLICATION FEE:

Authors will be asked to pay a publication fee for each article prior to the article appearing in the journal. However, this fee only needs to be paid after the article has been accepted for publishing. The fee is 380 EUR (for articles with maximum of 6 pages), 470 EUR (for articles with maximum of 10 pages), plus 50 EUR for each additional page. The additional cost for a color page is 90.00 EUR (only for a journal hard copy; optional upon author's request). These fees do not include tax.

Strojniški vestnik -Journal of Mechanical Engineering
Aškerčeva 6, 1000 Ljubljana, Slovenia, e-mail: info@sv-jme.eu

9 770039 248001
ISSN 0039-2480

http://www.sv-jme.eu

Contents

Papers